

Measurement of the Inclusive $e^\pm p$ Scattering Cross Section at High Inelasticity y and of the Structure Function F_L

H1 Collaboration

Abstract

A measurement is presented of the inclusive neutral current $e^\pm p$ scattering cross section using data collected by the H1 experiment at HERA during the years 2003 to 2007 with proton beam energies E_p of 920, 575, and 460 GeV. The kinematic range of the measurement covers low absolute four-momentum transfers squared, $1.5 \text{ GeV}^2 < Q^2 < 120 \text{ GeV}^2$, small values of Bjorken x , $2.9 \cdot 10^{-5} < x < 0.01$, and extends to high inelasticity up to $y = 0.85$. The structure function F_L is measured by combining the new results with previously published H1 data at $E_p = 920 \text{ GeV}$ and $E_p = 820 \text{ GeV}$. The new measurements are used to test several phenomenological and QCD models applicable in this low Q^2 and low x kinematic domain.

Submitted to EPJC

F.D. Aaron^{5,49}, C. Alexa⁵, V. Andreev²⁵, S. Backovic³⁰, A. Baghdasaryan³⁸, S. Baghdasaryan³⁸, E. Barrelet²⁹, W. Bartel¹¹, O. Behrend^{8,54}, P. Belov¹¹, K. Begzsuren³⁵, A. Belousov²⁵, J.C. Bizot²⁷, V. Boudry²⁸, I. Bozovic-Jelisavcic², J. Bracinik³, G. Brandt¹¹, M. Brinkmann¹¹, V. Brisson²⁷, D. Britzger¹¹, D. Bruncko¹⁶, A. Bunyatyan^{13,38}, G. Buschhorn^{26,†}, A. Bylinkin²⁴, L. Bystritskaya²⁴, A.J. Campbell¹¹, K.B. Cantun Avila²², F. Ceccopieri⁴, K. Cerny³², V. Cerny^{16,47}, V. Chekelian²⁶, A. Cholewa¹¹, J.G. Contreras²², J.A. Coughlan⁶, J. Cvach³¹, J.B. Dainton¹⁸, K. Daum^{37,43}, B. Delcourt²⁷, J. Delvax⁴, E.A. De Wolf⁴, C. Diaconu²¹, M. Dobre^{12,51,52}, V. Dodonov¹³, A. Dossanov²⁶, A. Dubak^{30,46}, G. Eckerlin¹¹, S. Egli³⁶, A. Eliseev²⁵, E. Elsen¹¹, L. Favart⁴, A. Fedotov²⁴, R. Felst¹¹, J. Feltesse^{10,48}, J. Ferencei¹⁶, D.-J. Fischer¹¹, M. Fleischer¹¹, A. Fomenko²⁵, E. Gabathuler¹⁸, J. Gayler¹¹, S. Ghazaryan¹¹, A. Glazov¹¹, L. Goerlich⁷, N. Gogitidze²⁵, M. Gouzevitch^{11,45}, C. Grab⁴⁰, A. Grebenyuk¹¹, T. Greenshaw¹⁸, B.R. Grell¹¹, G. Grindhammer²⁶, S. Habib¹¹, D. Haidt¹¹, C. Helebrant¹¹, R.C.W. Henderson¹⁷, E. Hennekemper¹⁵, H. Henschel³⁹, M. Herbst¹⁵, G. Herrera²³, M. Hildebrandt³⁶, K.H. Hiller³⁹, D. Hoffmann²¹, R. Horisberger³⁶, T. Hreus^{4,44}, F. Huber¹⁴, M. Jacquet²⁷, X. Janssen⁴, L. Jönsson²⁰, A.W. Jung¹⁵, H. Jung^{11,4}, M. Kapichine⁹, J. Katzy¹¹, I.R. Kenyon³, C. Kiesling²⁶, M. Klein¹⁸, C. Kleinwort¹¹, T. Kluge¹⁸, A. Knutsson¹¹, R. Kogler²⁶, P. Kostka³⁹, M. Kraemer¹¹, J. Kretzschmar¹⁸, K. Krüger¹⁵, K. Kutak¹¹, M.P.J. Landon¹⁹, W. Lange³⁹, G. Laštovička-Medin³⁰, P. Laycock¹⁸, A. Lebedev²⁵, V. Lendermann¹⁵, S. Levonian¹¹, K. Lipka^{11,51}, B. List¹², J. List¹¹, N. Loktionova²⁵, R. Lopez-Fernandez²³, V. Lubimov²⁴, A. Makankine⁹, E. Malinovski²⁵, P. Marage⁴, H.-U. Martyn¹, S.J. Maxfield¹⁸, A. Mehta¹⁸, A.B. Meyer¹¹, H. Meyer³⁷, J. Meyer¹¹, S. Mikocki⁷, I. Milcewicz-Mika⁷, F. Moreau²⁸, A. Morozov⁹, J.V. Morris⁶, M.U. Mozer⁴, M. Mudrinic², K. Müller⁴¹, Th. Naumann³⁹, P.R. Newman³, C. Niebuhr¹¹, A. Nikiforov^{11,53}, D. Nikitin⁹, G. Nowak⁷, K. Nowak¹¹, J.E. Olsson¹¹, S. Osman²⁰, D. Ozerov²⁴, P. Pahl¹¹, V. Palichik⁹, I. Panagoulas^{1,11,42}, M. Pandurovic², Th. Papadopoulou^{1,11,42}, C. Pascaud²⁷, G.D. Patel¹⁸, E. Perez^{10,45}, A. Petrukhin¹¹, I. Picuric³⁰, S. Piec¹¹, H. Pirumov¹⁴, D. Pitzl¹¹, R. Plačakyte¹², B. Pokorny³², R. Polifka³², B. Povh¹³, V. Radescu¹⁴, N. Raicevic³⁰, T. Ravdandorj³⁵, P. Reimer³¹, E. Rizvi¹⁹, P. Robmann⁴¹, R. Roosen⁴, A. Rostovtsev²⁴, M. Rotaru⁵, J.E. Ruiz Tabasco²², S. Rusakov²⁵, D. Šálek³², D.P.C. Sankey⁶, M. Sauter¹⁴, E. Sauvan²¹, S. Schmitt¹¹, L. Schoeffel¹⁰, A. Schöning¹⁴, H.-C. Schultz-Coulon¹⁵, F. Sefkow¹¹, L.N. Shtarkov²⁵, S. Shushkevich²⁶, T. Sloan¹⁷, I. Smiljanic², Y. Soloviev²⁵, P. Sopicki⁷, D. South¹¹, V. Spaskov⁹, A. Specka²⁸, Z. Staykova¹¹, M. Steder¹¹, B. Stella³³, G. Stoicea⁵, U. Straumann⁴¹, T. Sykora^{4,32}, P.D. Thompson³, T. Toll¹¹, T.H. Tran²⁷, D. Traynor¹⁹, P. Truöl⁴¹, I. Tsakov³⁴, B. Tseepeldorj^{35,50}, I. Tsurin¹⁸, J. Turnau⁷, K. Urban¹⁵, A. Valkárová³², C. Vallée²¹, P. Van Mechelen⁴, A. Vargas¹¹, Y. Vazdik²⁵, M. von den Driesch¹¹, D. Wegener⁸, E. Wunsch¹¹, J. Žáček³², J. Zálešák³¹, Z. Zhang²⁷, A. Zhokin²⁴, H. Zohrabyan³⁸, and F. Zomer²⁷

¹ *I. Physikalisches Institut der RWTH, Aachen, Germany*

² *Vinca Institute of Nuclear Sciences, University of Belgrade, 1100 Belgrade, Serbia*

³ *School of Physics and Astronomy, University of Birmingham, Birmingham, UK^b*

⁴ *Inter-University Institute for High Energies ULB-VUB, Brussels and Universiteit Antwerpen, Antwerpen, Belgium^c*

⁵ *National Institute for Physics and Nuclear Engineering (NIPNE), Bucharest, Romania^m*

⁶ *Rutherford Appleton Laboratory, Chilton, Didcot, UK^b*

⁷ *Institute for Nuclear Physics, Cracow, Poland^d*

⁸ *Institut für Physik, TU Dortmund, Dortmund, Germany^a*

- ⁹ *Joint Institute for Nuclear Research, Dubna, Russia*
- ¹⁰ *CEA, DSM/Trfu, CE-Saclay, Gif-sur-Yvette, France*
- ¹¹ *DESY, Hamburg, Germany*
- ¹² *Institut für Experimentalphysik, Universität Hamburg, Hamburg, Germany^a*
- ¹³ *Max-Planck-Institut für Kernphysik, Heidelberg, Germany*
- ¹⁴ *Physikalisches Institut, Universität Heidelberg, Heidelberg, Germany^a*
- ¹⁵ *Kirchhoff-Institut für Physik, Universität Heidelberg, Heidelberg, Germany^a*
- ¹⁶ *Institute of Experimental Physics, Slovak Academy of Sciences, Košice, Slovak Republic^f*
- ¹⁷ *Department of Physics, University of Lancaster, Lancaster, UK^b*
- ¹⁸ *Department of Physics, University of Liverpool, Liverpool, UK^b*
- ¹⁹ *Queen Mary and Westfield College, London, UK^b*
- ²⁰ *Physics Department, University of Lund, Lund, Sweden^g*
- ²¹ *CPPM, Aix-Marseille Université, CNRS/IN2P3, Marseille, France*
- ²² *Departamento de Física Aplicada, CINVESTAV, Mérida, Yucatán, México^j*
- ²³ *Departamento de Física, CINVESTAV IPN, México City, México^j*
- ²⁴ *Institute for Theoretical and Experimental Physics, Moscow, Russia^k*
- ²⁵ *Lebedev Physical Institute, Moscow, Russia^e*
- ²⁶ *Max-Planck-Institut für Physik, München, Germany*
- ²⁷ *LAL, Université Paris-Sud, CNRS/IN2P3, Orsay, France*
- ²⁸ *LLR, Ecole Polytechnique, CNRS/IN2P3, Palaiseau, France*
- ²⁹ *LPNHE, Université Pierre et Marie Curie Paris 6, Université Denis Diderot Paris 7, CNRS/IN2P3, Paris, France*
- ³⁰ *Faculty of Science, University of Montenegro, Podgorica, Montenegro^e*
- ³¹ *Institute of Physics, Academy of Sciences of the Czech Republic, Praha, Czech Republic^h*
- ³² *Faculty of Mathematics and Physics, Charles University, Praha, Czech Republic^h*
- ³³ *Dipartimento di Fisica Università di Roma Tre and INFN Roma 3, Roma, Italy*
- ³⁴ *Institute for Nuclear Research and Nuclear Energy, Sofia, Bulgaria^e*
- ³⁵ *Institute of Physics and Technology of the Mongolian Academy of Sciences, Ulaanbaatar, Mongolia*
- ³⁶ *Paul Scherrer Institut, Villigen, Switzerland*
- ³⁷ *Fachbereich C, Universität Wuppertal, Wuppertal, Germany*
- ³⁸ *Yerevan Physics Institute, Yerevan, Armenia*
- ³⁹ *DESY, Zeuthen, Germany*
- ⁴⁰ *Institut für Teilchenphysik, ETH, Zürich, Switzerlandⁱ*
- ⁴¹ *Physik-Institut der Universität Zürich, Zürich, Switzerlandⁱ*
- ⁴² *Also at Physics Department, National Technical University, Zografou Campus, GR-15773 Athens, Greece*
- ⁴³ *Also at Rechenzentrum, Universität Wuppertal, Wuppertal, Germany*
- ⁴⁴ *Also at University of P.J. Šafárik, Košice, Slovak Republic*
- ⁴⁵ *Also at CERN, Geneva, Switzerland*
- ⁴⁶ *Also at Max-Planck-Institut für Physik, München, Germany*
- ⁴⁷ *Also at Comenius University, Bratislava, Slovak Republic*
- ⁴⁸ *Also at DESY and University Hamburg, Helmholtz Humboldt Research Award*
- ⁴⁹ *Also at Faculty of Physics, University of Bucharest, Bucharest, Romania*
- ⁵⁰ *Also at Ulaanbaatar University, Ulaanbaatar, Mongolia*
- ⁵¹ *Supported by the Initiative and Networking Fund of the Helmholtz Association (HGF) under*

the contract VH-NG-401.

⁵² *Absent on leave from NIPNE-HH, Bucharest, Romania*

⁵³ *Now at Humboldt Universität Berlin, Berlin, Germany*

⁵⁴ *Now at Siemens, Nürnberg, Germany*

† *Deceased*

^a *Supported by the Bundesministerium für Bildung und Forschung, FRG, under contract numbers 05H09GUF, 05H09VHC, 05H09VHF, 05H16PEA*

^b *Supported by the UK Science and Technology Facilities Council, and formerly by the UK Particle Physics and Astronomy Research Council*

^c *Supported by FNRS-FWO-Vlaanderen, IISN-IKW and IWT and by Interuniversity Attraction Poles Programme, Belgian Science Policy*

^d *Partially Supported by Polish Ministry of Science and Higher Education, grant DPN/N168/DESY/2009*

^e *Supported by the Deutsche Forschungsgemeinschaft*

^f *Supported by VEGA SR grant no. 2/7062/27*

^g *Supported by the Swedish Natural Science Research Council*

^h *Supported by the Ministry of Education of the Czech Republic under the projects LC527, INGO-LA09042 and MSM0021620859*

ⁱ *Supported by the Swiss National Science Foundation*

^j *Supported by CONACYT, México, grant 48778-F*

^k *Russian Foundation for Basic Research (RFBR), grant no 1329.2008.2*

^l *This project is co-funded by the European Social Fund (75%) and National Resources (25%) - (EPEAEK II) - PYTHAGORAS II*

^m *Supported by the Romanian National Authority for Scientific Research under the contract PN 09370101*

1 Introduction

Deep inelastic lepton-nucleon scattering (DIS) plays a pivotal role in determining the structure of the proton. The electron-proton collider HERA covers a wide range of absolute four-momentum transfer squared, Q^2 , and of Bjorken x . Previous measurements of the DIS cross section, performed by the H1 [1–6] and ZEUS [7–15] collaborations, using data at proton beam energies of $E_p = 820$ GeV and $E_p = 920$ GeV and a lepton beam energy of $E_e = 27.6$ GeV, as well as their combination [16], have enabled studies of perturbative Quantum Chromodynamics (QCD) with unprecedented precision. These measurements are complemented here with new data including the data taken at $E_p = 460$ GeV and $E_p = 575$ GeV.

At low Q^2 , the scattering cross section is defined by the two structure functions, F_2 and F_L . In a reduced form, the double differential cross section is given by

$$\sigma_r(x, Q^2) \equiv \frac{Q^4 x}{2\pi\alpha^2 [1 + (1 - y)^2]} \cdot \frac{d^2\sigma}{dx dQ^2} = F_2(x, Q^2) - \frac{y^2}{1 + (1 - y)^2} F_L(x, Q^2). \quad (1)$$

Here α is the fine structure constant and $0 \leq y \leq 1$ is the process inelasticity which is related to Q^2 , x and the centre-of-mass energy squared $s = 4E_e E_p$ by $y = Q^2/sx$. The two structure functions are defined by the cross sections for the scattering of the longitudinally and transversely polarised photons off protons σ_L and σ_T as

$$F_L(x, Q^2) = \frac{Q^2}{4\pi^2\alpha} (1 - x) \cdot \sigma_L, \quad (2)$$

$$F_2(x, Q^2) = \frac{Q^2}{4\pi^2\alpha} (1 - x) \cdot (\sigma_L + \sigma_T). \quad (3)$$

These relations are valid to good approximation at low x and imply that $0 \leq F_L \leq F_2$. To disentangle the two structure functions in a model-independent way, measurements at different values of s are required.

Using the ratio $R(x, Q^2)$, defined as

$$R = \frac{\sigma_L}{\sigma_T} = \frac{F_L}{F_2 - F_L}, \quad (4)$$

the reduced cross section in equation 1 can also be written as

$$\sigma_r = F_2(x, Q^2) \cdot \left[1 - f(y) \cdot \frac{R}{1 + R} \right], \quad (5)$$

where $f(y) = y^2/(1 + (1 - y)^2)$.

In the quark-parton model, F_2 is given by the charge squared weighted sum of the quark densities while F_L is zero because of helicity conservation. In QCD, the gluon emission gives rise to a non-vanishing F_L . Measuring the structure function F_L therefore provides a way of studying the gluon density and a test of perturbative QCD.

The contribution of the term containing F_L to the scattering cross section can be sizeable only at large values of y . For low values of y , the reduced DIS neutral current (NC) scattering cross section is well approximated by the structure function F_2 . Kinematically, for low Q^2 ,

large values of y correspond to low energies of the scattered lepton. Selecting high y events is thus complicated due to a possibly large background from hadronic final state particles.

This paper reports new measurements of the DIS cross section at low Q^2 and high y values, using data collected by the H1 collaboration in the years 2003 to 2007. The data samples are taken with dedicated high y and low Q^2 triggers. Methods relying on data are used to determine the hadronic background contribution. The first data sample consists of a new cross-section measurement for the nominal proton beam energy of $E_p = 920$ GeV for $8.5 \leq Q^2 \leq 90$ GeV² with an increased integrated luminosity of 97.6 pb⁻¹ compared to [2]. The second new data sample at $E_p = 920$ GeV covers the region $2.5 \leq Q^2 \leq 12$ GeV² using a dedicated silicon tracker for the measurement of the charge of backward scattered particles. This analysis is based on an integrated luminosity of 5.9 pb⁻¹. Two further data samples correspond to the measurements at reduced proton beam energy, $E_p = 575$ GeV and $E_p = 460$ GeV, covering the kinematic domain of $1.5 \leq Q^2 \leq 90$ GeV² with integrated luminosities of 5.9 pb⁻¹ and 12.2 pb⁻¹, respectively. Combined with the previously published H1 measurements [1,2], the data are used to measure the structure function F_L . This new measurement supersedes the previous H1 result [17].

The measurements are used to test several phenomenological and QCD models describing the low x behaviour of the DIS cross section. The phenomenological models include the power-law dependence of F_2 [18] and several dipole models [19–23] applicable at low $x < 0.01$. For the first time, dipole model analyses are extended to account for the non-negligible valence-quark contributions at small x . Fits using the DGLAP evolution equations [24–28] at NLO [29,30] are applied for $Q^2 \geq 3.5$ GeV². For the DGLAP fits, different treatments of the heavy quark contributions are compared [31–33]. A study of possible non-DGLAP contributions at low x and low Q^2 is performed by varying kinematic cuts applied to the data. The dipole and DGLAP models are compared to with other by performing fits in a common kinematic domain.

This paper is organised as follows. The measurement technique is presented in section 2. The data analysis and event selection are described in section 3. The cross section and F_L measurement procedures are explained in sections 4 and 5. Section 6 contains the phenomenological analysis of the measurement. The results presented in the paper are summarised in section 7.

2 Measurement Technique

2.1 H1 Detector

A detailed description of the H1 detector can be found in [34,35]. A view of a high y , low Q^2 event reconstructed in the H1 detector is shown in figure 1. The origin of the H1 coordinate system is the nominal ep interaction point. The direction of the proton beam defines the positive z -axis (forward direction). Transverse momenta are measured in the $x - y$ plane. Polar (θ) and azimuthal (ϕ) angles are measured with respect to the reference system.

The most relevant detector components for this analysis are the central tracker (CT), the backward lead-scintillator calorimeter (SpaCal) [36] and the liquid argon calorimeter (LAr) [37]. The central tracker consists of the central jet drift chambers (CJC1 and CJC2), the z drift chamber [38], the central inner proportional chamber (CIP) [39], the central silicon tracker

(CST) [40]. The detector operates in a 1.16 T solenoidal magnetic field. The drift chambers and the CST are used for the measurement of tracks from the hadronic final state and to determine the interaction vertex. The energy of the scattered lepton E'_e is measured by the SpaCal. The polar angle of the scattered lepton θ_e is determined by the SpaCal and the vertex position. The tracking information obtained from the backward silicon tracker (BST) [41], partially in combination with the CJC, determines the charge of the scattered electron candidate using the measured curvature. The BST is equipped with silicon pad sensors to provide a fast trigger signal. The SpaCal contains electromagnetic and hadronic sections. Its energy resolution for electromagnetic energy depositions is $\delta E/E \approx 0.07/\sqrt{E/\text{GeV}} \oplus 0.01$. It also provides a trigger based on the scattered lepton energy, time and location inside the calorimeter. The LAr allows the hadronic final state to be reconstructed. Its energy resolution was determined to be $\delta E/E \approx 0.50/\sqrt{E/\text{GeV}} \oplus 0.02$ with pion test beam data [42]. Two electromagnetic calorimeters, a tungsten/quartz-fibre sampling calorimeter (“photon tagger”) and a compact lead/scintillator calorimeter (“electron tagger”), are located close to the beam pipe at $z = -103.1$ m and $z = -6$ m, respectively. The photon tagger is used for monitoring the luminosity via the measurement of the Bethe-Heitler process $ep \rightarrow \gamma ep$. The electron tagger is used to select pure samples of photoproduction events used for background estimation.

The H1 data collection employs a four level trigger system. The first level trigger (L1) is based on various sub-detector components, which are combined at the second level (L2); the decision is refined at the third level (L3). The fully reconstructed events are subject to an additional selection at the software filter farm (L4).

2.2 Reconstruction

At HERA, the DIS kinematics can be reconstructed using the scattered lepton, the hadronic final state or a combination of both. For the measurement at high inelasticity y , however, the reconstruction of kinematics using the scattered lepton, the so called electron method, has superior resolution and is used here.

The kinematic variables in the electron method are determined by

$$y_e = 1 - \frac{E'_e(1 - \cos \theta_e)}{2E_e}, \quad Q_e^2 = \frac{E_e'^2 \sin^2 \theta_e}{1 - y_e}, \quad x_e = \frac{Q_e^2}{4E_p E_e y_e}. \quad (6)$$

Energy-momentum conservation implies that

$$2E_e \approx (E - P_z)_{\text{in}} = (E - P_z)_{\text{out}} \approx E'_e(1 - \cos \theta_e) + \sum_i (E_z - P_{z,i}) \equiv E - P_z, \quad (7)$$

where the subscripts “in” and “out” denote the total $E - P_z$ before and after the interaction, E_i ($P_{z,i}$) is the reconstructed energy (longitudinal component of the momentum) of a particle i from the hadronic final state and the sum runs over all measured hadronic final state particles. For events with hard QED initial state radiation (ISR), the radiated photon escapes in the beam pipe and $E - P_z$ is reduced. Therefore measurement of $E - P_z$ allows control of the effective beam energy and the reduction of contamination from ISR events. Requiring $E - P_z$ to be close to the nominal value also suppresses photoproduction background events, in which the scattered lepton escapes in the beam pipe.

Sample	Years	Q^2 range GeV ²	\mathcal{L}_{e^-p} pb ⁻¹	\mathcal{L}_{e^+p} pb ⁻¹	Total \mathcal{L} pb ⁻¹
Medium Q^2 CJC $E_p = 920$ GeV	2003-2005	8.5 – 90	44.4	53.2	97.6
Low Q^2 BST $E_p = 920$ GeV	2006-2007	2.5 – 12	2.5	3.4	5.9
$E_p = 575$ GeV	2007	1.5 – 90	—	5.9	5.9
$E_p = 460$ GeV	2007	1.5 – 90	—	12.2	12.2

Table 1: Data samples used in the analysis with their Q^2 coverage and integrated luminosities.

2.3 Monte Carlo Simulation

The Monte Carlo (MC) simulation is used to correct for detector acceptance and resolution effects. The inclusive DIS signal events are generated using the DJANGO [43] event generator, which also contains a simplified simulation of diffractive processes. Elastic QED Compton events are generated using the COMPTON event generator [44]. The cross section measurement is corrected for QED radiation up to order α using HERACLES [45] which is included in DJANGO. The radiative corrections are cross checked with HECTOR [46].

All generated events are passed through the full GEANT [47] based simulation of the H1 apparatus and are reconstructed using the same program chain as the data. Shower models are used to speed up the simulation in the LAr [48] and SpaCal [49] calorimeters. The calibrations of the SpaCal and the LAr, as well as the alignment, are performed for the reconstructed MC events in the same way as for the data.

3 Data Analysis

3.1 Data Sets and Event Selection

The analysis is based on several data samples which are listed in table 1. These samples are distinguished based on the kinematic region, online trigger condition, offline selection criteria and proton beam energy.

3.1.1 Online Event Selection

The two high y data samples for $E_p = 920$ GeV (‘medium Q^2 CJC $E_p = 920$ GeV’ and ‘low Q^2 BST $E_p = 920$ GeV’) are collected with dedicated low energy SpaCal triggers which require at L1 a compact energy deposit in the SpaCal with energy above 2 GeV. In addition, to suppress non- ep background, a CIP track segment pointing to the nominal interaction vertex position is required. Several additional veto conditions, which are based on scintillator counters positioned up- and downstream the nominal interaction region and on the hadronic section of the SpaCal are used to further suppress non- ep background.

The medium Q^2 CJC $E_p = 920$ GeV analysis uses an L2 trigger condition, which requires that the energy deposit is reconstructed in the outer SpaCal region, at distances from the beam

Selection criteria	Medium Q^2 CJC $E_p = 920$ GeV	Low Q^2 BST $E_p = 920$ GeV	$E_p = 460$ GeV and $E_p = 575$ GeV
Vertex z position		$ z_{\text{vtx}} < 35$ cm	
Vertex z precision		$\sigma(z_{\text{vtx}}) < 8$ cm	
Scattered lepton energy		$E'_e > 3.4$ GeV	
Radial cluster position	$40 < R_{sp} < 74$ cm	$18 < R_{sp} < 74$ cm	$18 < R_{sp} < 74$ cm
Cluster transverse shape		$R_4 > 0.8$	
		$R_{\text{log}} < 4.5$ cm for $R_{sp} > 60$ cm	
	ECRA < 4.5 cm	ECRA < 4.5 cm	—
Energy in hadronic section		$E_h/E'_e < 0.15$	
Tracker validation	$D_{\text{CJC}} < 6$ cm		$D_{\text{BC}} < 3$ cm
Lepton charge		Agree with beam charge for $y \geq 0.56$	
Energy-momentum match	—	$ E'_e/P > 0.5$ for $E'_e < 7$ GeV	
Longitudinal momentum balance		$E - P_z > 35$ GeV	
Total energy in hadronic SpaCal	—	—	$E_{h,\text{tot}} < 16$ GeV
QED Compton rejection		Topological veto	
Kinematic range	$Q^2 > 7.5$ GeV ²	$Q^2 > 2.37$ GeV ²	$Q^2 > 1.33$ GeV ²

Table 2: Selection criteria used for the analyses.

line of $R_{sp} \geq 38$ cm, corresponding approximately to the inner CJC acceptance. The low Q^2 BST $E_p = 920$ GeV analysis uses another L2 condition, which requires $R_{sp} \geq 17$ cm corresponding to the acceptance of the BST. Both triggers are further filtered at L4 using fully reconstructed events to validate low level trigger conditions.

For the reduced proton beam energy data, the main trigger is the SpaCal trigger with an energy threshold of 2 GeV. In addition a track segment has to be reconstructed in the BST pad detector or the CIP. This trigger is complemented with a SpaCal trigger at a higher energy threshold of 6.5 GeV and no tracking condition. No L4 filtering is imposed for the low E_p runs.

The data are subject to offline cuts which are listed in table 2 and discussed below. Some of the cuts are common to all data samples, others differ, primarily because of the different tracking conditions used for the scattered lepton validation.

In order to ensure an accurate kinematic reconstruction and to suppress non- ep background, the z coordinate of the interaction vertex, z_{vtx} , is required to be reconstructed close to the nominal position and with sufficient accuracy, $\sigma(z_{\text{vtx}})$.

The scattered lepton is identified with the localised energy deposition (cluster) reconstructed in the SpaCal calorimeter, which has the highest transverse energy E_T . Here E_T is calculated using the cluster energy and position, the event interaction vertex position and the beam line. If the highest E_T cluster does not satisfy all of the identification cuts mentioned below, the cluster with the second highest E_t is tried. The procedure is repeated for up to three clusters. If none of the three clusters satisfies the selection cuts, the event is rejected.

3.1.2 Offline Event Selection

The energy of the scattered lepton is required to exceed $E'_e > 3.4$ GeV to ensure a high trigger efficiency. The radial position of the scattered lepton is required to be well inside the SpaCal

acceptance and within the active trigger region.

Several cuts are applied to suppress photoproduction background. In photoproduction events, hadronic final state particles may scatter in the SpaCal calorimeter and mimic the electron signal. The main sources of such background are charged hadrons (pions, kaons and (anti-)protons) as well as $\pi^0 \rightarrow \gamma\gamma$ decays for which one of the photons converts into an e^+e^- pair prior to entering the tracking devices. The selection against photoproduction events includes cuts on the transverse shower radius, estimated using logarithmic (R_{\log}) and square root (ECRA) energy weighting [49], as well as the fraction of energy of the cluster contained in the four highest energy cells, R_4 . The cut $R_4 > 0.8$ is found to be more efficient than the cluster radius estimators, but an L4 condition requires the ECRA cut to be used for the $E_p = 920$ GeV analyses. The transverse shape requirements are efficient against hadronic background as well as background from $\pi^0 \rightarrow \gamma\gamma$ where the two photon clusters merge together.

The cut on the fraction of energy in the hadronic SpaCal behind the lepton candidate cluster, $E_h/E'_e < 0.15$, rejects purely hadronic background. The cut does not reject background for $R_{sp} > 60$ cm because of the limited acceptance of the hadronic SpaCal. As a compromise between signal efficiency and background rejection, an extra cut $R_{\log} < 4.5$ cm is introduced for $R_{sp} > 60$ cm.

The photoproduction background is suppressed further by requiring cluster validation by a track (“track link”). The medium Q^2 CJC $E_p = 920$ GeV analysis uses tracks reconstructed solely in the CJC tracker. The other analyses use a dedicated reconstruction algorithm which combines information obtained from the CJC, BST, event vertex and the SpaCal (“BC” algorithm [50]). The tracks are extrapolated to the SpaCal position and required to match the SpaCal cluster within $D_{\text{CJC}} < 6$ cm for the CJC reconstruction and within $D_{\text{BC}} < 3$ cm for the BC algorithm. The tighter cut on the track-cluster matching for the BC compared to the CJC algorithm is possible for low R_{sp} because of accurate BST θ_e reconstruction and for higher R_{sp} because the SpaCal cluster is used in the BC algorithm and pulls the track towards the cluster. As discussed below, in section 3.2, the measured scattered lepton charge is required to match the beam charge for $y > 0.56$. The sample for which the charges are different is used to estimate the remaining background. For $E'_e < 7$ GeV, the momentum reconstruction is accurate enough and $|E'_e/P_e| > 0.5$ is required, where P_e is the track momentum of the electron candidate.

The total energy reconstructed in the hadronic section of the SpaCal, $E_{h,\text{tot}}$, is required to be below 16 GeV for the $E_p = 460$ GeV and $E_p = 575$ GeV data. This avoids a trigger inefficiency arising from a veto on the total energy deposited in the hadronic SpaCal.

Events with high energy initial state photon radiation are rejected by requiring $E - P_z > 35$ GeV. This cut is also efficient against the photoproduction background. The QED Compton process, $ep \rightarrow ep\gamma$, is suppressed using a topological cut against events with two back-to-back electromagnetic clusters reconstructed in the SpaCal.

Distributions of the variables which are used for the scattered lepton identification are shown for the $E_p = 460$ GeV sample in figure 2. While the shapes observed in the data are sometimes not perfectly reproduced by the simulation, those differences occur far from the cut values. The electron identification selection criteria are designed to have high efficiency for the signal while rejecting a significant amount of the background.

3.2 Background Subtraction

At low E'_e , corresponding to high y , the background contribution after the event selection is of a size comparable to the DIS signal. To reduce the systematic uncertainty, the background determination in this analysis relies on data. Two distinct methods are applied depending on the event inelasticity y . For high $y \geq 0.56$, the background estimation is based on a sample of events, in which the charge of the lepton candidate is opposite to the beam charge (“wrong charge method”). For lower $y < 0.56$ the background contamination is small, however, the uncertainty due to the charge determination becomes large, and an alternative method is employed. In this method the background is estimated using a sub-sample of events, in which the scattered lepton is detected in the electron tagger (“tagger method”).

The wrong charge subtraction method relies on the approximate charge symmetry of the background and a good charge reconstruction with the tracker at low momenta. The residual charge asymmetry of the background is defined as

$$\kappa_+ = \frac{N_+^{\text{bg}}}{N_-^{\text{bg}}}, \quad \kappa_- = 1/\kappa_+ = \frac{N_-^{\text{bg}}}{N_+^{\text{bg}}}, \quad (8)$$

where N_{\pm}^{bg} is the number of background events in which the lepton candidate is associated with a positively (for $+$) and a negatively (for $-$) charged track. The charge asymmetry of the background arises from the different response of the SpaCal to particles compared to antiparticles (in particular p and \bar{p}) and detector misalignments. The asymmetry depends on the electron identification cuts since they alter the ratio of the electromagnetic to hadronic components of the background.

The charge asymmetry is measured directly from the data by comparing background estimates from the e^+p and e^-p scattering periods as well as using clean background samples with the scattered lepton measured in the electron tagger. The charge asymmetry of the background is found to deviate from unity by 5% and 1% for scattering angles between 155° and 174° .

The scattered lepton charge may be misidentified which leads to an overestimation of the background at $y > 0.56$. The charge reconstruction is studied in the background free sample at $E'_e > 15$ GeV by comparing events with correctly and wrongly reconstructed lepton charge. The fraction of wrongly reconstructed events depends on both the energy and the angle of the scattered electron. This dependence is well reproduced by the simulation. The fraction is smaller at small E'_e due to a larger track curvature and at small θ_e since the CJC has a better momentum resolution than the BST.

Charge reconstruction at low energy ($E'_e < 15$ GeV) is studied using events with initial state radiation in which the radiative photon is detected in the photon tagger. For these events, the sum of the scattered electron and photon energies, $E_{e+\gamma}$, peaks at the beam energy which allows the estimation of the residual background using a side-band method. This procedure is illustrated for the combined $E_p = 460$ GeV and $E_p = 575$ GeV dataset in figure 3. The DIS signal is approximated by a Gaussian while the background is assumed to follow an exponential distribution. The Gaussian width of the signal distribution is fixed to be the same for both lepton candidate charges. The data are fitted by the sum of signal and background hypotheses. From

these fits, the fraction of events with wrongly reconstructed charge in the data is determined to be $(1.1 \pm 0.2_{\text{stat}})\%$, compared to 0.6% in the simulation. The simulation is corrected for the 0.5% difference and a systematic uncertainty of 0.5% is used for the charge determination of the lepton candidate.

The tagger method of background estimation used at low $y < 0.56$ relies on an accurate determination of the tagger acceptance, A_{tag} , which is defined in this analysis as the fraction of background events in which the scattered electron is tagged. The acceptance is measured by comparing all wrong charge events with $E'_e < 8$ GeV passing nominal selection cuts to those in which a scattered electron candidate is detected in the electron tagger. For this selection, the wrong charge sample is almost entirely comprised of photoproduction events with a small admixture of DIS events with charge misidentification, which is subtracted using the MC estimate. The tagger acceptance is seen to vary between $(16.9 \pm 0.2_{\text{stat}})\%$ for the medium Q^2 CJC $E_p = 920$ GeV e^- sample, taken in the year 2005, and $(20.5 \pm 0.4_{\text{stat}})\%$ for the $E_p = 575$ GeV sample. This difference in acceptance may be explained by differences in the beam optics. Stability of the tagger acceptance for different kinematic ranges is studied by varying the θ_e and E'_e cuts. A systematic uncertainty of 20% is assigned to the tagger acceptance. This uncertainty also accounts for a potential variation of the acceptance as a function of E'_e and θ_e . Finally, to avoid a subtraction of overlapping DIS and Bethe-Heitler events containing energy deposits in the electron tagger, in the background estimation the tagged events are also required to have a charge opposite to the lepton beam charge. Neglecting the background charge asymmetry, this reduces the number of tagged background events by a factor of two.

To summarise, the number of signal events for the e^+p and e^-p running periods is estimated as

$$N_{\text{sig}}^{e^{\pm}p} = \begin{cases} N_{\pm}^{e^{\pm}p} - \kappa_{\pm} N_{\mp}^{e^{\pm}p} & \text{for } y \geq 0.56, \\ N_{\pm}^{e^{\pm}p} - \frac{2}{A_{\text{tag}}} N_{\mp\text{tag}}^{e^{\pm}p} & \text{for } y < 0.56. \end{cases} \quad (9)$$

Here $N_{\pm}^{e^{\pm}p}$ ($N_{\mp}^{e^{\pm}p}$) is the number of events with the charge of the lepton candidate the same as (opposite to) the lepton beam charge and $N_{\mp\text{tag}}^{e^{\pm}p}$ is the number of tagged events with the charge of the lepton candidate opposite to the lepton beam charge.

3.3 Efficiencies

The efficiency of the electron identification cuts is studied in the data and MC, and the simulation is adjusted accordingly.

3.3.1 Online Selection and Vertex Efficiency

The efficiencies of the triggers used in the analysis are determined using events collected with independent triggers. The efficiency of the L1 energy condition is checked with tracker-based triggers. It is found to be fully efficient for $E'_e > 3$ GeV.

The efficiency of the L1 tracking condition (CIP or BST for $E_p = 460$ GeV and $E_p = 575$ GeV data) is checked using events triggered by SpaCal-based triggers without tracking

conditions. The efficiency of the L1 tracking condition is correlated with the vertex efficiency. To avoid biases, a combined efficiency is calculated as

$$\epsilon_{(\text{CIP}||\text{BST})\&\text{VTX}} = \epsilon_{\text{CIP}||\text{BST}} \cdot \epsilon_{\text{VTX}|(\text{CIP}||\text{BST})} \quad (10)$$

where $\epsilon_{\text{CIP}||\text{BST}}$ is the CIP or BST L1 condition efficiency based on events without vertex cut and $\epsilon_{\text{VTX}|(\text{CIP}||\text{BST})}$ is the vertex efficiency for the events passing the CIP or BST tracking condition. A similar decomposition is used for the $\epsilon_{\text{CIP}\&\text{VTX}}$ condition, used for $E_p = 920$ GeV data.

The CIP L1 condition is found to have uniform efficiency for $R_{\text{sp}} > 30$ cm, i.e. within the CIP acceptance. The efficiency varies for different periods between 95% and 98.5%. For lower radii, the efficiency decreases by about 2% since the scattered lepton leaves the CIP acceptance. This region is covered by the BST pad detector and for the combined CIP||BST condition, there is no drop of the efficiency.

The efficiency $\epsilon_{\text{VTX}|(\text{CIP}||\text{BST})}$ decreases at low $R_{\text{sp}} < 40$ cm and high $y > 0.5$ since the scattered lepton as well as part of the hadronic final state leave the CJC acceptance. The decrease in the efficiency occurs mostly for diffractive events which have a rapidity gap between the proton remnant and the struck quark. For $R_{\text{sp}} < 20$ cm at $y = 0.85$, the inefficiency in the data reaches 8% compared to 5% in the Monte Carlo simulation. The difference in the efficiency is parameterised as a function of R_{sp} and E'_e and is applied to the simulation.

3.3.2 Offline Selection Efficiency

The determination of the offline electron selection efficiencies at high y is complicated due to the large background contamination. Thus an accurate estimation of the background is a matter of paramount importance for this analysis. As discussed in section 3.2, this estimation is provided by the wrong charge data sample, for which a track link is required for the lepton candidate.

The track-link efficiency is measured using a background free sample with $17 < E'_e < 22$ GeV and no track condition, as the fraction of events satisfying the track link requirement.

For the medium Q^2 CJC $E_p = 920$ GeV sample, the SpaCal cluster is linked with a track from the CJC. It is observed that the track-link efficiency has a radial dependence which is well reproduced by the MC simulation. For the overall level of inefficiency, however, the MC prediction has to be downgraded by 3.6%, 3.3% and 5% for the 2003-2004, 2004-2005 and the 2006-2007 running periods, respectively. The track-link efficiency for the low Q^2 BST $E_p = 920$ GeV, $E_p = 460$ GeV and $E_p = 575$ GeV analyses has radial and azimuthal dependencies in the BST and BST-CJC overlap regions. It has a typical value of 90% but drops in some regions to 75%. The simulation is corrected in radial steps of 2 cm in the $18 \leq R_{\text{sp}} \leq 45$ cm range for the 12 BST azimuthal sectors individually. This correction does not exceed 10%. The correction factors to the MC are applied for all lepton energies. A cross check for low E'_e events is performed using a sample of ISR events for which a good agreement between the data and corrected MC is observed.

The transverse and longitudinal distributions of the electromagnetic shower energies (“shower shapes”) are affected by the amount of material passed through by the scattered lepton before entering the calorimeter. The total amount of material before the SpaCal depends on the

scattering angle and varies between 1.7 and 1.2 radiation lengths. A detailed map of the detector material is included in the simulation. The distribution of the material in the CT is checked using reconstructed photon conversions and nuclear interactions. A significant contribution to the material budget is due to the BST sensors, cooling circuit and readout electronics. The contribution due to the readout electronics is determined using the transverse shower shapes. The method exploits the fact that the BST was removed from the H1 detector for repair during the 2005 data taking. A comparison of the shower shapes in the data and MC simulation for the 2005 and 2006 data taking periods thus allows a check of the BST material contribution with high accuracy.

The signal efficiencies of the other offline selection cuts listed in table 2 are studied after the background subtraction described in section 3.2. Since the background is large and its level typically varies significantly upon applying these cuts, a variation of the background asymmetry is also considered for each cut of the electron identification. The background subtraction is the dominant systematic uncertainty for the efficiency determination. It is measured with 3% accuracy for $y > 0.8$, with 1.5% for $0.7 < y < 0.8$ and with 1% for $y < 0.7$.

3.4 Calibration and Alignment

The alignment and calibration of the H1 detector follows a procedure similar to that described in [1]. The alignment starts with the internal alignment of the CT and proceeds to the backward detectors, SpaCal and BST. The alignment of the BST sensors is performed with the minimisation package Millepede [51] by using position information from the central tracker and the SpaCal. The global alignment of the BST is refined by requiring a matching between the momentum and energy measurements in the BST, CJC and the SpaCal [50].

The calibration of the SpaCal electromagnetic energy scale uses the double angle method [1]. The linearity of the SpaCal energy response is checked using $\pi^0 \rightarrow \gamma\gamma$, $J/\psi \rightarrow e^+e^-$ and QED Compton events.

The hadronic final state is reconstructed using information from the central tracker, the LAr calorimeter and the SpaCal. The tracker momentum scale is checked by reconstructing narrow resonances such as $K_S^0 \rightarrow \pi^+\pi^-$ and $\Lambda \rightarrow p^\pm\pi^\mp$ decays. The hadronic calibration of the LAr calorimeter employs the transverse energy balance between the scattered electron and the hadronic final state as described in [1]. The hadronic calibration of the SpaCal employs the longitudinal momentum balance. The relative contribution of the SpaCal to $E-P_z$ becomes large at high y and the absolute calibration is obtained for $E'_e < 15$ GeV by requiring $E-P_z$ to peak at $2E_e$ for both the data and the Monte Carlo simulation. The calibration constants are determined separately for the electromagnetic and hadronic sections of the SpaCal.

3.5 Radiative Corrections

For large inelasticity $y > 0.5$ and low x the kinematics reconstruction using the electron method is prone to large radiative corrections which can reach a level of more than 50% of the Born cross section. Studies based on the DJANGO and HECTOR programs show that the largest radiative contribution arises because of hard initial state radiation from the incoming lepton.

The hard ISR process is strongly suppressed by the cut $E - P_z > 35$ GeV. After this cut, the radiative corrections amount to about 10% of the Born cross section with no strong dependence on y . A slight increase in the corrections occurs at the highest $y > 0.7$ due to QED Compton events. These events are efficiently rejected using the topological cut against two back-to-back clusters in the SpaCal.

Events rejected by the cut $E - P_z > 35$ GeV can be used to study the description by the simulation of the hard ISR. This is illustrated in figure 4 which shows the background subtracted $E - P_z$ distribution for events passing all cuts excluding the $E - P_z$ cut for the $E_p = 575$ GeV sample. The sample is restricted to $E'_e < 5$ GeV which corresponds to $y > 0.8$. A prominent peak for $E - P_z \approx 10$ GeV corresponds to the hard ISR process. The data in this kinematic region are well described by the simulation.

3.6 Control Distributions

Data and MC distributions of the main quantities used to reconstruct the event kinematics for the events passing all selection criteria are compared in figures 5 to 8 for all data sets included in the analysis. The MC distributions are normalised to the integrated luminosity and corrected for selection efficiency differences, as explained above. The control distributions illustrate the considerable level of background for low E'_e , that is estimated from the data. The DIS simulation uses the H1PDF2009 set of parton distributions [2]. There is a good overall agreement observed between the measurements and predictions. The local residual differences, visible for the energy distribution in the lowest Q^2 , BST sample near to $E'_e \simeq 10$ GeV and corresponding to $y_e \simeq 0.7$ (figure 7a and figure 7d), do not affect the cross-section measurement.

3.7 Systematic Uncertainties

The systematic uncertainty on the cross-section measurements arises from several contributions. Besides the global normalisation uncertainty, these contributions are classified as correlated uncertainties, which affect measurements at different Q^2, x in a correlated manner, and as uncorrelated ones, for which each of the measurements is affected individually. The summary of all systematic uncertainties is given in table 3.

The global normalisation uncertainty is 3% for the $E_p = 920$ GeV period and 4% for the $E_p = 460$ GeV and $E_p = 575$ GeV analyses. The uncertainty includes the uncertainty of the luminosity measurement as well as global trigger and reconstruction efficiency uncertainties.

The uncertainty on the SpaCal electromagnetic energy scale is determined to be 0.2% at $E'_e = 27.5$ GeV increasing to 1% at $E'_e = 2$ GeV for all but the medium Q^2 CJC $E_p = 920$ GeV analysis. The latter covers a large period of runs, from the year 2003 to 2005, and therefore is prone to variations of the SpaCal performance. For this analysis the scale uncertainty is 0.3% at $E'_e = 27.5$ increasing to 1% at $E'_e = 2$ GeV. The uncertainty at around 27.5 GeV is estimated from the difference between the result of the double-angle calibration and the position of the kinematic peak. The uncertainty at $E'_e = 2$ GeV is obtained using $J/\psi \rightarrow e^+e^-$ and $\pi^0 \rightarrow \gamma\gamma$ decays [1].

Correlated uncertainty source	Uncertainty
Global normalisation	3% for $E_p = 920$ GeV run 4% for $E_p = 460$ GeV and $E_p = 575$ GeV run
E'_e energy scale	0.2% at 27.5 to 1% at 2 GeV (all, but medium Q^2 CJC $E_p = 920$ GeV) 0.3% at 27.5 to 1% at 2 GeV (medium Q^2 CJC $E_p = 920$ GeV)
Polar angle θ_e	0.5 mrad
Hadronic energy scale	4%
LAr noise	20%
Background charge asymmetry	2%
Electron tagger acceptance	20%
Uncorrelated uncertainty source	Uncertainty
Trigger efficiency	1%
Track-cluster link efficiency	1.5%
Lepton charge determination	1%
Electron identification efficiency	1 – 3%
Radiative corrections	1%

Table 3: Summary of systematic uncertainties. For the correlated error sources, the uncertainties are given in terms of the uncertainty in the corresponding source. For the uncorrelated error sources, the uncertainties are given in terms of the effect on the measured cross section.

The uncertainty on the lepton polar angle is 0.5 mrad, which covers uncertainties of the alignment of the SpaCal as well as of the cluster position determination.

The hadronic energy scale has an uncertainty of 4%. Apart from reconstruction in the LAr calorimeter and in the tracker, this value covers the uncertainty of the hadronic energy scale of the SpaCal, which is important at high y . The uncertainty of the LAr electronic noise and beam related background is 20%. These uncertainties have little impact on the cross-section measurement which is based on the electron method since they enter only via the $E - P_z$ cut.

The background charge asymmetry is determined with a precision of 2%. It affects only the data for $y \geq 0.56$ where the wrong charge subtraction method is used. Its uncertainty has negligible impact on the medium Q^2 CJC $E_p = 920$ GeV and low Q^2 BST $E_p = 920$ GeV measurements since these are based on both e^+p and e^-p HERA running periods and have a charge symmetric background sample. For the $E_p = 460$ GeV and $E_p = 575$ GeV runs, the impact on the cross section reaches 3.5% at $y = 0.85$.

The electron tagger acceptance is known to 20%. This uncertainty is applied for $y < 0.56$ only and, since the background at low y is small, this source does not have a significant impact on the measurement.

The uncorrelated systematic uncertainties include the Monte Carlo statistical errors and the following sources: the uncorrelated part of the trigger efficiency, known to 1%; the track-cluster

Sample	Bin boundaries in y									
$E_p = 460$ GeV			0.9	0.8	0.7	0.6	0.38	0.24	0.15	0.095
$E_p = 575$ GeV	0.896	0.80	0.72	0.64	0.56	0.48	0.304	0.192	0.12	0.076
$E_p = 920$ GeV	0.56	0.50	0.45	0.40	0.35	0.30	0.19	0.12	0.075	0.0475

Table 4: Bin boundaries in $y = Q^2/sx$ for the cross-section analyses at different E_p used to measure the structure function F_L .

link efficiency, known to 1.5%; the uncertainty of the lepton charge determination of 0.5% leading to 1% uncertainty of the cross section, for $y \geq 0.56$ only; the electron identification uncertainty varies from 3% for $y > 0.8$ to 1% for $y < 0.6$; the uncertainty due to the radiative corrections is determined to be 1%.

4 Cross Section Determination

4.1 Method

At low Q^2 the contributions to the NC scattering process are completely dominated by photon exchange with negligible differences between the e^+p and e^-p scattering cross sections. The background determination at high y is based on the measured lepton-candidate charge. In order to reduce the sensitivity to the background charge asymmetry, the cross section is determined for a charge symmetric data sample for the medium Q^2 CJC $E_p = 920$ GeV and the low Q^2 BST $E_p = 920$ GeV samples. The reduced cross section is calculated in this case for each x, Q^2 bin as

$$\sigma_r(x, Q^2) = \frac{N_{\text{sig}}^{e^-p} + N_{\text{sig}}^{e^+p} \frac{\mathcal{L}^{e^-p}}{\mathcal{L}^{e^+p}}}{N_{\text{sig,MC}}^{e^-p} \frac{\mathcal{L}^{e^-p}}{\mathcal{L}_{\text{MC}}^{e^-p}} + N_{\text{sig,MC}}^{e^+p} \frac{\mathcal{L}^{e^-p}}{\mathcal{L}_{\text{MC}}^{e^+p}}} \sigma_r^{\text{MC}}(x, Q^2). \quad (11)$$

Here $\mathcal{L}^{e^\pm p}$ ($\mathcal{L}_{\text{MC}}^{e^\pm p}$) is the integrated luminosity for the data (MC), $N_{\text{sig,MC}}^{e^\pm p}$ is the number of signal events in the MC and $\sigma_r^{\text{MC}}(x, Q^2)$ is the value of the reduced cross section in the MC.

Equation 11 is rather insensitive to the uncertainty of the background charge asymmetry κ_\pm since for $y \geq 0.56$, the total background is estimated as $N_{bg} = \kappa_- N_+^{e^-p} + \kappa_+ N_-^{e^+p} (\mathcal{L}^{e^-p} / \mathcal{L}^{e^+p})$. The statistical accuracy of equation 11 is limited by the sample with the smaller luminosity, therefore the data taking strategy was tuned to obtain e^+p and e^-p samples of about equal size.

For the $E_p = 460$ GeV and $E_p = 575$ GeV samples, the absence of e^-p data does not allow for usage of equation 11, and a more standard cross section determination formula is used as

$$\sigma_r(x, Q^2) = \frac{N_{\text{sig}}^{e^+p}}{N_{\text{sig,MC}}^{e^+p} \frac{\mathcal{L}^{e^+p}}{\mathcal{L}_{\text{MC}}^{e^+p}}} \sigma_r^{\text{MC}}(x, Q^2). \quad (12)$$

These cross sections are therefore more sensitive to the uncertainty in κ_\pm .

The medium Q^2 CJC $E_p = 920$ GeV and low Q^2 BST $E_p = 920$ GeV samples extend the published H1 measurements to high y and for them the same mixed $(Q^2, x) - (Q^2, y)$ binning is adapted as used in [1]. The $E_p = 460$ GeV and $E_p = 575$ GeV samples are used to measure the structure function F_L . For this measurement, an optimal binning is in (Q^2, y) with the y boundaries of the bins adjusted so that the corresponding $x = Q^2/(4E_e \cdot E_p \cdot y)$ values agree for different E_p . This binning is given in table 4. Bin centres are calculated as an arithmetic average of the bin boundaries. Apart from the $E_p = 460$ GeV and $E_p = 575$ GeV samples, the binning is also employed in the reanalysis of the published H1 data at $E_p = 920$ GeV for the F_L measurement, as is discussed below, in section 5. The purity and stability [1] of the cross-section measurements are typically above 70% at highest y reducing to about 50% at lowest y .

4.2 Results

The cross-section measurements are given in tables 10-15 and shown in figure 9. The new data cover the range between 1.5 GeV^2 and 90 GeV^2 in Q^2 reaching values of inelasticity y as high as 0.85.

For the $E_p = 920$ GeV sample, the new data can be compared to the previous H1 results [1, 2]. For the high y region, the precision of the new data is significantly better than that of the previous H1 result, apart from the global normalisation uncertainty that is larger for the new result. This uncertainty is significantly reduced by combining the H1 measurements.

4.3 Combination of Data

For the proton beam energy $E_p = 920$, the new data cover a phase space similar to previous H1 results [1,2] which are based on HERA-I data, collected in the years 1994 to 2000. Therefore the data are combined, following the procedure described in [1,52].

Four data sets are considered in this combination: the combined H1 results from HERA-I [1,2], reported for $E_p = 820$ GeV and $E_p = 920$ GeV, and the two new data sets, medium Q^2 CJC $E_p = 920$ GeV and low Q^2 BST $E_p = 920$ GeV. The systematic uncertainties are assumed to be uncorrelated between the HERA-I and HERA-II measurements, apart from a 0.5% overall normalisation uncertainty due to the theoretical uncertainty on the Bethe-Heitler process cross section used for the luminosity measurement. In total, there are 46 independent sources of systematic uncertainty. For $Q^2 \geq 12 \text{ GeV}^2$, the new data extend the kinematic coverage towards high $y > 0.6$. At low $y < 0.6$ and for all values of y at low Q^2 , there is a sizable region of overlap.

The combined cross-section measurements are given in tables 16 to 19. The full information about correlation between cross-section measurements can be found elsewhere [53]. The data show very good compatibility, with $\chi^2/n_{\text{dof}} = 15.4/36$. At low y , the previous H1 data from [1, 2] have a higher precision than the new result. In particular, the global normalisation uncertainty was significantly smaller: about 1% at HERA-I compared to 3% at HERA-II. Therefore, in the combination, the new HERA-II data are effectively normalised to the HERA-I result and their global normalisation uncertainties are reduced significantly. Table 5 lists those few systematic

Systematic Source	Shift in σ	Uncertainty in σ
E'_e scale	-0.25	0.85
θ_e	0.14	0.84
\mathcal{L}_{CJC}	0.03	0.96
\mathcal{L}_{BST}	-0.30	0.37

Table 5: Shifts of the central values and reduction of the uncertainty of the systematic error sources in the combination of the medium Q^2 CJC $E_p = 920$ GeV and low Q^2 BST $E_p = 920$ GeV data sets with HERA-I data, expressed as fractions of the original uncertainty.

sources of the HERA-II analyses, which are noticeably altered by the averaging procedure. All alterations stay within one standard deviation of the estimated error.

The systematic errors of the HERA-I data are not significantly affected by the combination. At low y , the gain in the combined data precision compared to the HERA-I result is small. The uncertainties are reduced by at most 5% of their size and the shift of central values does not exceed 0.2%. At high y , however, there is a significant gain in the precision achieved by the data combination. For the region $2.5 \leq Q^2 < 12$ GeV² and $y = 0.8$, for example, the accuracy of the $E_p = 920$ GeV data is improved by about a factor of two. For medium Q^2 , $12 \leq Q^2 \leq 35$ GeV², the new high y measurements, corresponding to $E_p = 920$ GeV, exceed the accuracy of the HERA-I data, corresponding to $E_p = 820$ GeV, by a factor 1.5 to 2. The $E_p = 920$ GeV measurement at HERA-I was limited to $y \leq 0.6$.

The $E_p = 460$ GeV and $E_p = 575$ GeV data sets are measured using an identical grid of (Q^2, x) bin centres. At low y , the influence of the structure function F_L is small. Therefore the two data sets are combined for all (Q^2, x) points satisfying $y_{460} = Q^2 / (4E_e \cdot 460 \text{ GeV} \cdot x) < 0.35$ after a small correction of the cross-section values to $E_p = 575$ GeV. At higher y the measurements are kept separately but they are affected by the combination procedure. The data show good compatibility, with $\chi^2 / n_{\text{dof}} = 17.2/27$, and the combined reduced cross-section values are given in tables 20 and 21. This combined reduced E_p set, together with the combined nominal E_p set, is used for the phenomenological analysis presented in section 6.

5 Determination of the Structure Function F_L

5.1 Procedure

The structure function F_L is determined using the separate $E_p = 460$ GeV and $E_p = 575$ GeV samples and the published 920 GeV data from [1,2]. To determine F_L , common values of the (x, Q^2) grid centres are required for all centre-of-mass energies. The published 920 GeV data have therefore been reanalysed using the binning adopted for the F_L analysis, see table 4. To determine F_L , the data measured at high y for $E_p = 460$ GeV are combined with the data at intermediate y for $E_p = 575$ GeV and low y for $E_p = 920$ GeV. The usage of the published 920 GeV data compared to a new analysis of the HERA-II data is motivated by a wider Q^2 acceptance at low y , extending to $Q^2 = 1.5$ GeV². In addition, as discussed in section 4.3, adding the HERA-II data does not improve the precision at low y .

The determination of the structure function F_L depends on the treatment of the relative normalisations and systematic uncertainties of the data sets. A straightforward but simplified procedure was adopted in [17] where the data sets were normalised to each other at low y . The values of the structure function F_L were determined in straight-line fits to the reduced cross section as a function of $y^2/(1 + (1 - y)^2)$ in each (x, Q^2) bin using the statistical and uncorrelated systematic uncertainties. The correlated systematic errors were determined using an offset method. An illustration of this procedure, applied to the cross-section data from the current analysis, is shown in figure 10. The procedure adopted in [17] does not fully take into account correlations between the low and high y regions, used for the cross-section normalisation and the F_L computation. The offset method does not allow for shifts of the central values of the correlated systematic error sources. Thus the information on the goodness of the straight-line fits to the cross-section measurements at the three centre-of-mass energies is not fully employed.

The procedure for the F_L determination is improved in the current analysis. The new method extends the averaging procedure of [1]. For additive uncertainties it is based on the minimisation of the function

$$\chi_0^2(\mathbf{F}_2, \mathbf{F}_L, \mathbf{b}) = \sum_i \frac{[(F_2^i - f(y^i)F_L^i) - \sum_j \Gamma_j^i b_j - \mu^i]^2}{\Delta_i^2} + \sum_j b_j^2. \quad (13)$$

Here μ^i is the measured central value of the reduced cross section at a $(Q^2, x; s)$ point i with a combined statistical and uncorrelated systematic uncertainty $\Delta_i = (\Delta_{i,\text{stat}}^2 + \Delta_{i,\text{uncor}}^2)^{1/2}$. The effect of correlated error sources b_j on the cross-section measurements is approximated by the systematic error matrix Γ_j^i . The function χ_0^2 depends quadratically on the structure functions F_2^i and F_L^i (denoted as vectors $\mathbf{F}_2, \mathbf{F}_L$) as well as on b_j . Minimisation of χ_0^2 with respect to these variables leads to a system of linear equations.

For low $y \leq 0.35$, the coefficient $f(y)$ is small compared to unity and thus F_L can not be accurately measured. In this kinematic domain, the constraint $0 \leq F_L \leq F_2$ provides an even better bound on the value of F_L than the experimental data. Furthermore, the ratio R is not expected to vary strongly as a function of x in the limited x range of sensitivity to F_L . For the kinematic range studied in this paper it is measured to be consistent with $R \sim 0.25$. To avoid unphysical values for F_L , an extra prior is introduced for the χ^2 minimisation:

$$\chi^2(\mathbf{F}_2, \mathbf{F}_L, \mathbf{b}) = \chi_0^2(\mathbf{F}_2, \mathbf{F}_L, \mathbf{b}) + \sum_i \left(\frac{F_L^i - \frac{R}{R+1} F_2^i}{\Delta_{F_L}} \right)^2, \quad (14)$$

where $R = 0.25$ and the width $\Delta_{F_L} = 3$ is chosen such that it has a negligible influence for $y > 0.35$. The additional prior preserves the quadratic dependence of the χ^2 function on F_2^i and F_L^i . The prior has a significant contribution at low y only and is very similar to imposing a common cross-section normalisation at low y used in [17]. Since Δ_{F_L} is chosen to be large, the prior affects only points with large uncertainty on F_L . The bias introduced by the prior is investigated by varying the value of R between 0 and 0.5 and Δ_{F_L} between 1 and 5, and found to be negligible, for the points chosen for the F_L determination.

5.2 Results

The measured structure function $F_L(x, Q^2)$ is given in table 22 and shown in figure 11. By convention, only measurements with total uncertainties below 0.3 for $Q^2 \leq 35 \text{ GeV}^2$ and below

0.4 for $Q^2 = 45 \text{ GeV}^2$ are presented. The selection on the total uncertainty removes the bias due to the prior in equation 14. The measurement spans over two decades in x at low x , from $x = 0.00002$ to $x = 0.002$. The data are compared to the result of the DGLAP ACOT fit, which is described in section 6.2. The structure function F_2 measured for the corresponding bins is given in table 22 and shown together with F_L in figure 12. Note that compared to the previous determinations of F_2 by the H1 collaboration, this measurement represents a model independent determination without extra assumptions on F_L .

The values of $F_L(x, Q^2)$ resulting from averages over x at fixed Q^2 are given in table 23 and presented in figure 13. The average is performed taking into account correlations. The measured structure function F_L is compared with theoretical predictions from HERAPDF1.0 [16], CT10 [54], NNPDF2.1 [55,56], MSTW08 [57], GJR08 [58,59] and ABKM09 [60] sets. Depending on the PDF set, the calculations are performed at NLO or NNLO in perturbative QCD. Within the uncertainties all predictions describe the data reasonably well.

The measurement of the structure functions F_2 and F_L can be used to determine the ratio R (see equation 4). This ratio is shown in figure 14. Apart from conditions applied to select F_L results, only measurements with total uncertainties below 0.6 are included.

For $Q^2 \geq 3.5 \text{ GeV}^2$, the ratio R is consistent with a constant behaviour. This hypothesis is tested by a simultaneous determination of the values of the structure function $F_2(x, Q^2)$ at all (x, Q^2) data points under the assumption that R is constant. In this procedure, values of R are scanned between $R = 0$ and $R = 0.6$ in $\Delta R = 0.01$ steps, and each of the cross-section measurements is used to calculate the structure function $F_2(x, Q^2)$ using equation 5. The measurements of $F_2(x, Q^2)$ from different E_p are then combined using the standard averaging programme [1] taking into account correlations of the systematic uncertainties. Figure 15 shows the results of this scan represented as χ^2 for each average as a function of R . The minimum is found at $R_{\min} = 0.260 \pm 0.050$ where $\chi^2_{\min}/n_{\text{dof}} = 113.8/150$ suggesting a conservative error estimation. It is remarkable that all the low $7 \cdot 10^{-5} < x < 2 \cdot 10^{-3}$, low $3.5 \leq Q^2 \leq 45 \text{ GeV}^2$ data are consistent with the hypothesis that R is constant.

6 Phenomenological Analysis

The combined cross-section data for $E_p = 460, 575$ and $E_p = 820, 920 \text{ GeV}$ are used for several phenomenological analyses. The fits are applied to the combined reduced cross-section measurements accounting for correlations between the data points.

In the following, the quality of different fits is compared in terms of χ^2/n_{dof} . Since the systematic uncertainties dominate over statistics, and they are estimated conservatively, in several cases χ^2/n_{dof} is observed to be less than unity. This, however, does not prevent the comparison of quality among different fits with the same number of degrees of freedom in terms of $\Delta\chi^2$ since the average error overestimation, approximated as $\sqrt{\chi^2/n_{\text{dof}}}$, does not exceed 5 – 10%.

6.1 λ Fit

The increase of the structure function F_2 for $x \rightarrow 0$ can be approximated by a power law in x , $F_2 = c(Q^2)x^{-\lambda(Q^2)}$. This simple parameterisation was shown to describe previous H1 data

rather well for $x < 0.01$ [18]. In the recent H1 analysis [1], a fit was performed to the measured reduced cross section, σ_r , represented as

$$\sigma_r(Q^2, x) = c(Q^2)x^{-\lambda(Q^2)} \left[1 - \frac{y^2}{1 + (1 - y)^2} \frac{R}{1 + R} \right] \quad (15)$$

by allowing R to float for each Q^2 bin independently. At low $Q^2 \leq 10 \text{ GeV}^2$, this lead to surprisingly large values of $R \approx 0.5$, which are incompatible with the result $R \approx 0.26$ obtained in section 5.2. A similar behaviour is observed when equation 15 is applied to the present data. This points to some inconsistency in the simple power law for the rise of F_2 towards low x and the measured value of R . A different approach is therefore adopted in this analysis. It is generally assumed that $R = 0.26$ for all Q^2 bins. A fit termed the λ fit is made with only $c(Q^2)$ and $\lambda(Q^2)$ as free parameters. This is extended in a subsequent step to allow for possible deviations in the behaviour of F_2 from the simple λ fit formula.

The combined H1 data are fitted using the offset method to evaluate systematic uncertainties. The parameters obtained in the fits as a function of Q^2 are shown in figure 16. The parameter λ exhibits an approximately linear increase as a function of $\ln Q^2$ for $Q^2 \geq 2 \text{ GeV}^2$. For lower Q^2 , the variation of λ deviates from that linear dependence. The normalisation coefficient $c(Q^2)$ rises with increasing Q^2 for $Q^2 < 2 \text{ GeV}^2$ and is consistent with a constant behaviour for higher Q^2 , as in [18]. The total χ^2 of the fit is $\chi^2/n_{\text{dof}} = 538/350$ when the uncertainties are taken as the statistical and uncorrelated systematic uncertainties added in quadrature. Values of χ^2/n_{dof} significantly larger than unity may arise in the offset method because it does not take into account the correlated systematic uncertainties. Studies show that the largest contribution to the χ^2 arises from the $1 < Q^2 < 10 \text{ GeV}^2$ domain. In order to further investigate this behaviour, the parameterisation of the structure function F_2 is extended by one additional parameter

$$F_2(x, Q^2) = c(Q^2)x^{-\lambda(Q^2) + \lambda'(Q^2) \ln x} = c(Q^2) \exp[-\lambda(Q^2) \ln x + \lambda'(Q^2) \ln^2 x] \quad (16)$$

to allow for deviations from a single power law. This fit returns a significantly improved $\chi^2/n_{\text{dof}} = 405/326$. The parameters λ and λ' are shown in figure 17. From this figure, it is interesting to observe that the parameter λ becomes consistent with having a constant value of $\lambda = 0.25$. The two parameters λ and λ' are strongly correlated since for each Q^2 bin the data span over a limited range in x . Therefore, fits are performed, termed λ' fits, for which $\lambda = 0.25$ is fixed. The quality of these fits with a total $\chi^2/n_{\text{dof}} = 464/350$ is better than of the original λ fits. The fitted parameters c and λ' are shown in figure 18. A comparison of the λ' fit result with the H1 reduced cross-section data is given in figures 19 and 20. Figure 21 shows comparison of the λ and λ' fits for $Q^2 \geq 2 \text{ GeV}^2$ with the structure function F_2 which is calculated from the reduced cross sections assuming $R = 0.26$. The parameter λ' is negative and shows a constant behaviour for $Q^2 < 5 \text{ GeV}^2$, with a smooth transition and a linear rise with $\ln Q^2$ for $Q^2 > 20 \text{ GeV}^2$. Therefore, for the low Q^2 domain, the λ' fit shows somewhat softer increase towards low x compared to the λ fit opposite to that observed for higher Q^2 values. The present measurement of R therefore leads to a refined understanding of the rise of F_2 towards low x , which appears to be tamed at low Q^2 , and correspondingly lower x , compared to a pure power-law behaviour, as it was predicted in [61].

In order to consolidate the observations obtained with the offset method, an analysis is performed in which the errors are evaluated using the Hessian method following the χ^2 definition given in [2]. The fitted parameters are 2×24 coefficients $c(Q^2)$, $\lambda(Q^2)$ or $c(Q^2)$, $\lambda'(Q^2)$ for the 24 Q^2 bins and the parameters for the sources of the systematic uncertainty. The λ' fit returns $\chi^2/n_{\text{dof}} = 345.7/350$ compared to a worse $\chi^2/n_{\text{dof}} = 370.5/350$ of the λ fit.

6.2 DGLAP Fit

The new combined H1 data are used together with the previously published high $Q^2 \geq 90 \text{ GeV}^2$ H1 data [4–6] as input to a DGLAP pQCD fit analysis to NLO, with the main objective of studying F_L predictions. The HERA measurement regions are limited by $W_{min}^2 = 300 \text{ GeV}^2$ and $x_{max} = 0.65$, such that target mass corrections and higher twist contributions can be assumed to be small. In addition, in order to restrict to a region where perturbative QCD is valid, only data with $Q^2 \geq Q_{min}^2 = 3.5 \text{ GeV}^2$ are used in the central fit. The influence of this value is discussed further in this section. The internal consistency of the input data set enables a calculation of the experimental uncertainties on the PDFs using the χ^2 tolerance criterion of $\Delta\chi^2 = 1$. The data are fitted using the program QCDNUM [62] and the complete error correlation information in a χ^2 fit as in [2] using MINUIT [63] as the minimisation program.

The fit procedure begins with parameterising the input parton distribution functions (PDFs) at a starting scale $Q_0^2 = 1.9 \text{ GeV}^2$, chosen to be below the charm mass threshold. The PDFs are then evolved using the DGLAP evolution equations [24–28] at NLO [29,30] in the \overline{MS} scheme with the renormalisation and factorisation scales set to Q^2 , and the strong coupling to $\alpha_s(M_Z) = 0.1176$ [64]. The QCD predictions for the structure functions are obtained by convoluting the PDFs with the calculable NLO coefficient functions. Those are calculated using the general mass variable-flavour scheme of ACOT [33] and cross checked against the RT scheme [31,32]. The ACOT and RT schemes differ in the inclusion of various terms at higher orders in α_s for the computation of the heavy quark structure functions, and for the structure function F_L .

For the QCD fit, the following independent input PDFs are chosen: the valence quark distributions xu_v and xd_v , the gluon distribution xg and anti-quark distributions $x\bar{U}$ and $x\bar{D}$. The conditions $x\bar{U} = x\bar{u}$, and $x\bar{D} = x\bar{d} + x\bar{s}$ are imposed at the starting scale Q_0^2 . A standard generic functional form is used to parameterise these PDFs:

$$xf(x) = Ax^B(1-x)^C(1+Dx+Ex^2). \quad (17)$$

The normalisation parameters, A_{u_v} , A_{d_v} and A_g , are constrained by the fermion number and momentum sum rules. The up and down quark type B parameters are set equal, $B_{\bar{U}} = B_{\bar{D}}$, such that there is only a single B parameter for the sea distributions, which governs the PDFs at low x .

The strange quark distribution is already present at the starting scale, and it is assumed that $x\bar{s} = f_s x\bar{D}$ at Q_0^2 . The strange fraction is chosen to be $f_s = 0.31$, which is consistent with determinations of this fraction using neutrino induced di-muon production data [57,65]. In addition, to ensure that $x\bar{u} \rightarrow x\bar{d}$ as $x \rightarrow 0$, the constraint $A_{\bar{U}} = A_{\bar{D}}(1 - f_s)$ is applied.

The initial fits are performed using the same parameterisation type as for the HERAPDF1.0 fit [16], which has only one free polynomial parameter, E_{u_v} . For this parameterisation, the ACOT and RT heavy flavour schemes are compared. Both fits give good descriptions of the data, but the ACOT fit, which has $\chi^2/n_{\text{dof}} = 722.7/782$, is superior to the RT fit, with $\chi^2/n_{\text{dof}} = 773.2/782$, by about 50 units. Therefore, the ACOT fit is chosen for further more detailed investigations.

The central fit is chosen in a χ^2 optimisation procedure, as previously used by H1 [2], in which all extra parameters D, E are first set to zero, leading to a nine parameter fit. They are then added, one at a time until no significant improvement in χ^2 is observed. In addition, the

Q_{min}^2 / GeV^2	1.5	2	2.5	3.5	5	7.5
χ^2 / n_{dof}	824.8/834	777.9/818	748.7/801	715.2/781	677.6/759	626.9/712

Table 6: Values of χ^2 / n_{dof} for QCD fits with different Q_{min}^2 values.

A_S	0.2	0.3	0.5	0.7	1.0	1.5
χ^2 / n_{dof}	709.5/777	696.1/762	643.1/734	617.3/709	594.4/690	554.1/654

Table 7: Values of χ^2 / n_{dof} for QCD fits with different values of the parameter A_S for saturation-inspired cut on data, see equation 18.

assumption that $B_{u_v} = B_{d_v}$ is removed and a flexible parameterisation for the gluon density with two extra parameters [16] is also tried but both variations do not lead to significant fit improvements. The parameterisation procedure also requires for the central fit that all PDFs are positive definite. The best fit is obtained with the extra free parameters D_{u_v} and E_{u_v} resulting in a $\chi^2 / n_{\text{dof}} = 715.2/781$. Figure 22 compares the fit result to the low Q^2 H1 data. As a consistency check, a fit using the RT heavy flavour scheme is repeated. A similar increase in χ^2 of about 50 units is observed in this case.

The sensitivity of the fit to the inclusion of low Q^2 data is studied by varying the Q_{min}^2 cut. The variation of the fit quality in terms of χ^2 / n_{dof} is summarised in table 6. Increasing the Q_{min}^2 cut leads to a steady decrease in the χ^2 / n_{dof} , suggesting that the fit has some difficulties to describe the data at low Q^2 values. Figure 23 compares the structure function F_2 with the fits performed using different Q_{min}^2 cuts. At low Q^2 the shape of the measured structure function F_2 as a function of x is somewhat different from those obtained by the DGLAP fits based on the parameterisation described above. The fit obtained with a Q_{min}^2 cut of 7.5 GeV² falls significantly below the data at small x when extrapolating to the low Q^2 region. Figure 24 shows gluon and sea-quark distributions for different values of Q_{min}^2 at the evolution starting scale $Q_0^2 = 1.9 \text{ GeV}^2$. A change of Q_{min}^2 from 1.5 GeV² to 7.5 GeV² leads to an increase of the gluon distribution while the sea-quark distribution becomes smaller at low x . This suppression of the sea-quark contribution at small x when using a Q_{min}^2 cut of 7.5 GeV² is responsible for the smaller values of F_2 obtained by this fit at small Q^2 and small x .

An alternative approach to the Q_{min}^2 variation is a saturation-inspired cut on the kinematic region depending on x like

$$Q^2 \geq A_S x^{-\lambda_S}, \quad (18)$$

with $\lambda_S = 0.3$ and different values of the parameter A_S , as suggested in [66]. The dependence of χ^2 / n_{dof} on A_S is given in table 7. Figure 25 shows gluon and sea-quark distributions for different values of A_S . The saturation-inspired cut has an effect similar to the one of the Q_{min}^2 variation. The fit quality improves with increasing A_S and the gluon becomes larger while the sea-quark density decreases at low x .

To facilitate the comparison of the data with dipole model predictions, DGLAP fits are also performed in the kinematic domain $x < 0.01$ and $Q^2 \geq 3.5 \text{ GeV}^2$, in which both the DGLAP theory and the dipole ansatz can be assumed to hold. The valence quark parameters cannot be determined in this range. Therefore they are fixed to the values obtained by the full phase space fits. There are six non-valence quark parameters, $B_g, C_g, A_{\bar{D}}, B_{\bar{D}}, C_{\bar{D}}$ and $C_{\bar{U}}$, as compared

to three free parameters of the dipole models discussed below. When restricted to this common kinematic domain, the ACOT fit is of very good quality, with $\chi^2/n_{\text{dof}} = 248.3/249$ while the RT fit yields $\chi^2/n_{\text{dof}} = 288.8/249$.

6.3 Dipole Model Fits

At low x and low Q^2 , virtual photon-proton scattering has been described using the colour dipole model [19]. In this model, the scattering process is calculated as a fluctuation of the photon into a quark-antiquark pair (dipole), with a lifetime $\propto 1/x$, which interacts with the proton.

Several approaches were developed to phenomenologically describe the dipole-proton interaction cross section, three of which are subsequently applied to the data of this paper. These are the original model version (GBW) [20], a model based on the colour glass condensate approach to the high parton density regime (IIM) [21], and a model with the generalised impact parameter dipole saturation (B-SAT) [22].

In the GBW model the dipole-proton cross section $\hat{\sigma}$ is given by

$$\hat{\sigma}(x, r) = \sigma_0 \left\{ 1 - \exp \left[-r^2 / (4r_0^2(x)) \right] \right\}, \quad (19)$$

where r corresponds to the transverse separation between the quark and the antiquark, and r_0^2 is an x dependent scale parameter, assumed to have the form

$$r_0^2(x) \sim (x/x_0)^\lambda. \quad (20)$$

The parameters of the fit are the cross-section normalisation σ_0 as well as x_0 and λ . The IIM model has a modified expression for $\hat{\sigma}$ using the parameter R_{IIM} instead of σ_0 . The B-SAT model modifies equation 19 by adding effects of the DGLAP evolution. This model uses as an input a gluon density

$$xg(x, Q_0^2) = A_g x^{-\lambda_g} (1-x)^{5.6} \quad (21)$$

with the starting scale Q_0^2 , normalisation A_g and low x exponent λ_g as free parameters while the other dipole model parameters are kept fixed.

The dipole models are applicable at low $x < 0.01$ where the gluon and sea quark densities dominate. The models are valid down to the photoproduction limit $Q^2 \approx 0$, therefore no Q^2 cut is applied for the central fits. In DGLAP fits it is observed that the contribution of the valence quarks to the ep scattering cross section is sizeable for the whole HERA kinematic range, compared to the data precision. This contribution varies between 5% and 15% for x varying from 0.0001 to 0.01. Modified dipole fits are therefore performed, in which the contribution from the valence quarks to the cross section, as determined by the central DGLAP fit, is added to the dipole model prediction. These fits are performed requiring that $Q^2 \geq 3.5 \text{ GeV}^2$, to be consistent with DGLAP analyses.

It should be noted that the size of the valence-quark contribution at low x is rather uncertain because it is only indirectly constrained by the HERA data. For $x > 0.01$ it is determined by the combination of neutral and charged current scattering cross sections measurements. At lower x however the valence quark contribution follows from the parameterisation and the fermion number sum rules. The uncertainty can reach $\sim 30\%$ at $x = 0.0001$ [16].

Parameter	Value	Uncertainty	Value	Uncertainty	Value	Uncertainty
	Nominal GBW		$Q^2 \geq 3.5 \text{ GeV}^2$ GBW		GBW+DGLAP_{valence}	
σ_0 (mb)	21.7	0.7	18.4	0.7	17.7	0.7
λ	0.287	0.002	0.296	0.003	0.336	0.003
x_0	1.76×10^{-4}	0.25×10^{-4}	3.50×10^{-4}	0.60×10^{-4}	3.46×10^{-4}	0.57×10^{-4}
	Nominal IIM		$Q^2 \geq 3.5 \text{ GeV}^2$ IIM		IIM+DGLAP_{valence}	
R_{IIM} (fm)	0.611	0.007	0.595	0.007	0.666	0.009
λ	0.258	0.004	0.260	0.004	0.289	0.005
x_0	0.48×10^{-4}	0.06×10^{-4}	0.61×10^{-4}	0.08×10^{-4}	0.15×10^{-4}	0.03×10^{-4}
	Nominal B-SAT		$Q^2 \geq 3.5 \text{ GeV}^2$ B-SAT		B-SAT+DGLAP_{valence}	
A_g	2.32	0.06	2.38	0.09	1.66	0.05
λ_g	0.088	0.010	0.073	0.014	0.099	0.011
Q_0^2 (GeV ²)	2.25	0.18	2.04	0.20	1.51	0.11

Table 8: Parameters and total uncertainties for GBW, IIM and B-SAT dipole model fits for various fit conditions described in the text. The $Q^2 \geq 3.5 \text{ GeV}^2$ and DGLAP_{valence} fits are performed in a kinematic phase spaces restricted to $Q^2 \geq 3.5 \text{ GeV}^2$.

Dipole models fits are performed using the same minimisation package as for the DGLAP fit. The values of parameters and their uncertainties are estimated using a Monte Carlo method [67]¹. The parameters of the fits are given in table 8. The fit qualities are summarised together with the results obtained for DGLAP fits in table 9. Among the dipole models, the IIM fit provides the best description of the data. It is shown in figures 26 and 27. The B-SAT model, which includes some DGLAP evolution, provides a worse fit to the data yet still with an acceptable χ^2/n_{dof} . The GBW model, however, fails to describe the data. This fit agrees with the data well at low Q^2 , but falls significantly below the data for $Q^2 \geq 25 \text{ GeV}^2$, where the DGLAP evolution, neglected in the model, plays an important role. Fits with a DGLAP-based correction for the contribution of the valence quarks are restricted to $Q^2 \geq 3.5 \text{ GeV}^2$. In order to simplify comparisons, pure dipole model fits with the same Q^2 cut are performed too. The addition of the valence-quark contribution allows an acceptable description of the data at high x , however, the overall fit quality is reduced. The fitted parameters of the models vary beyond their experimental uncertainties. As an example, a comparison of the reduced cross-section data to the IIM+DGLAP_{valence} fit is given in figure 28.

Finally, the fits at $x < 0.01$ and $Q^2 \geq 3.5 \text{ GeV}^2$ are compared in terms of χ^2/n_{dof} for the three dipole and two DGLAP models (table 9). The best description is obtained with the ACOT fit, followed by the pure dipole model IIM and B-SAT fits. The DGLAP RT fit is of similar quality as the IIM+DGLAP_{valence} fit, followed by the B-SAT+DGLAP_{valence} fit. The GBW fit fails to describe the data in this kinematic domain.

In both the DGLAP and the dipole models the structure function F_L can be calculated once the model parameters are fixed. It is thus of interest to compare the F_L predictions of the different models with the data, which is illustrated in figure 29. For high $Q^2 > 10 \text{ GeV}^2$, all models agree with the data and with each other well. For lower Q^2 values, there is a significant

¹The Monte Carlo method is preferred for the estimation of uncertainties compared to the MINUIT error estimation in order to avoid instabilities of numerical integration used in the Dipole codes.

Fit Conditions	χ^2/n_{dof}				
	GBW	IIM	B-SAT	ACOT	RT
Nominal fit	718.8/352	397.6/352	424.9/352	715.2/781	764.5/781
$Q^2 \geq 3.5 \text{ GeV}^2$	559.7/252	259.4/252	261.7/252		
DGLAP _{valence}	739.5/252	287.6/252	371.4/252	248.3/249	288.8/249

Table 9: Quality of fits in terms of χ^2/n_{dof} for GBW, IIM and B-SAT dipole model as well as ACOT and RT DGLAP models for various fit conditions described in the text. The $Q^2 \geq 3.5 \text{ GeV}^2$ and DGLAP_{valence} fits are performed in a kinematic phase space restricted to $Q^2 \geq 3.5 \text{ GeV}^2$ and $x < 0.01$ which is valid for both dipole and DGLAP models.

difference between the predictions. The DGLAP fit in the RT scheme predicts low values of F_L , while in the DGLAP fit in the ACOT scheme the decrease of F_L occurs at lower values of Q^2 . The predictions of the dipole models considered here show only little variation with Q^2 . All predictions, except the DGLAP RT fit, agree with the data well. The Q^2 dependence of F_L is best reproduced by the DGLAP ACOT fit.

7 Summary

A measurement is presented of the inclusive double differential cross section for neutral current deep inelastic $e^\pm p$ scattering at small Bjorken x and low absolute four-momentum transfers squared, Q^2 . The measurement extends to high values of inelasticity y . The data were collected with the H1 detector for the proton beam energy of $E_p = 920 \text{ GeV}$, in the years 2003 to 2006, and for $E_p = 575 \text{ GeV}$ and $E_p = 460 \text{ GeV}$, in 2007. The integrated luminosities of the measurements are 103.5 pb^{-1} , 5.9 pb^{-1} and 12.2 pb^{-1} for the $E_p = 920 \text{ GeV}$, $E_p = 575 \text{ GeV}$ and $E_p = 460 \text{ GeV}$ data samples, respectively. The data at $E_p = 920 \text{ GeV}$ significantly improve the accuracy of the cross-section measurements at high y when compared to the previous H1 data. All data are combined with the HERA-I results to provide a new accurate data sample covering $0.2 \leq Q^2 \leq 150 \text{ GeV}^2$, $5 \times 10^{-6} < x < 0.15$ and $0.005 < y \leq 0.85$ which supersedes previous H1 measurements of the DIS cross section and of F_2 in this kinematic domain.

The data at $E_p = 460 \text{ GeV}$ and $E_p = 575 \text{ GeV}$, together with the measurements at $E_p = 920 \text{ GeV}$ are used to determine the structure function F_L . This extraction applies a novel method which takes into account the correlations of data points due to systematic uncertainties. This is the first measurement at low $1.5 \leq Q^2 \leq 45 \text{ GeV}^2$ and $2.7 \times 10^{-5} < x < 2 \times 10^{-3}$, which became possible by employing a dedicated backward silicon tracker for the electron reconstruction. The data are reasonably well reproduced by the predictions based on NLO and NNLO QCD.

The measurements of F_L are used to determine the ratio $R = F_L/(F_2 - F_L)$. For $Q^2 \geq 3.5 \text{ GeV}^2$, the ratio R shows a constant behaviour with $R = 0.260 \pm 0.050$.

The combined H1 data are subjected to phenomenological analyses. The rise of the structure function F_2 towards low x is examined using power-law fits. As in previous H1 analyses, the power-law exponent λ is found to be approximately constant for $Q^2 \leq 2 \text{ GeV}^2$ but increases

linearly with $\ln Q^2$ for higher Q^2 values. Closer inspection of the fits reveals, however, a deterioration of the fit quality for the $1 \leq Q^2 \leq 10 \text{ GeV}^2$ range. A parameterisation which allows for a Q^2 dependent $\ln x$ correction to a fixed power-law, for $\lambda = 0.25$, provides an improved description of the data with the same number of parameters. This observation suggests that the x dependence of the structure function F_2 may deviate from a simple power law at small x and small Q^2 exhibiting a softer rise. This confirms a QCD prediction of [61], according to which the rise of F_2 should be slower than any power of $1/x$ but faster than any power of $\ln 1/x$.

The data are found to be well described by an NLO DGLAP QCD analysis. The ACOT and the RT schemes are used, which differ in the treatment of the heavy-flavour and higher-order F_L contributions to the cross section. A comparison of ACOT and RT based fits to the data reveals a significant preference for the ACOT treatment.

The sensitivity of the DGLAP fits to low Q^2 and low x effects is checked by varying the Q_{min}^2 of the data and also by applying a saturation-model inspired [66] selection of the data. While for all variants of the cuts the fits provide a good description of the data, the fit quality improves as more data at low x and low Q^2 are removed from the analysis. This also leads to an increase of the gluon and a decrease of the sea-quark densities at low x .

Dipole model based analyses are applied to the data at $x < 0.01$ using three variants of them. The GBW model is unable to describe the data at larger Q^2 , while the IIM and B-SAT models agreed with the data generally well. The influence of valence quarks at low x is investigated by adding their contribution as estimated from the ACOT fit. These models together with the two DGLAP fits are compared to each other by fitting the data in a common kinematic range. The DGLAP ACOT fit provides the best description of the data, followed closely by the dipole IIM and B-SAT models. All models agree well with the F_L measurement at $Q^2 > 10 \text{ GeV}^2$. For lower Q^2 , however, the RT fit falls significantly below the data while the other models describe the measured F_L well.

The present measurement and the combination with all accurate H1 DIS cross section data provide a total cross section uncertainty of about 1% at low Q^2 and low x . The structure function $F_2(x, Q^2)$ rises towards low x . The structure function $F_L(x, Q^2)$ is measured directly. Both structure functions agree with pQCD expectations.

Acknowledgements

We are grateful to the HERA machine group whose outstanding efforts have made this experiment possible. We thank the engineers and technicians for their work in constructing and maintaining the H1 detector, our funding agencies for financial support, the DESY technical staff for continual assistance and the DESY directorate for support and for the hospitality which they extend to the non-DESY members of the collaboration.

References

- [1] F. Aaron *et al.* [H1 Collaboration], Eur. Phys. J. **C63**, 625 (2009) [[arXiv:0904.0929](https://arxiv.org/abs/0904.0929)].

- [2] F. Aaron *et al.* [H1 Collaboration], Eur. Phys. J. **C64**, 561 (2009) [[arXiv:0904.3513](#)].
- [3] C. Adloff *et al.* [H1 Collaboration], Eur. Phys. J. **C21**, 33 (2001) [[hep-ex/0012053](#)].
- [4] C. Adloff *et al.* [H1 Collaboration], Eur. Phys. J. **C13**, 609 (2000) [[hep-ex/9908059](#)].
- [5] C. Adloff *et al.* [H1 Collaboration], Eur. Phys. J. **C19**, 269 (2001) [[hep-ex/0012052](#)].
- [6] C. Adloff *et al.* [H1 Collaboration], Eur. Phys. J. C **30**, 1 (2003) [[hep-ex/0304003](#)].
- [7] J. Breitweg *et al.* [ZEUS Collaboration], Phys. Lett. **B407**, 432 (1997) [[hep-ex/9707025](#)].
- [8] J. Breitweg *et al.* [ZEUS Collaboration], Phys. Lett. B **487**, 53 (2000) [[hep-ex/0005018](#)].
- [9] J. Breitweg *et al.* [ZEUS Collaboration], Eur. Phys. J. **C7**, 609 (1999) [[hep-ex/9809005](#)].
- [10] S. Chekanov *et al.* [ZEUS Collaboration], Eur. Phys. J. C **21**, 443 (2001) [[hep-ex/0105090](#)].
- [11] J. Breitweg *et al.* [ZEUS Collaboration], Eur. Phys. J. C **12**, 411 (2000) [Erratum-ibid. **C27** (2003) 305] [[hep-ex/9907010](#)].
- [12] S. Chekanov *et al.* [ZEUS Collaboration], Eur. Phys. J. **C28**, 175 (2003) [[hep-ex/0208040](#)].
- [13] S. Chekanov *et al.* [ZEUS Collaboration], Phys. Lett. **B539**, 197 (2002), [Erratum-ibid. **B552** (2003) 308] [[hep-ex/0205091](#)].
- [14] S. Chekanov *et al.* [ZEUS Collaboration], Phys. Rev. D **70**, 052001 (2004) [[hep-ex/0401003](#)].
- [15] S. Chekanov *et al.* [ZEUS Collaboration], Eur. Phys. J. **C32**, 1 (2003) [[hep-ex/0307043](#)].
- [16] F. Aaron *et al.* [H1 and ZEUS Collaborations], JHEP **1001**, 109 (2010) [[arXiv:0911.0884](#)].
- [17] F. Aaron *et al.* [H1 Collaboration], Phys. Lett. **B665**, 139 (2008) [[arXiv:0805.2809](#)].
- [18] C. Adloff *et al.* [H1 Collaboration], Phys. Lett. **B520**, 183 (2001) [[hep-ex/0108035](#)].
- [19] N. N. Nikolaev and B. G. Zakharov, Z. Phys. C **49**, 607 (1991).
- [20] K. Golec-Biernat and M. Wüsthoff, Phys. Rev. D **59**, 014017 (1999) [[hep-ph/9807513](#)].
- [21] E. Iancu, K. Itakura, and S. Munier, Phys. Lett. **B590**, 199 (2004) [[hep-ph/0310338](#)].
- [22] H. Kowalski, L. Motyka, and G. Watt, Phys. Rev. D **74**, 074016 (2006) [[hep-ph/0606272](#)].
- [23] J. L. Albacete, N. Armesto, J. G. Milhano, and C. A. Salgado, Phys. Rev. **D80**, 034031 (2009) [[arXiv:0902.1112](#)].
- [24] V. N. Gribov and L. N. Lipatov, Sov. J. Nucl. Phys. **15**, 438 (1972).
- [25] V. N. Gribov and L. N. Lipatov, Sov. J. Nucl. Phys. **15**, 675 (1972).
- [26] L. N. Lipatov, Sov. J. Nucl. Phys. **20**, 94 (1975).

- [27] Y. L. Dokshitzer, Sov. Phys. JETP **46**, 641 (1977).
- [28] G. Altarelli and G. Parisi, Nucl. Phys. B **126**, 298 (1977).
- [29] G. Curci, W. Furmanski, and R. Petronzio, Nucl.Phys. **B175**, 27 (1980).
- [30] W. Furmanski and R. Petronzio, Phys.Lett. **B97**, 437 (1980).
- [31] R. S. Thorne and R. G. Roberts, Phys. Rev. D **57**, 6871 (1998) [[hep-ph/9709442](#)].
- [32] R. S. Thorne, Phys. Rev. **D73**, 054019 (2006) [[hep-ph/0601245](#)].
- [33] M. Kramer, F. I. Olness, and D. E. Soper, Phys. Rev. **D62**, 096007 (2000) [[hep-ph/0003035](#)].
- [34] I. Abt *et al.* [H1 Collaboration], Nucl. Instr. and Meth. A **386**, 310 (1997).
- [35] I. Abt *et al.* [H1 Collaboration], Nucl. Instr. and Meth. A **386**, 348 (1997).
- [36] R. D. Appuhn *et al.* [H1 SpaCal Group], Nucl. Instr. and Meth. A **386**, 397 (1997).
- [37] B. Andrieu *et al.* [H1 Calorimeter Group], Nucl. Instrum. Meth. **A336**, 460 (1993).
- [38] H. Barwolff *et al.*, Nucl. Instrum. Meth. **A283**, 467 (1989).
- [39] J. Becker *et al.*, Nucl. Instrum. Meth. **A586**, 190 (2008).
- [40] D. Pitzl *et al.*, Nucl. Instr. and Meth. A **454**, 334 (2000) [[hep-ex/0002044](#)].
- [41] W. Eick *et al.*, Nucl. Instr. and Meth. A **386**, 81 (1997).
- [42] B. Andrieu *et al.* [H1 Calorimeter Group], Nucl. Instrum. Meth. **A336**, 499 (1993).
- [43] G. A. Schuler and H. Spiesberger, in *Physics at HERA, vol. 3*, edited by W. Buchmüller and G. Ingelman (1991), pp. 1419–1432, DJANGO 1.4.
- [44] A. Courau and P. Kessler, Phys. Rev. **D46**, 117 (1992), COMPTON 2.2.
- [45] A. Kwiatkowski, H. Spiesberger, and H.-J. Moehring, Comp. Phys. Comm. **69**, 155 (1992).
- [46] A. Arbuzov *et al.*, Comp. Phys. Comm. **94**, 128 (1996), HECTOR 1.0 [[hep-ph/9511434](#)].
- [47] R. Brun *et al.*, *GEANT3 User's Guide*, CERN (1987) [[CERN-DD/EE 84-01](#)].
- [48] G. Grindhammer, M. Rudowicz, and S. Peters, Nucl. Instr. and Meth. A **290**, 469 (1990).
- [49] A. Glazov, N. Raicevic, and A. Zhokin, Comput. Phys. Commun. **181**, 1008 (2010).
- [50] S. Piec, Doctoral thesis, Humboldt-Universität zu Berlin (2009), [<http://www-h1.desy.de/psfiles/theses/h1th-546.pdf>].
- [51] V. Blobel and C. Kleinwort, *A new method for the high precision alignment of track detectors* (2002) [[hep-ex/0208021](#)].

- [52] A. Glazov, AIP Conf. Proc. **792**, 237 (2005).
- [53] Correlation information can be found at <https://www.desy.de/h1/>.
- [54] H.-L. Lai *et al.*, Phys. Rev. **D82**, 074024 (2010) [[arXiv:1007.2241](#)].
- [55] R. D. Ball *et al.*, Nucl. Phys. **B838**, 136 (2010), [[arXiv:1002.4407](#)].
- [56] S. Forte, E. Laenen, P. Nason, and J. Rojo, Nucl. Phys. **B834**, 116 (2010) [[arXiv:1001.2312](#)].
- [57] A. D. Martin, W. J. Stirling, R. S. Thorne, and G. Watt (2009) [[arXiv:0901.0002](#)].
- [58] M. Gluck, P. Jimenez-Delgado, and E. Reya, Eur. Phys. J. **C53**, 355 (2008) [[arXiv:0709.0614](#)].
- [59] M. Gluck, P. Jimenez-Delgado, E. Reya, and C. Schuck, Phys. Lett. **B664**, 133 (2008) [[arXiv:0801.3618](#)].
- [60] S. Alekhin, J. Blumlein, S. Klein, and S. Moch, Phys. Rev. **D81**, 014032 (2010) [[arXiv:0908.2766](#)].
- [61] A. De Rujula *et al.*, Phys. Rev. **D10**, 1649 (1974).
- [62] M. Botje (2010), <http://www.nikef.nl/h24/qcdnum/index.html> [[arXiv:1005.1481](#)].
- [63] F. James and M. Roos, Comput. Phys. Commun. **10**, 343 (1975).
- [64] C. Amsler *et al.* (Particle Data Group), Phys. Lett. **B667**, 1 (2008).
- [65] P. M. Nadolsky *et al.*, Phys. Rev. **D78**, 013004 (2008) [[arXiv:0802.0007](#)].
- [66] F. Caola, S. Forte, and J. Rojo, Phys. Lett. **B686**, 127 (2010) [[arXiv:0910.3143](#)].
- [67] A. Glazov, S. Moch, and V. Radescu, Accepted by Phys. Lett. B doi:10.1016/j.physletb.2003.10.071 (2010) [[arXiv:1009.6170](#)].

Q^2 GeV ²	x	y	σ_r	δ_{stat} %	δ_{unc} %	δ_{tot} %	$\gamma_{E'_e}$ %	γ_{θ_e} %	γ_{had} %	γ_{noise} %	γ_{acntag} %
2.5	2.900×10^{-5}	0.85	0.828	5.70	4.29	7.28	1.26	-0.15	0.52	0.53	0.00
2.5	3.290×10^{-5}	0.75	0.816	3.99	3.27	5.36	1.13	-0.72	0.35	0.42	0.00
2.5	3.790×10^{-5}	0.65	0.896	6.91	4.76	9.20	3.70	-0.76	-0.05	-0.05	0.00
3.5	4.060×10^{-5}	0.85	0.809	6.13	4.17	7.57	1.11	0.96	0.33	0.35	0.00
3.5	4.600×10^{-5}	0.75	0.971	3.04	2.99	4.35	0.42	-0.63	0.28	0.35	0.00
3.5	5.310×10^{-5}	0.65	0.887	3.09	2.64	4.12	0.53	-0.17	0.21	0.20	0.00
3.5	8.000×10^{-5}	0.43	0.952	5.62	3.66	7.28	1.60	-2.00	0.31	0.44	1.07
5.0	5.800×10^{-5}	0.85	0.939	6.41	4.13	7.81	1.46	0.58	0.35	0.47	0.00
5.0	6.580×10^{-5}	0.75	1.002	2.84	2.87	4.15	0.74	-0.39	0.32	0.36	0.00
5.0	7.590×10^{-5}	0.65	1.094	1.71	2.29	3.08	1.02	-0.39	0.24	0.24	0.00
5.0	1.300×10^{-4}	0.38	1.050	3.14	2.24	4.27	1.40	-1.00	0.18	0.26	0.56
6.5	7.540×10^{-5}	0.85	1.133	6.23	4.15	7.55	0.02	0.89	0.29	0.34	0.00
6.5	8.550×10^{-5}	0.75	1.077	2.83	2.82	4.25	1.07	0.85	0.32	0.34	0.00
6.5	9.860×10^{-5}	0.65	1.134	2.09	2.31	3.29	0.89	0.45	0.24	0.23	0.00
6.5	1.300×10^{-4}	0.49	1.115	1.51	1.86	2.55	0.71	-0.15	0.17	0.18	0.40
6.5	2.000×10^{-4}	0.32	1.082	1.72	1.91	2.85	0.85	-0.89	0.03	0.05	0.07
6.5	3.200×10^{-4}	0.20	1.054	3.17	2.25	4.11	0.94	-0.94	0.00	0.00	0.16
8.5	9.860×10^{-5}	0.85	1.146	6.46	4.05	7.71	1.07	-0.04	0.37	0.35	0.00
8.5	1.118×10^{-4}	0.75	1.102	3.31	2.82	4.46	0.84	0.43	0.22	0.22	0.00
8.5	1.290×10^{-4}	0.65	1.200	1.69	2.22	3.04	1.11	0.38	0.21	0.21	0.00
8.5	2.000×10^{-4}	0.42	1.206	1.24	1.80	2.29	0.56	0.27	0.13	0.17	0.17
8.5	3.200×10^{-4}	0.26	1.118	1.38	1.82	2.42	0.80	0.03	0.00	0.00	0.04
12.0	1.392×10^{-4}	0.85	1.238	5.34	3.97	6.80	1.36	0.10	0.21	0.25	0.00
12.0	1.578×10^{-4}	0.75	1.313	3.41	2.82	4.47	0.45	0.29	0.23	0.26	0.00
12.0	1.821×10^{-4}	0.65	1.244	2.51	2.30	3.54	0.73	0.54	0.23	0.20	0.00
12.0	2.000×10^{-4}	0.59	1.258	1.67	2.20	2.98	0.94	0.52	0.17	0.19	0.00

Table 10: Reduced cross section σ_r , as measured with the low Q^2 BST $E_p = 920$ GeV data sample. The uncertainties are quoted in % relative to σ_r . δ_{stat} is the statistical uncertainty, δ_{unc} represents the uncorrelated systematic uncertainty and δ_{tot} is the total uncertainty determined as the quadratic sum of systematic and statistical uncertainties. $\gamma_{E'_e}$, γ_{θ_e} , γ_{had} , γ_{noise} and γ_{acntag} are the bin-to-bin correlated systematic uncertainties in the cross section measurement due to uncertainties in the SpaCal electromagnetic energy scale, electron scattering angle, calorimeter hadronic energy scale, LAr calorimeter noise and electron tagger acceptance, respectively. The global normalisation uncertainty of 3% is not included in δ_{tot} .

Q^2 GeV ²	x	y	σ_r	δ_{stat} %	δ_{unc} %	δ_{tot} %	$\gamma_{E'_e}$ %	γ_{θ_e} %	γ_{had} %	γ_{noise} %	γ_{acctag} %
8.5	9.860×10^{-5}	0.85	1.172	2.22	3.75	4.44	0.76	0.09	0.29	0.33	0.00
12.0	1.392×10^{-4}	0.85	1.304	1.47	3.71	4.09	0.77	0.06	0.28	0.29	0.00
12.0	1.578×10^{-4}	0.75	1.394	1.72	2.71	3.38	0.98	0.05	0.28	0.25	0.00
15.0	1.741×10^{-4}	0.85	1.349	1.37	3.71	4.06	0.72	0.34	0.31	0.30	0.00
15.0	1.973×10^{-4}	0.75	1.400	0.93	2.64	2.83	0.26	0.10	0.25	0.25	0.00
15.0	2.276×10^{-4}	0.65	1.342	1.80	2.33	2.99	0.37	-0.12	0.26	0.20	0.00
20.0	2.321×10^{-4}	0.85	1.396	1.52	3.73	4.12	0.71	0.32	0.28	0.25	0.00
20.0	2.630×10^{-4}	0.75	1.439	0.83	2.63	2.92	0.73	0.50	0.25	0.21	0.00
20.0	3.035×10^{-4}	0.65	1.391	0.76	2.16	2.35	0.41	0.13	0.24	0.19	0.00
25.0	2.901×10^{-4}	0.85	1.482	2.46	3.86	4.64	0.65	-0.06	0.32	0.23	0.00
25.0	3.288×10^{-4}	0.75	1.450	0.88	2.64	2.84	0.33	0.31	0.24	0.20	0.00
25.0	3.794×10^{-4}	0.65	1.469	0.73	2.16	2.40	0.55	0.43	0.24	0.19	0.00
25.0	5.000×10^{-4}	0.49	1.403	0.69	1.77	2.12	0.74	0.09	0.22	0.19	0.51
25.0	8.000×10^{-4}	0.31	1.281	1.10	1.85	2.28	0.70	0.19	0.10	0.12	0.08
35.0	4.603×10^{-4}	0.75	1.457	1.23	2.68	3.01	0.33	0.36	0.29	0.21	0.00
35.0	5.311×10^{-4}	0.65	1.483	0.66	2.15	2.34	0.31	0.43	0.26	0.19	0.00
35.0	8.000×10^{-4}	0.43	1.404	0.48	1.75	2.02	0.78	0.29	0.18	0.17	0.16
35.0	1.300×10^{-3}	0.27	1.236	0.63	1.77	1.99	0.64	0.01	0.01	0.02	0.01
35.0	2.000×10^{-3}	0.17	1.112	1.42	1.93	2.73	1.25	-0.35	0.00	0.00	0.00
45.0	6.341×10^{-4}	0.70	1.470	1.00	2.21	2.58	0.79	0.28	0.28	0.18	0.00
45.0	8.000×10^{-4}	0.55	1.488	0.69	2.16	2.47	0.85	0.41	0.22	0.19	0.00
45.0	1.300×10^{-3}	0.34	1.316	0.45	1.75	1.94	0.50	0.45	0.08	0.09	0.04
45.0	2.000×10^{-3}	0.22	1.182	0.52	1.76	1.94	0.54	0.30	0.00	0.00	0.03
60.0	1.302×10^{-3}	0.45	1.419	0.61	1.77	1.97	0.42	0.35	0.18	0.14	0.00
60.0	2.000×10^{-3}	0.30	1.248	0.50	1.76	1.95	0.40	0.56	0.02	0.03	0.02
60.0	3.200×10^{-3}	0.18	1.102	0.71	1.78	2.12	0.83	0.33	0.00	0.00	0.02
90.0	2.004×10^{-3}	0.44	1.354	0.79	1.80	2.09	0.56	0.42	0.09	0.08	0.00
90.0	3.200×10^{-3}	0.28	1.183	0.60	1.77	1.95	0.44	0.32	0.00	0.00	0.00
90.0	5.000×10^{-3}	0.18	1.018	1.50	1.96	2.50	0.29	0.33	0.00	0.00	0.00

Table 11: Reduced cross section σ_r , as measured with the medium Q^2 CJC $E_p = 920$ GeV data sample. Description of the columns is given in the caption of table 10.

Q^2 GeV ²	x	y	σ_r	δ_{stat} %	δ_{unc} %	δ_{tot} %	$\gamma_{E'_e}$ %	γ_{θ_e} %	γ_{had} %	γ_{noise} %	γ_{asym} %	γ_{acntag} %
1.5	3.480×10^{-5}	0.850	0.520	8.10	4.96	10.16	0.69	0.08	0.45	0.58	3.47	0.00
2.0	4.640×10^{-5}	0.850	0.704	4.57	4.31	6.89	1.10	-0.81	0.49	0.59	2.34	0.00
2.0	5.260×10^{-5}	0.750	0.717	4.59	3.93	6.38	1.64	-0.64	0.32	0.45	0.86	0.00
2.5	5.800×10^{-5}	0.850	0.777	4.18	4.16	6.73	2.01	-0.31	0.60	0.64	2.36	0.00
2.5	6.580×10^{-5}	0.750	0.768	2.64	3.03	4.24	0.91	0.42	0.42	0.37	0.74	0.00
2.5	7.590×10^{-5}	0.650	0.711	4.32	3.45	5.82	1.33	-1.12	0.23	0.33	0.40	0.00
3.5	8.120×10^{-5}	0.850	0.794	4.21	4.05	6.41	0.82	0.62	0.38	0.57	2.32	0.00
3.5	9.210×10^{-5}	0.750	0.820	2.22	2.86	4.09	1.71	0.30	0.31	0.38	0.63	0.00
3.5	1.062×10^{-4}	0.650	0.857	2.03	2.47	3.69	1.73	-0.43	0.32	0.32	0.26	0.00
3.5	1.409×10^{-4}	0.490	0.797	2.55	2.45	4.31	1.32	-1.66	0.24	0.25	0.00	1.19
5.0	1.160×10^{-4}	0.850	0.939	4.19	4.01	6.60	1.92	0.46	0.45	0.51	2.37	0.00
5.0	1.315×10^{-4}	0.750	0.924	2.07	2.80	3.82	1.28	0.58	0.34	0.37	0.54	0.00
5.0	1.517×10^{-4}	0.650	0.966	1.69	2.33	3.10	1.02	-0.25	0.25	0.30	0.21	0.00
5.0	2.013×10^{-4}	0.490	0.914	1.16	1.87	2.48	0.66	-0.59	0.19	0.20	0.00	0.65
6.5	1.509×10^{-4}	0.850	1.034	4.26	4.02	6.55	0.94	0.88	0.41	0.50	2.57	0.00
6.5	1.710×10^{-4}	0.750	0.958	2.15	2.80	3.79	0.94	0.65	0.39	0.43	0.51	0.00
6.5	1.973×10^{-4}	0.650	1.007	1.60	2.30	2.92	0.64	0.39	0.23	0.25	0.17	0.00
6.5	2.617×10^{-4}	0.490	1.008	0.90	1.82	2.26	0.83	0.20	0.20	0.22	0.00	0.40
6.5	4.136×10^{-4}	0.310	0.962	1.14	1.87	2.44	1.00	-0.39	0.00	0.01	0.00	0.00
8.5	1.973×10^{-4}	0.850	0.969	4.68	4.01	7.05	1.28	0.64	0.40	0.49	3.05	0.00
8.5	2.236×10^{-4}	0.750	1.008	2.38	2.84	3.95	0.92	0.79	0.21	0.26	0.59	0.00
8.5	2.580×10^{-4}	0.650	1.087	1.66	2.32	3.30	1.40	0.80	0.22	0.23	0.15	0.00
8.5	3.422×10^{-4}	0.490	1.051	0.85	1.81	2.25	0.92	0.18	0.19	0.21	0.00	0.31
8.5	5.409×10^{-4}	0.310	1.016	0.91	1.82	2.10	0.44	0.23	0.01	0.01	0.00	0.02
8.5	8.384×10^{-4}	0.200	0.939	1.01	1.84	2.29	0.90	0.14	0.00	0.00	0.00	0.00
8.5	1.397×10^{-3}	0.120	0.857	1.21	1.89	2.55	1.11	-0.48	0.00	0.00	0.00	0.00
12.0	2.785×10^{-4}	0.850	1.127	3.90	3.98	6.07	0.97	0.19	0.34	0.41	2.13	0.00
12.0	3.156×10^{-4}	0.750	1.110	2.38	2.85	3.92	1.00	0.10	0.34	0.33	0.59	0.00
12.0	3.642×10^{-4}	0.650	1.095	1.86	2.36	3.15	0.58	0.67	0.22	0.22	0.18	0.00
12.0	4.831×10^{-4}	0.490	1.108	0.89	1.81	2.25	0.58	0.76	0.15	0.16	0.00	0.17
12.0	7.636×10^{-4}	0.310	1.028	0.87	1.81	2.22	0.79	0.50	0.01	0.01	0.00	0.01
12.0	1.184×10^{-3}	0.200	0.972	0.93	1.83	2.22	0.85	0.06	0.00	0.00	0.00	0.00
12.0	1.973×10^{-3}	0.120	0.880	1.07	1.86	2.57	1.37	0.34	0.00	0.00	0.00	0.00
15.0	3.481×10^{-4}	0.850	1.218	3.90	4.06	5.91	0.57	0.33	0.29	0.30	1.60	0.00
15.0	3.945×10^{-4}	0.750	1.109	2.33	2.84	3.77	0.30	0.36	0.30	0.31	0.53	0.00
15.0	4.552×10^{-4}	0.650	1.138	2.05	2.40	3.44	1.06	0.78	0.25	0.24	0.24	0.00
15.0	6.039×10^{-4}	0.490	1.161	0.96	1.83	2.31	0.87	0.45	0.20	0.18	0.00	0.13
15.0	9.545×10^{-4}	0.310	1.049	0.91	1.82	2.21	0.52	0.68	0.00	0.01	0.00	0.04
15.0	1.479×10^{-3}	0.200	0.939	0.95	1.83	2.28	0.81	0.55	0.00	0.00	0.00	0.00
15.0	2.466×10^{-3}	0.120	0.859	1.06	1.85	2.68	1.61	0.17	0.00	0.00	0.00	0.00

Table 12: Reduced cross section σ_r , as measured with the $E_p = 460$ GeV data sample. The uncertainties are quoted in % relative to σ_r . δ_{stat} is the statistical uncertainty. δ_{unc} represents the uncorrelated systematic uncertainty. δ_{tot} is the total uncertainty determined as the quadratic sum of systematic and statistical uncertainties. $\gamma_{E'_e}$, γ_{θ_e} , γ_{had} , γ_{noise} , γ_{asym} and γ_{acntag} are the bin-to-bin correlated systematic uncertainties in the cross section measurement due to uncertainties in the SpaCal electromagnetic energy scale, electron scattering angle, calorimeter hadronic energy scale, LAr calorimeter noise, background charge asymmetry and electron tagger acceptance, respectively. The global normalisation uncertainty of 4% is not included in δ_{tot} .

Q^2 GeV ²	x	y	σ_r	δ_{stat} %	δ_{unc} %	δ_{tot} %	$\gamma_{E'_e}$ %	γ_{θ_e} %	γ_{had} %	γ_{noise} %	γ_{asym} %	γ_{acctag} %
20.0	4.642×10^{-4}	0.850	1.003	5.34	4.21	7.12	1.20	0.59	0.46	0.46	1.47	0.00
20.0	5.261×10^{-4}	0.750	1.200	2.27	2.87	3.80	0.88	0.02	0.28	0.26	0.36	0.00
20.0	6.070×10^{-4}	0.650	1.177	1.97	2.39	3.15	0.22	0.36	0.23	0.20	0.18	0.00
20.0	8.052×10^{-4}	0.490	1.166	1.06	1.85	2.45	0.93	0.69	0.13	0.14	0.00	0.25
20.0	1.273×10^{-3}	0.310	1.089	1.00	1.84	2.31	0.72	0.65	0.00	0.00	0.00	0.01
20.0	1.973×10^{-3}	0.200	0.987	1.02	1.85	2.25	0.56	0.56	0.00	0.00	0.00	0.03
20.0	3.288×10^{-3}	0.120	0.875	1.14	1.87	2.49	0.88	0.78	0.00	0.00	0.00	0.00
25.0	6.165×10^{-4}	0.800	1.207	2.42	2.94	3.96	0.23	0.92	0.33	0.23	0.36	0.00
25.0	7.587×10^{-4}	0.650	1.237	2.00	2.43	3.24	-0.17	0.70	0.19	0.15	0.11	0.00
25.0	1.007×10^{-3}	0.490	1.190	1.10	1.86	2.42	0.84	0.61	0.19	0.18	0.00	0.26
25.0	1.591×10^{-3}	0.310	1.079	1.12	1.87	2.39	0.74	0.63	0.00	0.01	0.00	0.00
25.0	2.466×10^{-3}	0.200	0.989	1.15	1.88	2.47	0.64	0.91	0.00	0.00	0.00	0.02
25.0	4.110×10^{-3}	0.120	0.854	1.30	1.91	2.60	0.75	0.92	0.00	0.00	0.00	0.00
35.0	9.206×10^{-4}	0.750	1.106	3.84	3.32	5.32	1.47	-0.25	0.46	0.28	0.19	0.00
35.0	1.062×10^{-3}	0.650	1.225	2.23	2.50	3.57	0.93	0.77	0.19	0.13	0.07	0.00
35.0	1.409×10^{-3}	0.490	1.195	1.14	1.87	2.37	0.60	0.59	0.20	0.16	0.00	0.20
35.0	2.227×10^{-3}	0.310	1.085	1.16	1.88	2.31	0.13	0.67	0.00	0.01	0.00	0.02
35.0	3.452×10^{-3}	0.200	0.984	1.27	1.91	2.45	-0.05	0.85	0.00	0.00	0.00	0.00
35.0	5.754×10^{-3}	0.120	0.847	1.46	1.96	2.94	1.29	1.00	0.00	0.00	0.00	0.00
45.0	1.366×10^{-3}	0.650	1.258	3.13	2.84	4.27	-0.15	0.56	0.19	0.13	0.06	0.00
45.0	1.812×10^{-3}	0.490	1.186	1.29	1.91	2.50	0.86	0.38	0.16	0.16	0.00	0.05
45.0	2.864×10^{-3}	0.310	1.081	1.22	1.89	2.30	0.23	0.40	0.00	0.01	0.00	0.00
45.0	4.439×10^{-3}	0.200	0.951	1.29	1.91	2.47	0.69	0.52	0.00	0.00	0.00	0.00
45.0	7.398×10^{-3}	0.120	0.806	1.52	1.97	2.84	1.28	0.48	0.00	0.00	0.00	0.00
60.0	2.416×10^{-3}	0.490	1.201	1.63	2.01	2.77	0.91	0.24	0.20	0.14	0.00	0.08
60.0	3.818×10^{-3}	0.310	1.038	1.40	1.94	2.45	-0.01	0.55	0.00	0.00	0.00	0.00
60.0	5.918×10^{-3}	0.200	0.929	1.44	1.96	2.51	0.06	0.63	0.00	0.00	0.00	0.00
60.0	9.864×10^{-3}	0.120	0.795	1.63	2.02	2.85	1.00	0.63	0.00	0.00	0.00	0.00
90.0	3.623×10^{-3}	0.490	1.097	3.36	2.72	4.47	1.03	0.40	0.20	0.13	0.00	0.00
90.0	5.727×10^{-3}	0.310	0.975	1.76	2.05	2.73	0.23	0.33	0.01	0.01	0.00	0.00
90.0	8.877×10^{-3}	0.200	0.835	1.71	2.03	2.79	0.73	0.44	0.00	0.00	0.00	0.00
90.0	1.480×10^{-2}	0.120	0.717	1.90	2.10	2.96	0.68	0.54	0.00	0.00	0.00	0.00

Table 13: Continuation of table 12

Q^2 GeV ²	x	y	σ_r	δ_{stat} %	δ_{unc} %	δ_{tot} %	$\gamma_{E'_e}$ %	γ_{θ_e} %	γ_{had} %	γ_{noise} %	γ_{asym} %	γ_{acctag} %
1.5	2.790×10^{-5}	0.848	0.662	9.36	4.94	11.36	2.78	-1.16	0.36	0.53	2.73	0.00
2.0	3.720×10^{-5}	0.848	0.760	6.37	4.34	8.32	1.81	-0.49	0.56	0.60	2.38	0.00
2.0	4.150×10^{-5}	0.760	0.663	7.43	3.97	8.82	0.86	-2.16	0.26	0.29	1.10	0.00
2.5	4.650×10^{-5}	0.848	0.829	5.43	4.12	7.51	2.26	0.15	0.34	0.40	2.15	0.00
2.5	5.190×10^{-5}	0.760	0.837	3.85	3.10	5.20	1.19	0.59	0.38	0.46	0.69	0.00
2.5	5.800×10^{-5}	0.680	0.768	4.98	3.14	5.92	0.44	0.15	0.15	0.10	0.36	0.00
3.5	6.510×10^{-5}	0.848	0.871	5.56	4.05	7.61	2.33	-0.19	0.50	0.55	2.13	0.00
3.5	7.270×10^{-5}	0.760	0.873	3.51	2.92	4.96	1.74	0.00	0.30	0.33	0.69	0.00
3.5	8.120×10^{-5}	0.680	0.869	3.15	2.49	4.54	1.83	-0.89	0.27	0.26	0.36	0.00
3.5	9.210×10^{-5}	0.600	0.939	3.36	2.66	4.34	0.30	-0.47	0.30	0.26	0.12	0.00
3.5	1.062×10^{-4}	0.520	0.957	5.39	3.27	6.67	1.22	-1.56	0.07	0.19	0.00	0.87
5.0	9.310×10^{-5}	0.848	0.849	6.48	3.99	8.24	1.58	0.08	0.46	0.55	2.65	0.00
5.0	1.038×10^{-4}	0.760	0.883	3.52	2.84	4.68	0.83	0.05	0.32	0.39	0.68	0.00
5.0	1.160×10^{-4}	0.680	1.006	2.66	2.37	3.77	1.17	-0.08	0.19	0.23	0.28	0.00
5.0	1.315×10^{-4}	0.600	0.946	2.60	2.37	3.78	1.35	-0.08	0.20	0.20	0.14	0.00
5.0	1.517×10^{-4}	0.520	1.011	2.43	2.04	3.34	0.86	-0.34	0.18	0.25	0.00	0.37
5.0	2.013×10^{-4}	0.392	0.940	2.58	2.06	3.50	0.76	-0.82	0.17	0.23	0.00	0.00
6.5	1.210×10^{-4}	0.848	0.903	7.18	4.03	8.91	0.65	0.62	0.35	0.40	3.25	0.00
6.5	1.350×10^{-4}	0.760	0.992	3.48	2.85	4.72	0.98	0.67	0.29	0.37	0.56	0.00
6.5	1.509×10^{-4}	0.680	1.069	2.56	2.35	3.70	1.04	0.57	0.31	0.35	0.21	0.00
6.5	1.710×10^{-4}	0.600	1.048	2.30	2.32	3.40	0.75	-0.46	0.19	0.19	0.11	0.00
6.5	1.973×10^{-4}	0.520	1.106	2.05	1.96	2.97	0.81	0.12	0.19	0.19	0.00	0.26
6.5	2.617×10^{-4}	0.392	1.001	1.38	1.83	2.50	0.95	-0.17	0.10	0.12	0.00	0.20
8.5	1.582×10^{-4}	0.848	0.976	7.10	4.00	9.20	2.37	0.47	0.32	0.34	3.49	0.00
8.5	1.765×10^{-4}	0.760	1.072	3.81	2.90	4.92	-0.12	0.87	0.29	0.28	0.62	0.00
8.5	1.973×10^{-4}	0.680	1.092	2.80	2.39	3.93	1.27	0.37	0.26	0.26	0.19	0.00
8.5	2.236×10^{-4}	0.600	1.103	2.32	2.33	3.41	0.60	0.65	0.19	0.18	0.09	0.00
8.5	2.580×10^{-4}	0.520	1.033	2.03	1.93	3.14	1.08	0.33	0.19	0.22	0.00	0.81
8.5	3.422×10^{-4}	0.392	1.087	1.20	1.81	2.29	0.71	-0.01	0.09	0.11	0.00	0.02
8.5	5.409×10^{-4}	0.248	1.015	1.32	1.83	2.35	0.57	0.35	0.00	0.00	0.00	0.00
8.5	8.384×10^{-4}	0.160	0.941	1.47	1.85	2.56	0.92	-0.33	0.00	0.00	0.00	0.00
8.5	1.397×10^{-3}	0.096	0.818	2.58	2.07	3.50	1.11	-0.16	0.00	0.00	0.00	0.10
12.0	2.233×10^{-4}	0.848	1.238	5.51	4.00	7.51	2.15	0.15	0.47	0.34	2.24	0.00
12.0	2.492×10^{-4}	0.760	1.083	4.06	2.91	5.19	1.15	0.15	0.25	0.24	0.76	0.00
12.0	2.785×10^{-4}	0.680	1.167	3.07	2.43	4.09	0.29	1.07	0.26	0.28	0.24	0.00
12.0	3.156×10^{-4}	0.600	1.188	2.55	2.37	3.70	0.76	0.97	0.22	0.19	0.11	0.00
12.0	3.642×10^{-4}	0.520	1.175	2.12	1.96	3.03	0.43	0.64	0.21	0.20	0.00	0.40
12.0	4.831×10^{-4}	0.392	1.127	1.19	1.81	2.33	0.71	0.50	0.06	0.08	0.00	0.04
12.0	7.636×10^{-4}	0.248	1.053	1.23	1.82	2.31	0.64	0.31	0.00	0.00	0.00	0.05
12.0	1.184×10^{-3}	0.160	1.017	1.29	1.83	2.39	0.77	0.30	0.00	0.00	0.00	0.00
12.0	1.973×10^{-3}	0.096	0.871	2.25	2.00	3.36	1.48	-0.04	0.00	0.00	0.00	0.00
15.0	2.792×10^{-4}	0.848	1.110	6.31	4.04	7.92	1.47	0.34	0.37	0.36	2.01	0.00
15.0	3.115×10^{-4}	0.760	1.294	3.40	2.90	4.56	0.47	0.38	0.33	0.31	0.48	0.00
15.0	3.481×10^{-4}	0.680	1.226	3.18	2.47	4.05	0.24	0.28	0.16	0.17	0.24	0.00
15.0	3.945×10^{-4}	0.600	1.156	2.97	2.43	3.96	0.39	0.81	0.25	0.21	0.15	0.00
15.0	4.552×10^{-4}	0.520	1.255	2.33	2.01	3.23	0.69	0.60	0.20	0.18	0.00	0.26
15.0	6.039×10^{-4}	0.392	1.162	1.29	1.82	2.53	0.95	0.72	0.08	0.11	0.00	0.03
15.0	9.545×10^{-4}	0.248	1.044	1.28	1.82	2.30	0.37	0.43	0.00	0.00	0.00	0.00
15.0	1.479×10^{-3}	0.160	0.973	1.32	1.83	2.58	0.99	0.78	0.00	0.00	0.00	0.00
15.0	2.466×10^{-3}	0.096	0.856	2.17	1.98	3.36	1.31	0.94	0.00	0.00	0.00	0.07

Table 14: Reduced cross section σ_r , as measured with the $E_p = 575$ GeV data sample. Description of the columns is given in the caption of table 12.

Q^2 GeV ²	x	y	σ_r	δ_{stat} %	δ_{unc} %	δ_{tot} %	$\gamma_{E'_e}$ %	γ_{θ_e} %	γ_{had} %	γ_{noise} %	γ_{asym} %	γ_{acctag} %
20.0	3.722×10^{-4}	0.848	1.287	6.59	4.25	8.28	2.28	-0.09	0.32	0.35	1.27	0.00
20.0	4.153×10^{-4}	0.760	1.246	3.65	2.93	4.80	0.89	0.17	0.28	0.24	0.42	0.00
20.0	4.642×10^{-4}	0.680	1.293	3.04	2.46	3.95	0.20	0.47	0.19	0.17	0.18	0.00
20.0	5.261×10^{-4}	0.600	1.135	3.17	2.46	4.16	0.73	0.67	0.27	0.24	0.17	0.00
20.0	6.070×10^{-4}	0.520	1.224	2.57	2.06	3.64	0.65	1.27	0.21	0.19	0.00	0.52
20.0	8.052×10^{-4}	0.392	1.212	1.41	1.84	2.50	0.44	0.80	0.10	0.10	0.00	0.03
20.0	1.273×10^{-3}	0.248	1.093	1.39	1.84	2.53	0.53	0.89	0.00	0.00	0.00	0.00
20.0	1.973×10^{-3}	0.160	0.981	1.44	1.85	2.63	0.87	0.84	0.00	0.00	0.00	0.00
20.0	3.288×10^{-3}	0.096	0.853	2.39	2.03	3.41	1.28	0.43	0.00	0.00	0.00	0.00
25.0	4.932×10^{-4}	0.800	1.264	3.94	3.02	5.02	0.44	0.12	0.30	0.27	0.47	0.00
25.0	6.165×10^{-4}	0.640	1.272	2.19	2.46	3.35	0.41	0.37	0.27	0.18	0.12	0.00
25.0	7.587×10^{-4}	0.520	1.220	2.61	2.06	3.49	0.92	0.33	0.20	0.15	0.00	0.31
25.0	1.007×10^{-3}	0.392	1.228	1.54	1.86	2.58	0.48	0.74	0.07	0.10	0.00	0.11
25.0	1.591×10^{-3}	0.248	1.131	1.55	1.87	2.51	0.39	0.52	0.00	0.00	0.00	0.04
25.0	2.466×10^{-3}	0.160	1.015	1.58	1.88	2.93	1.22	1.04	0.00	0.00	0.00	0.00
25.0	4.110×10^{-3}	0.096	0.896	2.63	2.11	3.57	0.34	1.11	0.00	0.00	0.00	0.00
35.0	7.268×10^{-4}	0.760	1.438	6.27	3.72	7.52	-1.72	-0.48	0.28	0.19	0.22	0.00
35.0	8.123×10^{-4}	0.680	1.364	3.51	2.60	4.54	1.03	0.56	0.29	0.24	0.08	0.00
35.0	9.206×10^{-4}	0.600	1.343	3.12	2.52	4.09	0.31	0.68	0.26	0.18	0.06	0.00
35.0	1.062×10^{-3}	0.520	1.314	2.73	2.11	3.62	0.86	0.65	0.16	0.15	0.00	0.11
35.0	1.409×10^{-3}	0.392	1.254	1.55	1.87	2.55	0.54	0.54	0.08	0.11	0.00	0.00
35.0	2.227×10^{-3}	0.248	1.111	1.68	1.89	2.68	0.62	0.63	0.00	0.00	0.00	0.00
35.0	3.452×10^{-3}	0.160	0.967	1.83	1.91	2.77	0.32	0.75	0.00	0.00	0.00	0.00
35.0	5.754×10^{-3}	0.096	0.851	3.01	2.20	4.23	1.90	0.60	0.00	0.00	0.00	0.00
45.0	1.044×10^{-3}	0.680	1.274	6.36	3.42	7.23	0.24	0.30	0.17	0.09	0.06	0.00
45.0	1.184×10^{-3}	0.600	1.266	3.80	2.68	4.71	0.32	0.54	0.31	0.22	0.04	0.00
45.0	1.366×10^{-3}	0.520	1.291	3.08	2.20	3.81	0.29	0.11	0.20	0.13	0.00	0.14
45.0	1.812×10^{-3}	0.392	1.193	1.70	1.89	2.64	0.40	0.56	0.09	0.10	0.00	0.04
45.0	2.864×10^{-3}	0.248	1.106	1.71	1.90	2.64	0.29	0.60	0.00	0.00	0.00	0.00
45.0	4.439×10^{-3}	0.160	0.942	1.87	1.92	2.86	0.48	0.89	0.00	0.00	0.00	0.00
45.0	7.398×10^{-3}	0.096	0.822	3.15	2.23	4.33	1.63	1.11	0.00	0.00	0.00	0.00
60.0	1.578×10^{-3}	0.600	1.286	8.41	4.22	9.57	1.69	0.28	0.00	0.07	0.04	0.00
60.0	1.821×10^{-3}	0.520	1.263	4.23	2.54	4.98	0.23	0.63	0.10	0.12	0.00	0.00
60.0	2.416×10^{-3}	0.392	1.167	1.96	1.94	2.78	0.28	0.18	0.06	0.06	0.00	0.00
60.0	3.818×10^{-3}	0.248	1.018	1.98	1.94	2.84	0.35	0.50	0.00	0.00	0.00	0.06
60.0	5.918×10^{-3}	0.160	0.992	1.97	1.96	2.93	0.75	0.53	0.00	0.00	0.00	0.00
60.0	9.864×10^{-3}	0.096	0.777	3.38	2.30	4.23	0.14	1.07	0.00	0.00	0.00	0.00
90.0	3.623×10^{-3}	0.392	1.147	2.91	2.17	3.67	-0.05	0.51	0.07	0.09	0.00	0.00
90.0	5.727×10^{-3}	0.248	0.921	2.37	2.01	3.16	0.55	0.18	0.00	0.00	0.00	0.00
90.0	8.877×10^{-3}	0.160	0.869	2.31	2.02	3.20	0.78	0.49	0.00	0.00	0.00	0.00
90.0	1.480×10^{-2}	0.096	0.755	3.84	2.47	4.63	0.68	0.34	0.00	0.00	0.00	0.00

Table 15: Continuation of table 14

Bin #	Q^2 GeV ²	x	y	σ_r^{ave}	F_2^{ave}	$\delta_{\text{ave,stat}}$ %	$\delta_{\text{ave,uncor}}$ %	$\delta_{\text{ave,cor}}$ %	$\delta_{\text{ave,tot}}$ %	\sqrt{s} GeV
1	0.2	0.398×10^{-4}	0.050	0.232	0.232	14.27	11.96	6.97	19.88	319
2	0.2	0.251×10^{-3}	0.008	0.190	0.190	13.12	6.18	3.89	15.01	319
3	0.25	0.398×10^{-4}	0.062	0.302	0.302	9.79	11.26	7.48	16.69	319
4	0.25	0.251×10^{-3}	0.010	0.191	0.191	10.00	4.70	4.78	12.03	319
5	0.25	0.158×10^{-2}	0.002	0.204	0.204	10.84	5.29	2.69	12.35	319
6	0.35	0.511×10^{-5}	0.675	0.452	0.494	21.67	12.79	2.28	25.27	319
7	0.35	0.611×10^{-5}	0.634	0.359	0.387	5.73	11.03	5.25	13.49	301
8	0.35	0.320×10^{-4}	0.108	0.416	0.416	9.06	11.10	14.08	20.09	319
9	0.35	0.130×10^{-3}	0.027	0.266	0.266	9.59	4.38	2.94	10.95	319
10	0.35	0.500×10^{-3}	0.007	0.237	0.237	8.80	4.19	2.51	10.06	319
11	0.35	0.251×10^{-2}	0.001	0.205	0.205	9.91	4.55	1.82	11.06	319
12	0.5	0.731×10^{-5}	0.675	0.453	0.495	5.40	5.74	4.97	9.32	319
13	0.5	0.860×10^{-5}	0.650	0.444	0.481	3.74	9.17	4.01	10.68	301
14	0.5	0.158×10^{-4}	0.312	0.463	0.470	18.93	9.84	3.07	21.56	319
15	0.5	0.398×10^{-4}	0.124	0.484	0.485	10.08	6.07	10.88	16.03	319
16	0.5	0.100×10^{-3}	0.049	0.412	0.412	8.83	4.87	3.09	10.55	319
17	0.5	0.251×10^{-3}	0.020	0.297	0.297	8.33	4.25	2.61	9.71	319
18	0.5	0.800×10^{-3}	0.006	0.281	0.281	5.88	3.49	1.69	7.04	319
19	0.5	0.320×10^{-2}	0.002	0.183	0.183	11.37	6.39	1.37	13.11	319
20	0.65	0.950×10^{-5}	0.675	0.482	0.527	3.95	2.90	3.02	5.76	319
21	0.65	0.112×10^{-4}	0.650	0.506	0.549	3.73	8.21	4.04	9.88	301
22	0.65	0.158×10^{-4}	0.406	0.468	0.480	3.08	5.44	1.70	6.48	319
23	0.65	0.164×10^{-4}	0.439	0.512	0.528	3.01	7.28	2.66	8.31	301
24	0.65	0.398×10^{-4}	0.161	0.681	0.683	17.43	11.16	4.24	21.13	319
25	0.65	0.100×10^{-3}	0.064	0.501	0.501	5.14	5.84	7.32	10.68	319
26	0.65	0.251×10^{-3}	0.026	0.378	0.378	6.78	3.48	2.25	7.94	319
27	0.65	0.800×10^{-3}	0.008	0.309	0.309	4.91	3.06	2.09	6.15	319
28	0.65	0.320×10^{-2}	0.002	0.226	0.226	5.79	3.19	1.35	6.75	319
29	0.85	0.124×10^{-4}	0.675	0.569	0.621	2.54	2.52	2.56	4.40	319
30	0.85	0.138×10^{-4}	0.675	0.617	0.675	5.19	9.45	5.62	12.16	301
31	0.85	0.200×10^{-4}	0.470	0.598	0.620	2.64	4.98	2.72	6.26	301
32	0.85	0.200×10^{-4}	0.419	0.614	0.631	1.95	5.36	1.75	5.97	319
33	0.85	0.398×10^{-4}	0.211	0.569	0.572	1.58	3.49	1.61	4.15	319
34	0.85	0.500×10^{-4}	0.168	0.548	0.550	2.91	4.52	2.54	5.95	319
35	0.85	0.100×10^{-3}	0.084	0.501	0.502	2.65	3.78	3.72	5.93	319
36	0.85	0.251×10^{-3}	0.033	0.415	0.415	5.88	2.98	3.08	7.28	319
37	0.85	0.800×10^{-3}	0.010	0.352	0.352	4.59	2.67	1.66	5.56	319
38	0.85	0.320×10^{-2}	0.003	0.308	0.308	4.54	2.83	1.14	5.47	301
39	1.2	0.176×10^{-4}	0.675	0.613	0.670	2.51	2.16	2.90	4.40	319
40	1.2	0.200×10^{-4}	0.675	0.744	0.813	3.59	8.36	4.07	9.97	301
41	1.2	0.200×10^{-4}	0.592	0.675	0.719	2.61	2.51	1.45	3.90	319
42	1.2	0.320×10^{-4}	0.415	0.708	0.727	2.67	4.55	2.44	5.81	301
43	1.2	0.320×10^{-4}	0.370	0.692	0.706	1.67	2.73	1.45	3.51	319
44	1.2	0.631×10^{-4}	0.188	0.649	0.652	1.18	2.27	1.71	3.08	319
45	1.2	0.800×10^{-4}	0.148	0.596	0.598	2.18	4.03	2.52	5.22	319
46	1.2	0.130×10^{-3}	0.091	0.544	0.545	2.42	4.97	1.64	5.76	319
47	1.2	0.158×10^{-3}	0.075	0.506	0.506	1.54	2.35	1.46	3.17	319
48	1.2	0.398×10^{-3}	0.030	0.503	0.503	2.09	3.37	1.63	4.29	319
49	1.2	0.130×10^{-2}	0.009	0.375	0.375	3.54	2.67	1.61	4.72	319
50	1.2	0.500×10^{-2}	0.002	0.298	0.298	4.50	2.61	1.64	5.46	319
51	1.5	0.185×10^{-4}	0.800	0.621	0.711	3.14	3.48	4.33	6.38	319
52	1.5	0.219×10^{-4}	0.675	0.707	0.773	1.93	1.79	1.60	3.08	319
53	1.5	0.320×10^{-4}	0.519	0.805	0.843	1.19	3.20	2.85	4.45	301
54	1.5	0.320×10^{-4}	0.462	0.759	0.786	1.73	2.15	1.24	3.02	319
55	1.5	0.500×10^{-4}	0.296	0.762	0.772	1.04	1.98	1.29	2.58	319
56	1.5	0.800×10^{-4}	0.185	0.702	0.705	1.26	2.15	1.52	2.92	319
57	1.5	0.130×10^{-3}	0.114	0.645	0.646	1.46	2.43	1.68	3.29	319
58	1.5	0.200×10^{-3}	0.074	0.617	0.618	2.07	2.86	1.78	3.95	319
59	1.5	0.320×10^{-3}	0.046	0.586	0.586	1.48	2.26	1.85	3.27	319
60	1.5	0.500×10^{-3}	0.030	0.550	0.550	2.51	7.05	1.94	7.73	319
61	1.5	0.800×10^{-3}	0.018	0.497	0.497	2.35	2.47	1.63	3.78	319
62	1.5	0.100×10^{-2}	0.015	0.465	0.465	5.21	3.74	1.50	6.58	319
63	1.5	0.320×10^{-2}	0.005	0.410	0.410	2.31	2.04	1.59	3.47	301
64	1.5	0.130×10^{-1}	0.001	0.327	0.327	3.99	2.49	5.17	6.99	319

Table 16: Combined reduced cross section σ_r for $E_p = 920$ GeV and $E_p = 820$ GeV. F_2^{ave} represents the structure function F_2 calculated from σ_r^{ave} by using $R = 0.26$. $\delta_{\text{ave,stat}}$, $\delta_{\text{ave,uncor}}$, $\delta_{\text{ave,cor}}$ and $\delta_{\text{ave,tot}}$ represent the statistical, uncorrelated systematic, correlated systematic and total experimental uncertainty, respectively. The uncertainties are quoted in percent relative to σ_r^{ave} . The overall normalisation uncertainty of 0.5% is not included.

Bin #	Q^2 GeV ²	x	y	σ_r^{ave}	F_2^{ave}	$\delta_{\text{ave,stat}}$ %	$\delta_{\text{ave,uncor}}$ %	$\delta_{\text{ave,cor}}$ %	$\delta_{\text{ave,tot}}$ %	\sqrt{s} GeV
65	2.	0.247×10^{-4}	0.800	0.788	0.903	2.30	2.70	3.33	4.86	319
66	2.	0.295×10^{-4}	0.675	0.798	0.872	1.48	1.65	1.43	2.64	319
67	2.	0.328×10^{-4}	0.675	0.843	0.922	1.40	5.32	3.10	6.32	301
68	2.	0.500×10^{-4}	0.443	0.860	0.887	0.80	2.49	1.41	2.97	301
69	2.	0.500×10^{-4}	0.395	0.828	0.848	1.52	1.94	1.05	2.67	319
70	2.	0.800×10^{-4}	0.247	0.771	0.778	0.80	1.70	1.06	2.16	319
71	2.	0.130×10^{-3}	0.152	0.729	0.731	0.98	1.73	1.13	2.29	319
72	2.	0.200×10^{-3}	0.099	0.681	0.682	0.95	1.85	1.36	2.48	319
73	2.	0.320×10^{-3}	0.062	0.635	0.636	1.00	1.65	1.52	2.46	319
74	2.	0.500×10^{-3}	0.039	0.580	0.580	1.17	2.04	1.54	2.81	319
75	2.	0.100×10^{-2}	0.020	0.511	0.511	0.98	1.79	1.23	2.39	319
76	2.	0.320×10^{-2}	0.006	0.425	0.425	1.07	1.90	1.66	2.74	319
77	2.	0.130×10^{-1}	0.002	0.361	0.361	2.38	2.13	4.27	5.33	319
78	2.5	0.309×10^{-4}	0.800	0.836	0.958	1.98	1.89	1.72	3.23	319
79	2.5	0.379×10^{-4}	0.650	0.871	0.944	2.17	2.09	1.32	3.29	319
80	2.5	0.410×10^{-4}	0.675	0.925	1.011	1.56	6.21	2.73	6.96	301
81	2.5	0.500×10^{-4}	0.553	0.899	0.949	1.19	2.09	1.95	3.10	301
82	2.5	0.500×10^{-4}	0.493	0.866	0.902	1.50	1.65	0.99	2.44	319
83	2.5	0.800×10^{-4}	0.308	0.859	0.871	0.66	1.19	0.97	1.67	319
84	2.5	0.130×10^{-3}	0.190	0.798	0.802	0.70	1.16	1.01	1.69	319
85	2.5	0.200×10^{-3}	0.123	0.760	0.761	0.76	1.61	1.03	2.06	319
86	2.5	0.320×10^{-3}	0.077	0.673	0.674	0.79	1.75	1.17	2.25	319
87	2.5	0.500×10^{-3}	0.049	0.631	0.632	0.76	1.47	1.20	2.05	319
88	2.5	0.800×10^{-3}	0.031	0.580	0.580	0.87	1.84	1.00	2.27	319
89	2.5	0.158×10^{-2}	0.016	0.536	0.536	0.68	1.63	1.12	2.09	319
90	2.5	0.500×10^{-2}	0.005	0.440	0.440	0.74	1.82	1.63	2.55	319
91	2.5	0.200×10^{-1}	0.001	0.342	0.342	2.52	2.45	7.94	8.68	319
92	3.5	0.432×10^{-4}	0.800	0.917	1.050	2.03	1.87	1.64	3.22	319
93	3.5	0.512×10^{-4}	0.675	0.928	1.015	1.77	1.72	1.15	2.72	319
94	3.5	0.574×10^{-4}	0.675	0.935	1.022	1.99	6.18	2.39	6.92	301
95	3.5	0.800×10^{-4}	0.484	0.953	0.991	1.00	1.76	1.70	2.64	301
96	3.5	0.800×10^{-4}	0.432	0.958	0.986	1.25	1.55	0.91	2.19	319
97	3.5	0.130×10^{-3}	0.266	0.921	0.930	0.65	1.06	0.91	1.54	319
98	3.5	0.200×10^{-3}	0.173	0.863	0.866	0.69	1.07	0.94	1.58	319
99	3.5	0.320×10^{-3}	0.108	0.803	0.804	0.73	1.13	0.95	1.65	319
100	3.5	0.500×10^{-3}	0.069	0.762	0.762	0.82	1.33	1.02	1.86	319
101	3.5	0.800×10^{-3}	0.043	0.663	0.664	0.67	1.17	0.97	1.65	319
102	3.5	0.130×10^{-2}	0.027	0.628	0.628	0.86	1.38	1.06	1.94	319
103	3.5	0.251×10^{-2}	0.014	0.558	0.558	0.62	1.12	1.00	1.63	319
104	3.5	0.800×10^{-2}	0.004	0.449	0.449	0.68	1.56	1.51	2.28	319
105	5.	0.618×10^{-4}	0.800	1.000	1.146	1.99	1.85	1.60	3.15	319
106	5.	0.732×10^{-4}	0.675	1.082	1.183	1.16	1.59	1.03	2.22	319
107	5.	0.819×10^{-4}	0.675	1.052	1.149	2.07	4.85	2.96	6.05	301
108	5.	0.130×10^{-3}	0.426	1.057	1.088	1.02	1.68	1.07	2.24	301
109	5.	0.130×10^{-3}	0.379	1.066	1.089	1.33	1.67	0.94	2.33	319
110	5.	0.200×10^{-3}	0.247	1.015	1.023	0.73	1.20	0.95	1.69	319
111	5.	0.320×10^{-3}	0.154	0.934	0.937	0.79	1.29	0.89	1.75	319
112	5.	0.500×10^{-3}	0.099	0.842	0.843	0.80	1.29	0.91	1.77	319
113	5.	0.800×10^{-3}	0.062	0.755	0.756	0.82	1.29	0.93	1.79	319
114	5.	0.130×10^{-2}	0.038	0.698	0.698	0.85	1.31	1.05	1.88	319
115	5.	0.200×10^{-2}	0.025	0.642	0.642	0.88	1.31	0.95	1.84	319
116	5.	0.398×10^{-2}	0.012	0.571	0.571	0.67	1.23	1.06	1.75	319
117	5.	0.130×10^{-1}	0.004	0.439	0.439	0.71	1.86	1.62	2.56	319
118	6.5	0.803×10^{-4}	0.800	1.092	1.251	1.98	1.80	1.39	3.02	319
119	6.5	0.951×10^{-4}	0.675	1.110	1.213	1.72	1.65	1.16	2.66	319
120	6.5	0.130×10^{-3}	0.553	1.129	1.192	1.53	1.73	1.91	2.99	301
121	6.5	0.130×10^{-3}	0.493	1.125	1.172	1.12	1.43	0.99	2.07	319
122	6.5	0.200×10^{-3}	0.360	1.122	1.143	1.09	1.62	1.02	2.20	301
123	6.5	0.200×10^{-3}	0.321	1.109	1.125	1.05	1.46	0.99	2.05	319
124	6.5	0.320×10^{-3}	0.200	1.016	1.021	0.81	1.08	0.87	1.61	319
125	6.5	0.500×10^{-3}	0.128	0.939	0.941	0.84	1.28	0.94	1.79	319
126	6.5	0.800×10^{-3}	0.080	0.858	0.859	0.86	1.28	1.00	1.83	319
127	6.5	0.130×10^{-2}	0.049	0.760	0.760	0.89	1.28	0.94	1.82	319
128	6.5	0.200×10^{-2}	0.032	0.696	0.696	0.91	1.30	0.95	1.84	319
129	6.5	0.398×10^{-2}	0.016	0.618	0.618	0.67	1.21	1.02	1.71	319
130	6.5	0.130×10^{-1}	0.005	0.483	0.483	0.68	1.82	1.40	2.39	319

Table 17: Continuation of table 16

Bin #	Q^2 GeV ²	x	y	σ_r^{ave}	F_2^{ave}	$\delta_{ave,stat}$ %	$\delta_{ave,uncor}$ %	$\delta_{ave,cor}$ %	$\delta_{ave,tot}$ %	\sqrt{s} GeV
131	8.5	0.986×10^{-4}	0.850	1.158	1.355	2.32	2.99	0.96	3.90	319
132	8.5	0.105×10^{-3}	0.800	1.143	1.310	2.47	2.00	1.27	3.42	319
133	8.5	0.124×10^{-3}	0.675	1.214	1.326	1.36	1.60	1.07	2.36	319
134	8.5	0.139×10^{-3}	0.675	1.140	1.246	2.06	1.82	3.58	4.51	301
135	8.5	0.200×10^{-3}	0.470	1.186	1.230	1.38	1.64	1.40	2.56	301
136	8.5	0.200×10^{-3}	0.419	1.203	1.237	0.96	1.40	0.99	1.96	319
137	8.5	0.320×10^{-3}	0.262	1.120	1.130	0.75	1.04	0.89	1.56	319
138	8.5	0.500×10^{-3}	0.168	1.037	1.041	0.91	1.21	0.90	1.76	319
139	8.5	0.800×10^{-3}	0.105	0.954	0.955	0.93	1.30	0.91	1.84	319
140	8.5	0.130×10^{-2}	0.064	0.844	0.844	0.97	1.31	0.96	1.89	319
141	8.5	0.200×10^{-2}	0.042	0.775	0.775	0.98	1.32	0.93	1.89	319
142	8.5	0.320×10^{-2}	0.026	0.665	0.665	1.03	1.33	0.98	1.94	319
143	8.5	0.631×10^{-2}	0.013	0.606	0.606	0.76	1.25	0.99	1.77	319
144	8.5	0.200×10^{-1}	0.004	0.457	0.457	0.83	1.85	1.70	2.64	319
145	12.	0.139×10^{-3}	0.850	1.278	1.497	1.78	2.91	0.95	3.55	319
146	12.	0.158×10^{-3}	0.750	1.360	1.526	1.63	2.02	0.90	2.75	319
147	12.	0.161×10^{-3}	0.825	1.229	1.423	4.12	3.78	1.13	5.70	301
148	12.	0.200×10^{-3}	0.675	1.271	1.389	0.88	2.15	2.53	3.44	301
149	12.	0.200×10^{-3}	0.592	1.281	1.365	0.95	0.71	1.50	1.92	319
150	12.	0.320×10^{-3}	0.415	1.228	1.261	0.57	1.73	1.10	2.13	301
151	12.	0.320×10^{-3}	0.370	1.228	1.253	0.86	0.68	0.89	1.42	319
152	12.	0.500×10^{-3}	0.237	1.158	1.166	0.54	0.76	0.88	1.28	319
153	12.	0.800×10^{-3}	0.148	1.058	1.061	0.72	0.63	0.78	1.23	319
154	12.	0.130×10^{-2}	0.091	0.925	0.926	1.08	1.32	0.91	1.93	319
155	12.	0.200×10^{-2}	0.059	0.863	0.864	1.09	1.35	0.90	1.96	319
156	12.	0.320×10^{-2}	0.037	0.759	0.759	1.12	1.36	0.90	1.98	319
157	12.	0.631×10^{-2}	0.019	0.648	0.648	0.85	1.26	0.98	1.81	319
158	12.	0.200×10^{-1}	0.006	0.491	0.491	0.90	1.85	1.39	2.48	319
159	15.	0.174×10^{-3}	0.850	1.335	1.563	1.38	3.71	1.07	4.10	319
160	15.	0.197×10^{-3}	0.750	1.387	1.557	0.93	2.64	1.06	3.00	319
161	15.	0.201×10^{-3}	0.825	1.262	1.461	3.20	3.61	1.13	4.96	301
162	15.	0.228×10^{-3}	0.650	1.329	1.440	1.81	2.33	1.07	3.14	319
163	15.	0.247×10^{-3}	0.675	1.361	1.488	0.92	2.17	1.67	2.89	301
164	15.	0.320×10^{-3}	0.519	1.300	1.362	0.68	1.97	1.28	2.45	301
165	15.	0.320×10^{-3}	0.462	1.312	1.358	0.85	0.70	1.16	1.60	319
166	15.	0.500×10^{-3}	0.296	1.219	1.233	0.45	0.74	0.86	1.22	319
167	15.	0.800×10^{-3}	0.185	1.113	1.118	0.46	0.70	0.88	1.22	319
168	15.	0.130×10^{-2}	0.114	0.987	0.988	0.49	0.74	0.96	1.31	319
169	15.	0.200×10^{-2}	0.074	0.879	0.880	0.51	0.75	1.07	1.40	319
170	15.	0.320×10^{-2}	0.046	0.794	0.794	0.56	0.78	0.98	1.37	319
171	15.	0.500×10^{-2}	0.030	0.725	0.725	0.59	0.79	0.99	1.40	319
172	15.	0.100×10^{-1}	0.015	0.607	0.607	0.50	0.72	0.94	1.29	319
173	15.	0.251×10^{-1}	0.006	0.503	0.503	0.67	1.77	1.71	2.56	319
174	20.	0.232×10^{-3}	0.850	1.382	1.618	1.53	3.73	1.05	4.16	319
175	20.	0.263×10^{-3}	0.750	1.425	1.600	0.83	2.63	1.07	2.96	319
176	20.	0.268×10^{-3}	0.825	1.327	1.536	3.25	3.67	1.12	5.03	301
177	20.	0.304×10^{-3}	0.650	1.377	1.493	0.76	2.16	1.03	2.51	319
178	20.	0.329×10^{-3}	0.675	1.401	1.531	1.04	2.10	1.41	2.74	301
179	20.	0.500×10^{-3}	0.443	1.315	1.357	0.64	1.71	1.01	2.09	301
180	20.	0.500×10^{-3}	0.395	1.309	1.341	0.74	0.70	0.88	1.34	319
181	20.	0.800×10^{-3}	0.247	1.203	1.213	0.44	0.68	0.86	1.18	319
182	20.	0.130×10^{-2}	0.152	1.081	1.084	0.46	0.68	0.89	1.21	319
183	20.	0.200×10^{-2}	0.099	0.974	0.976	0.49	0.70	0.98	1.30	319
184	20.	0.320×10^{-2}	0.062	0.860	0.860	0.52	0.71	0.95	1.29	319
185	20.	0.500×10^{-2}	0.039	0.771	0.771	0.55	0.73	0.93	1.30	319
186	20.	0.100×10^{-1}	0.020	0.650	0.650	0.45	0.66	0.99	1.27	319
187	20.	0.251×10^{-1}	0.008	0.522	0.522	0.55	1.76	1.38	2.30	319
188	25.	0.290×10^{-3}	0.850	1.466	1.716	2.47	3.86	1.06	4.71	319
189	25.	0.329×10^{-3}	0.750	1.436	1.612	0.88	2.64	1.04	2.97	319
190	25.	0.335×10^{-3}	0.825	1.399	1.620	4.10	3.92	1.11	5.78	301
191	25.	0.379×10^{-3}	0.650	1.455	1.577	0.73	2.16	1.04	2.51	319
192	25.	0.411×10^{-3}	0.675	1.401	1.531	1.16	2.10	1.34	2.75	301
193	25.	0.500×10^{-3}	0.553	1.370	1.446	1.04	1.88	1.08	2.40	301
194	25.	0.500×10^{-3}	0.493	1.390	1.447	0.70	0.74	0.94	1.39	319
195	25.	0.800×10^{-3}	0.308	1.271	1.289	0.44	0.67	0.85	1.16	319
196	25.	0.130×10^{-2}	0.190	1.138	1.143	0.47	0.69	0.87	1.20	319
197	25.	0.200×10^{-2}	0.123	1.029	1.031	0.51	0.69	0.91	1.25	319
198	25.	0.320×10^{-2}	0.077	0.910	0.910	0.52	0.70	0.97	1.31	319
199	25.	0.500×10^{-2}	0.049	0.797	0.797	0.54	0.70	0.96	1.30	319
200	25.	0.800×10^{-2}	0.031	0.703	0.703	0.58	0.71	0.94	1.31	319
201	25.	0.130×10^{-1}	0.019	0.636	0.636	0.55	0.73	1.05	1.39	319
202	25.	0.200×10^{-1}	0.012	0.581	0.581	0.84	0.77	1.20	1.66	319
203	25.	0.398×10^{-1}	0.006	0.498	0.498	0.62	1.78	1.82	2.62	319

Table 18: Continuation of table 16.

Bin #	Q^2 GeV ²	x	y	σ_r^{ave}	F_2^{ave}	$\delta_{ave,stat}$ %	$\delta_{ave,uncor}$ %	$\delta_{ave,cor}$ %	$\delta_{ave,tot}$ %	\sqrt{s} GeV
204	35.	0.460×10^{-3}	0.750	1.444	1.621	1.24	2.68	1.05	3.13	319
205	35.	0.531×10^{-3}	0.650	1.469	1.593	0.66	2.15	1.06	2.49	319
206	35.	0.575×10^{-3}	0.675	1.512	1.652	1.36	2.01	1.15	2.69	301
207	35.	0.800×10^{-3}	0.484	1.389	1.444	0.88	1.75	1.02	2.20	301
208	35.	0.800×10^{-3}	0.432	1.391	1.433	0.62	0.72	0.88	1.29	319
209	35.	0.130×10^{-2}	0.266	1.227	1.239	0.45	0.66	0.85	1.16	319
210	35.	0.200×10^{-2}	0.173	1.098	1.102	0.50	0.67	0.87	1.21	319
211	35.	0.320×10^{-2}	0.108	0.975	0.976	0.59	0.72	0.96	1.33	319
212	35.	0.500×10^{-2}	0.069	0.854	0.855	0.60	0.72	0.96	1.34	319
213	35.	0.800×10^{-2}	0.043	0.758	0.759	0.62	0.72	0.96	1.35	319
214	35.	0.130×10^{-1}	0.027	0.670	0.670	0.68	0.74	0.97	1.40	319
215	35.	0.200×10^{-1}	0.017	0.607	0.607	0.67	0.74	1.15	1.53	319
216	35.	0.398×10^{-1}	0.009	0.511	0.511	0.76	2.14	1.37	2.66	319
217	35.	0.800×10^{-1}	0.004	0.451	0.451	1.78	3.54	2.85	4.88	319
218	45.	0.634×10^{-3}	0.700	1.455	1.603	1.01	2.21	1.05	2.64	319
219	45.	0.800×10^{-3}	0.555	1.466	1.548	0.94	0.94	0.89	1.60	319
220	45.	0.130×10^{-2}	0.383	1.326	1.356	0.92	1.75	0.92	2.18	301
221	45.	0.130×10^{-2}	0.341	1.311	1.334	0.63	0.74	0.85	1.29	319
222	45.	0.200×10^{-2}	0.222	1.163	1.171	0.49	0.69	0.85	1.20	319
223	45.	0.320×10^{-2}	0.139	1.016	1.018	0.65	0.73	0.89	1.32	319
224	45.	0.500×10^{-2}	0.089	0.898	0.899	0.69	0.73	0.96	1.39	319
225	45.	0.800×10^{-2}	0.055	0.787	0.787	0.71	0.75	0.93	1.39	319
226	45.	0.130×10^{-1}	0.034	0.691	0.691	0.75	0.75	0.94	1.42	319
227	45.	0.200×10^{-1}	0.022	0.611	0.611	0.75	0.77	1.16	1.58	319
228	45.	0.320×10^{-1}	0.014	0.540	0.540	1.09	0.85	1.03	1.72	319
229	45.	0.631×10^{-1}	0.007	0.457	0.457	0.92	1.82	2.10	2.93	319
230	60.	0.130×10^{-2}	0.455	1.398	1.446	0.80	0.90	0.87	1.48	319
231	60.	0.200×10^{-2}	0.296	1.252	1.267	0.54	0.74	0.85	1.25	319
232	60.	0.320×10^{-2}	0.185	1.087	1.092	0.58	0.71	0.86	1.26	319
233	60.	0.500×10^{-2}	0.118	0.964	0.965	0.79	0.78	0.93	1.45	319
234	60.	0.800×10^{-2}	0.074	0.829	0.829	0.82	0.79	0.95	1.48	319
235	60.	0.130×10^{-1}	0.046	0.716	0.716	0.86	0.80	0.98	1.53	319
236	60.	0.200×10^{-1}	0.030	0.648	0.648	0.94	0.82	1.06	1.63	319
237	60.	0.320×10^{-1}	0.018	0.563	0.563	1.00	0.83	1.10	1.70	319
238	60.	0.631×10^{-1}	0.009	0.465	0.465	1.14	2.18	2.02	3.18	319
239	60.	0.130	0.005	0.399	0.399	2.93	3.88	2.45	5.45	301
240	90.	0.200×10^{-2}	0.444	1.324	1.367	0.94	1.06	0.88	1.67	319
241	90.	0.320×10^{-2}	0.277	1.169	1.181	0.64	0.82	0.86	1.35	319
242	90.	0.500×10^{-2}	0.178	1.027	1.031	0.75	0.76	0.87	1.38	319
243	90.	0.800×10^{-2}	0.111	0.880	0.881	0.96	0.84	0.98	1.61	319
244	90.	0.130×10^{-1}	0.068	0.758	0.759	0.99	0.85	1.00	1.65	319
245	90.	0.200×10^{-1}	0.044	0.664	0.664	1.06	0.87	1.07	1.74	319
246	90.	0.320×10^{-1}	0.028	0.569	0.569	1.11	0.88	1.10	1.79	319
247	90.	0.500×10^{-1}	0.018	0.492	0.492	1.59	1.02	1.41	2.35	319
248	90.	0.100	0.009	0.402	0.402	1.50	1.65	2.10	3.06	319
249	120.	0.500×10^{-2}	0.237	1.032	1.040	1.58	1.15	0.96	2.18	319
250	120.	0.800×10^{-2}	0.148	0.897	0.899	1.31	1.02	0.95	1.91	319
251	120.	0.130×10^{-1}	0.091	0.787	0.788	1.32	1.02	1.08	1.99	319
252	120.	0.200×10^{-1}	0.059	0.662	0.662	1.34	1.01	1.11	2.01	319
253	120.	0.320×10^{-1}	0.037	0.580	0.580	1.47	1.03	1.21	2.16	319
254	120.	0.500×10^{-1}	0.024	0.498	0.498	1.55	1.05	1.30	2.28	319
255	120.	0.100	0.012	0.404	0.404	1.91	1.12	2.68	3.48	319
256	120.	0.200	0.006	0.342	0.342	4.61	4.81	2.94	7.29	319
257	150.	0.130×10^{-1}	0.114	0.748	0.749	5.47	2.73	1.22	6.24	319
258	150.	0.200×10^{-1}	0.074	0.722	0.722	3.16	2.19	1.46	4.12	319
259	150.	0.320×10^{-1}	0.046	0.605	0.605	2.99	1.92	2.17	4.17	319
260	150.	0.500×10^{-1}	0.030	0.503	0.503	3.02	1.87	1.83	3.99	319
261	150.	0.100	0.015	0.429	0.429	3.43	1.80	2.60	4.67	319
262	150.	0.200	0.007	0.330	0.330	8.06	7.13	1.99	10.94	319

Table 19: Continuation of table 16.

Bin #	Q^2 GeV ²	x	y	σ_r^{ave}	F_2^{ave}	$\delta_{ave,stat}$ %	$\delta_{ave,uncor}$ %	$\delta_{ave,cor}$ %	$\delta_{ave,tot}$ %	\sqrt{s} GeV
1	1.5	0.279×10^{-4}	0.848	0.661	0.773	9.37	4.94	4.80	11.63	252
2	1.5	0.348×10^{-4}	0.850	0.521	0.610	8.09	4.96	4.60	10.54	225
3	2.	0.372×10^{-4}	0.848	0.758	0.887	6.38	4.34	4.14	8.76	252
4	2.	0.415×10^{-4}	0.761	0.663	0.747	7.43	3.97	3.73	9.21	252
5	2.	0.464×10^{-4}	0.850	0.707	0.828	4.56	4.31	3.97	7.42	225
6	2.	0.526×10^{-4}	0.750	0.720	0.808	4.58	3.93	3.43	6.94	225
7	2.5	0.465×10^{-4}	0.848	0.826	0.966	5.44	4.12	4.13	7.98	252
8	2.5	0.519×10^{-4}	0.760	0.834	0.940	3.86	3.10	3.21	5.90	252
9	2.5	0.580×10^{-4}	0.850	0.780	0.913	4.17	4.16	4.24	7.26	225
10	2.5	0.580×10^{-4}	0.680	0.765	0.838	4.99	3.14	2.90	6.57	252
11	2.5	0.658×10^{-4}	0.750	0.770	0.864	2.64	3.03	3.15	5.11	225
12	2.5	0.759×10^{-4}	0.650	0.714	0.774	4.31	3.45	3.30	6.43	225
13	3.5	0.651×10^{-4}	0.848	0.868	1.016	5.57	4.05	4.18	8.05	252
14	3.5	0.727×10^{-4}	0.760	0.870	0.981	3.52	2.92	3.34	5.66	252
15	3.5	0.812×10^{-4}	0.850	0.796	0.932	4.20	4.05	3.87	7.01	225
16	3.5	0.812×10^{-4}	0.680	0.867	0.949	3.15	2.49	3.40	5.26	252
17	3.5	0.921×10^{-4}	0.750	0.822	0.923	2.22	2.86	3.38	4.95	225
18	3.5	0.921×10^{-4}	0.600	0.936	1.000	3.36	2.66	2.92	5.19	252
19	3.5	0.106×10^{-3}	0.650	0.860	0.932	2.03	2.47	3.33	4.61	225
20	3.5	0.106×10^{-3}	0.520	0.956	1.001	5.39	3.27	3.46	7.20	252
21	3.5	0.141×10^{-3}	0.490	0.800	0.833	2.54	2.45	3.65	5.08	225
22	5.	0.931×10^{-4}	0.848	0.846	0.990	6.49	3.99	4.19	8.70	252
23	5.	0.104×10^{-3}	0.760	0.880	0.992	3.53	2.84	3.05	5.46	252
24	5.	0.116×10^{-3}	0.850	0.942	1.103	4.18	4.01	4.20	7.16	225
25	5.	0.116×10^{-3}	0.680	1.002	1.098	2.66	2.37	3.05	4.69	252
26	5.	0.131×10^{-3}	0.750	0.927	1.040	2.07	2.80	3.24	4.76	225
27	5.	0.131×10^{-3}	0.600	0.943	1.008	2.60	2.37	3.10	4.69	252
28	5.	0.152×10^{-3}	0.650	0.970	1.051	1.69	2.33	3.05	4.19	225
29	5.	0.152×10^{-3}	0.520	1.009	1.056	2.43	2.04	2.99	4.36	252
30	5.	0.201×10^{-3}	0.490	0.917	0.955	1.16	1.87	3.05	3.76	225
31	5.	0.201×10^{-3}	0.392	0.938	0.960	2.58	2.06	3.02	4.48	252
32	6.5	0.121×10^{-3}	0.848	0.900	1.052	7.19	4.03	4.42	9.36	252
33	6.5	0.135×10^{-3}	0.760	0.988	1.114	3.49	2.85	3.12	5.48	252
34	6.5	0.151×10^{-3}	0.850	1.037	1.214	4.26	4.02	4.09	7.14	225
35	6.5	0.151×10^{-3}	0.680	1.065	1.166	2.56	2.35	3.08	4.64	252
36	6.5	0.171×10^{-3}	0.750	0.960	1.078	2.15	2.80	3.16	4.74	225
37	6.5	0.171×10^{-3}	0.600	1.045	1.117	2.30	2.32	2.96	4.41	252
38	6.5	0.197×10^{-3}	0.650	1.010	1.095	1.60	2.30	2.97	4.08	225
39	6.5	0.197×10^{-3}	0.520	1.102	1.154	2.05	1.96	2.95	4.10	252
40	6.5	0.262×10^{-3}	0.490	1.011	1.052	0.90	1.82	3.01	3.63	225
41	6.5	0.262×10^{-3}	0.392	0.998	1.022	1.38	1.83	2.97	3.76	252
42	6.5	0.414×10^{-3}	0.248	0.973	0.981	1.13	1.86	3.00	3.70	252
43	8.5	0.158×10^{-3}	0.848	0.972	1.137	7.11	4.00	5.02	9.58	252
44	8.5	0.177×10^{-3}	0.760	1.067	1.203	3.82	2.90	3.04	5.68	252
45	8.5	0.197×10^{-3}	0.850	0.972	1.137	4.67	4.01	4.44	7.59	225
46	8.5	0.197×10^{-3}	0.680	1.088	1.192	2.80	2.39	3.10	4.82	252
47	8.5	0.224×10^{-3}	0.750	1.010	1.134	2.38	2.84	3.16	4.87	225
48	8.5	0.224×10^{-3}	0.600	1.099	1.174	2.32	2.33	2.96	4.43	252
49	8.5	0.258×10^{-3}	0.650	1.090	1.182	1.66	2.32	3.26	4.33	225
50	8.5	0.258×10^{-3}	0.520	1.030	1.078	2.03	1.93	3.13	4.20	252
51	8.5	0.342×10^{-3}	0.490	1.054	1.097	0.85	1.81	3.02	3.62	225
52	8.5	0.342×10^{-3}	0.392	1.083	1.109	1.20	1.81	2.91	3.63	252
53	8.5	0.541×10^{-3}	0.248	1.020	1.028	0.77	1.29	2.87	3.24	252
54	8.5	0.838×10^{-3}	0.160	0.941	0.944	0.86	1.31	2.94	3.33	252
55	8.5	0.140×10^{-2}	0.096	0.846	0.847	1.16	1.44	3.02	3.55	252
56	12.	0.223×10^{-3}	0.848	1.234	1.443	5.52	4.00	4.14	7.97	252
57	12.	0.249×10^{-3}	0.760	1.079	1.217	4.07	2.91	3.13	5.90	252
58	12.	0.278×10^{-3}	0.850	1.130	1.323	3.89	3.98	3.72	6.70	225
59	12.	0.278×10^{-3}	0.680	1.162	1.272	3.08	2.43	3.05	4.97	252
60	12.	0.316×10^{-3}	0.750	1.114	1.250	2.38	2.85	3.10	4.84	225
61	12.	0.316×10^{-3}	0.600	1.183	1.264	2.56	2.37	3.07	4.64	252
62	12.	0.364×10^{-3}	0.650	1.098	1.190	1.86	2.36	3.01	4.25	225
63	12.	0.364×10^{-3}	0.520	1.171	1.226	2.12	1.96	2.97	4.14	252
64	12.	0.483×10^{-3}	0.490	1.111	1.156	0.89	1.81	3.02	3.63	225
65	12.	0.483×10^{-3}	0.392	1.123	1.150	1.19	1.81	2.95	3.66	252
66	12.	0.764×10^{-3}	0.248	1.044	1.052	0.73	1.28	2.92	3.27	252
67	12.	0.118×10^{-2}	0.160	0.994	0.997	0.78	1.30	2.93	3.29	252
68	12.	0.197×10^{-2}	0.096	0.878	0.879	1.04	1.40	3.12	3.58	252

Table 20: Combined reduced cross section σ_r for $E_p = 460$ GeV and $E_p = 575$ GeV. Description of the columns is given in the caption of table 16.

Bin #	Q^2 GeV ²	x	y	σ_r^{ave}	F_2^{ave}	$\delta_{\text{ave,stat}}\%$	$\delta_{\text{ave,uncor}}\%$	$\delta_{\text{ave,cor}}\%$	$\delta_{\text{ave,tot}}\%$	\sqrt{s} GeV
69	15.	0.279×10^{-3}	0.848	1.106	1.294	6.32	4.04	3.77	8.39	252
70	15.	0.312×10^{-3}	0.760	1.290	1.453	3.41	2.90	2.97	5.37	252
71	15.	0.348×10^{-3}	0.850	1.222	1.430	3.89	4.06	3.36	6.55	225
72	15.	0.348×10^{-3}	0.680	1.222	1.338	3.19	2.47	2.88	4.95	252
73	15.	0.395×10^{-3}	0.750	1.112	1.249	2.33	2.84	2.97	4.72	225
74	15.	0.395×10^{-3}	0.600	1.152	1.231	2.98	2.43	2.98	4.86	252
75	15.	0.455×10^{-3}	0.650	1.141	1.237	2.05	2.40	3.15	4.46	225
76	15.	0.455×10^{-3}	0.520	1.250	1.310	2.33	2.01	2.98	4.29	252
77	15.	0.604×10^{-3}	0.490	1.165	1.212	0.96	1.83	3.02	3.66	225
78	15.	0.604×10^{-3}	0.392	1.158	1.185	1.29	1.82	3.04	3.77	252
79	15.	0.954×10^{-3}	0.248	1.050	1.059	0.76	1.29	2.90	3.26	252
80	15.	0.148×10^{-2}	0.160	0.955	0.958	0.79	1.30	3.01	3.37	252
81	15.	0.247×10^{-2}	0.096	0.859	0.860	1.02	1.39	3.18	3.62	252
82	20.	0.372×10^{-3}	0.848	1.283	1.501	6.60	4.25	3.74	8.70	252
83	20.	0.415×10^{-3}	0.760	1.242	1.400	3.66	2.93	3.00	5.57	252
84	20.	0.464×10^{-3}	0.850	1.006	1.177	5.33	4.21	3.52	7.65	225
85	20.	0.464×10^{-3}	0.680	1.288	1.410	3.05	2.46	2.89	4.87	252
86	20.	0.526×10^{-3}	0.750	1.204	1.351	2.27	2.87	3.02	4.74	225
87	20.	0.526×10^{-3}	0.600	1.131	1.208	3.18	2.46	3.00	5.02	252
88	20.	0.607×10^{-3}	0.650	1.181	1.280	1.97	2.39	2.91	4.25	225
89	20.	0.607×10^{-3}	0.520	1.219	1.277	2.58	2.06	3.18	4.58	252
90	20.	0.805×10^{-3}	0.490	1.169	1.217	1.06	1.85	3.08	3.75	225
91	20.	0.805×10^{-3}	0.392	1.207	1.236	1.41	1.84	2.96	3.76	252
92	20.	0.127×10^{-2}	0.248	1.094	1.103	0.83	1.30	2.97	3.35	252
93	20.	0.197×10^{-2}	0.160	0.985	0.988	0.85	1.31	2.97	3.36	252
94	20.	0.329×10^{-2}	0.096	0.869	0.869	1.09	1.42	3.05	3.54	252
95	25.	0.493×10^{-3}	0.800	1.260	1.443	3.95	3.02	2.93	5.77	252
96	25.	0.616×10^{-3}	0.800	1.210	1.386	2.42	2.94	3.04	4.87	225
97	25.	0.616×10^{-3}	0.640	1.268	1.370	2.19	2.46	2.90	4.39	252
98	25.	0.759×10^{-3}	0.650	1.240	1.344	2.00	2.43	2.94	4.31	225
99	25.	0.759×10^{-3}	0.520	1.216	1.273	2.61	2.06	3.00	4.48	252
100	25.	0.101×10^{-2}	0.490	1.193	1.242	1.10	1.86	3.05	3.74	225
101	25.	0.101×10^{-2}	0.392	1.223	1.252	1.54	1.86	2.95	3.82	252
102	25.	0.159×10^{-2}	0.248	1.106	1.115	0.93	1.33	2.92	3.34	252
103	25.	0.247×10^{-2}	0.160	1.001	1.004	0.95	1.34	3.08	3.49	252
104	25.	0.411×10^{-2}	0.096	0.868	0.869	1.22	1.47	3.04	3.59	252
105	35.	0.727×10^{-3}	0.760	1.434	1.617	6.28	3.72	3.33	8.02	252
106	35.	0.812×10^{-3}	0.680	1.359	1.488	3.52	2.60	3.05	5.33	252
107	35.	0.921×10^{-3}	0.750	1.110	1.246	3.83	3.32	3.22	6.01	225
108	35.	0.921×10^{-3}	0.600	1.338	1.430	3.13	2.52	2.94	4.98	252
109	35.	0.106×10^{-2}	0.650	1.228	1.331	2.23	2.50	3.09	4.56	225
110	35.	0.106×10^{-2}	0.520	1.309	1.371	2.74	2.11	3.01	4.58	252
111	35.	0.141×10^{-2}	0.490	1.198	1.247	1.14	1.87	2.99	3.71	225
112	35.	0.141×10^{-2}	0.392	1.250	1.280	1.55	1.87	2.92	3.80	252
113	35.	0.223×10^{-2}	0.248	1.100	1.109	0.98	1.34	2.90	3.34	252
114	35.	0.345×10^{-2}	0.160	0.977	0.981	1.07	1.36	2.93	3.40	252
115	35.	0.575×10^{-2}	0.096	0.849	0.850	1.36	1.52	3.26	3.85	252
116	45.	0.104×10^{-2}	0.680	1.270	1.390	6.37	3.42	2.87	7.78	252
117	45.	0.118×10^{-2}	0.600	1.262	1.348	3.81	2.68	2.92	5.50	252
118	45.	0.137×10^{-2}	0.650	1.261	1.367	3.13	2.84	2.91	5.13	225
119	45.	0.137×10^{-2}	0.520	1.287	1.348	3.08	2.20	2.87	4.75	252
120	45.	0.181×10^{-2}	0.490	1.189	1.238	1.29	1.91	3.01	3.79	225
121	45.	0.181×10^{-2}	0.392	1.189	1.217	1.70	1.89	2.91	3.87	252
122	45.	0.286×10^{-2}	0.248	1.095	1.104	1.01	1.35	2.87	3.33	252
123	45.	0.444×10^{-2}	0.160	0.948	0.951	1.09	1.37	2.95	3.43	252
124	45.	0.740×10^{-2}	0.096	0.812	0.812	1.42	1.54	3.18	3.80	252
125	60.	0.158×10^{-2}	0.600	1.282	1.370	8.42	4.22	3.23	9.96	252
126	60.	0.182×10^{-2}	0.520	1.258	1.318	4.24	2.54	2.91	5.73	252
127	60.	0.242×10^{-2}	0.490	1.204	1.254	1.63	2.01	3.01	3.97	225
128	60.	0.242×10^{-2}	0.392	1.163	1.191	1.96	1.94	2.86	3.97	252
129	60.	0.382×10^{-2}	0.248	1.032	1.041	1.16	1.38	2.87	3.39	252
130	60.	0.592×10^{-2}	0.160	0.957	0.960	1.18	1.40	2.90	3.43	252
131	60.	0.986×10^{-2}	0.096	0.791	0.791	1.51	1.58	3.01	3.72	252
132	90.	0.362×10^{-2}	0.490	1.100	1.145	3.36	2.72	3.06	5.29	225
133	90.	0.362×10^{-2}	0.392	1.142	1.170	2.92	2.17	2.88	4.64	252
134	90.	0.573×10^{-2}	0.248	0.954	0.962	1.43	1.45	2.85	3.50	252
135	90.	0.888×10^{-2}	0.160	0.850	0.853	1.39	1.45	2.95	3.56	252
136	90.	0.148×10^{-1}	0.096	0.728	0.729	1.74	1.67	2.94	3.80	252

Table 21: Continuation of table 20

Q^2 GeV ²	x	F_L	Δ_{stat}	Δ_{uncor}	Δ_{cor}	Δ_{tot}
1.5	0.279×10^{-4}	0.091	0.114	0.188	0.054	0.226
2.	0.427×10^{-4}	0.117	0.039	0.074	0.017	0.086
2.5	0.588×10^{-4}	0.147	0.025	0.050	0.008	0.056
3.5	0.877×10^{-4}	0.222	0.021	0.049	0.006	0.054
5.	0.129×10^{-3}	0.310	0.022	0.055	0.007	0.059
6.5	0.169×10^{-3}	0.263	0.023	0.059	0.008	0.064
8.5	0.224×10^{-3}	0.213	0.025	0.063	0.009	0.068
12.	0.319×10^{-3}	0.314	0.027	0.051	0.008	0.058
15.	0.402×10^{-3}	0.255	0.027	0.051	0.008	0.058
20.	0.540×10^{-3}	0.315	0.029	0.053	0.009	0.061
25.	0.686×10^{-3}	0.269	0.029	0.061	0.010	0.069
35.	0.103×10^{-2}	0.201	0.040	0.070	0.014	0.082
45.	0.146×10^{-2}	0.219	0.056	0.098	0.024	0.116

Table 23: The proton structure function $F_L(x, Q^2)$ obtained by averaging F_L data from table 22 for each Q^2 bin at the given values of Q^2 and x . Δ_{stat} , Δ_{uncor} , Δ_{cor} and Δ_{tot} are the statistical, uncorrelated systematic, correlated systematic and total uncertainty on F_L , respectively.

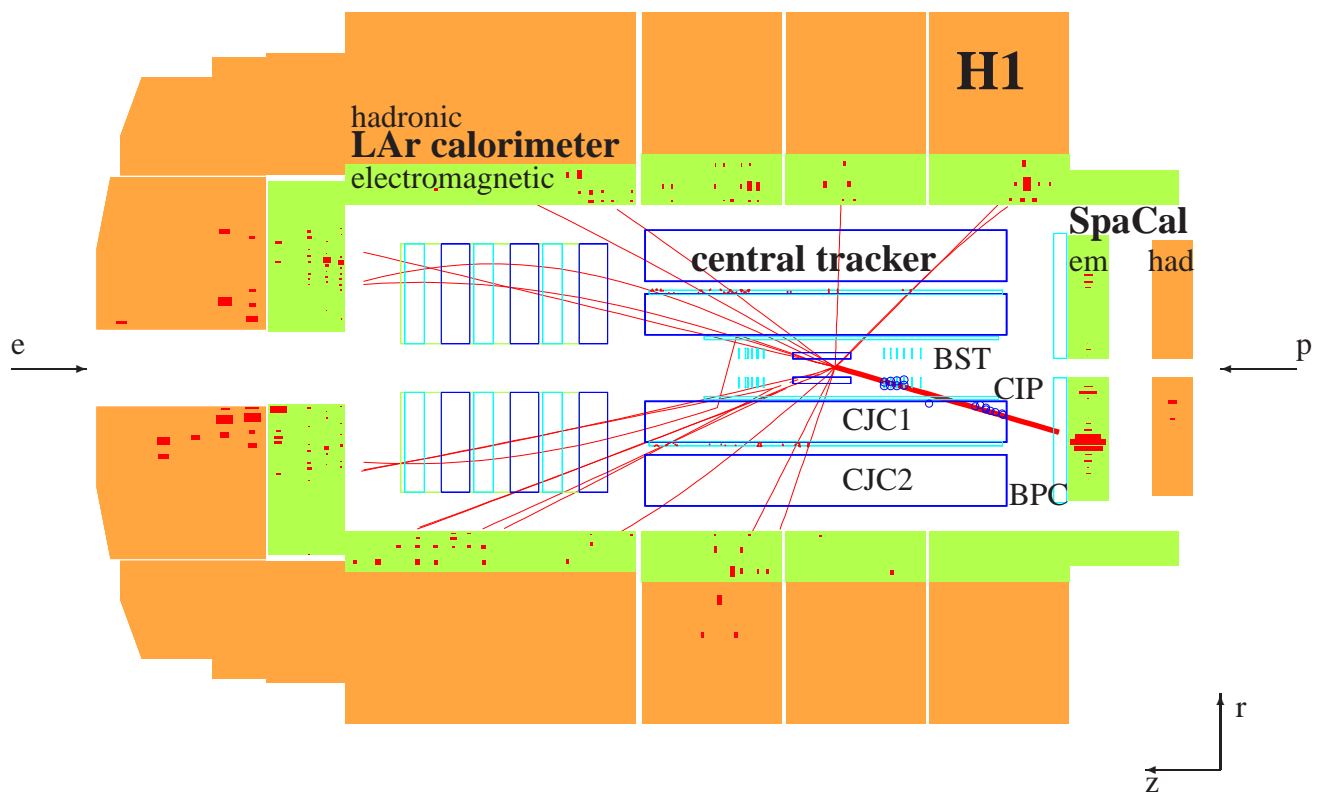


Figure 1: A high y event as reconstructed in the H1 detector. The scattered electron is measured in the SpaCal calorimeter. The electron trajectory, shown by a thick line, is reconstructed in the backward silicon tracker (BST) and in the inner central jet chamber (CJC1). The trajectory crosses the central inner proportional chamber (CIP) which is used for triggering. The backward proportional chamber (BPC) may assist the measurement of the scattering angle. The hadronic final state particles are detected in the central tracker, liquid argon calorimeter (LAR) and in the SpaCal electromagnetic and hadronic sections.

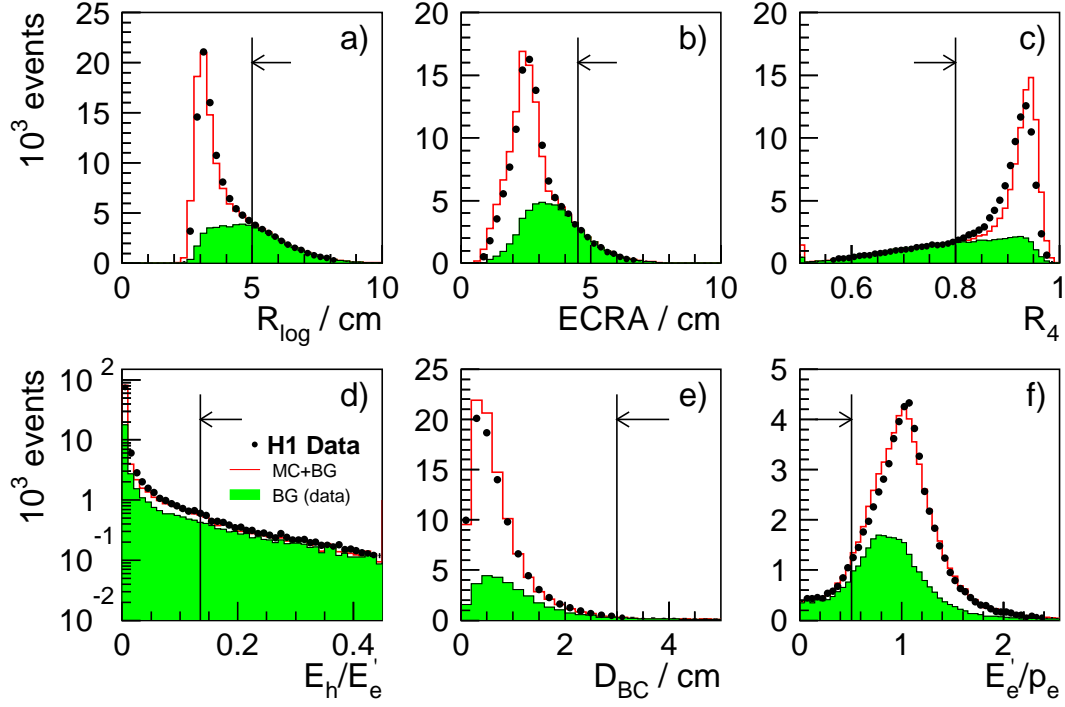


Figure 2: Distribution of variables used for the scattered lepton identification, for the $E_p = 460$ GeV sample: a) logarithmic cluster radius R_{\log} ; b) square root weighted cluster radius ECRA; c) fraction of energy in the four hottest cells of the cluster R_4 ; d) ratio of the energy in the hadronic section of the SpaCal in the cone behind the electron candidate to the electron candidate energy E_h/E'_e ; e) distance between BC track extrapolated to the SpaCal cluster Z and the cluster D_{BC} ; f) ratio of the lepton candidate energy to the track momentum E'_e/p_e . The data are shown as dots, the background as shaded histograms and the sum of the signal MC simulation and the background as open histograms. The vertical lines indicate the value of the electron identification cuts. The arrow points in the direction of the part of the distribution kept by the cut. The data are presented for $E'_e < 10$ GeV except for the E'_e/p_e plot which is shown for $E'_e < 7$ GeV.

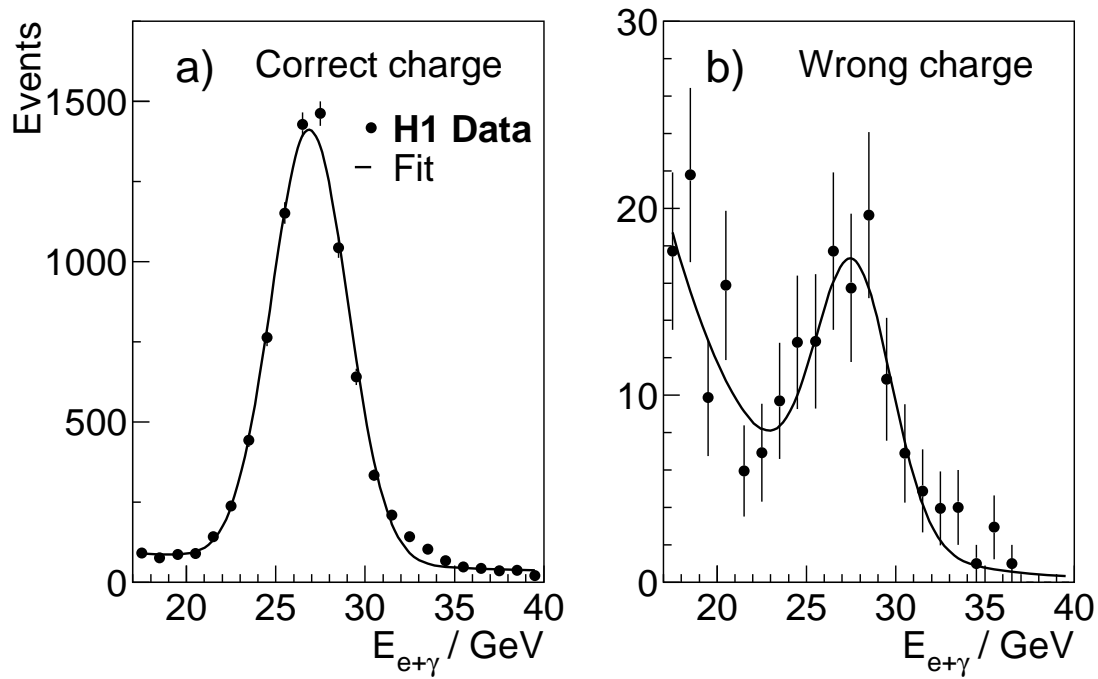


Figure 3: Sum of energies of the scattered electron and the photon for correct (a) and wrong (b) charge of the lepton candidate, for the dedicated selection of events with hard initial state radiation. The distributions are fitted by the sum of a Gaussian and exponential distributions, the fit result is shown by the line. The data are taken from the $E_p = 460$ GeV and $E_p = 575$ GeV samples.

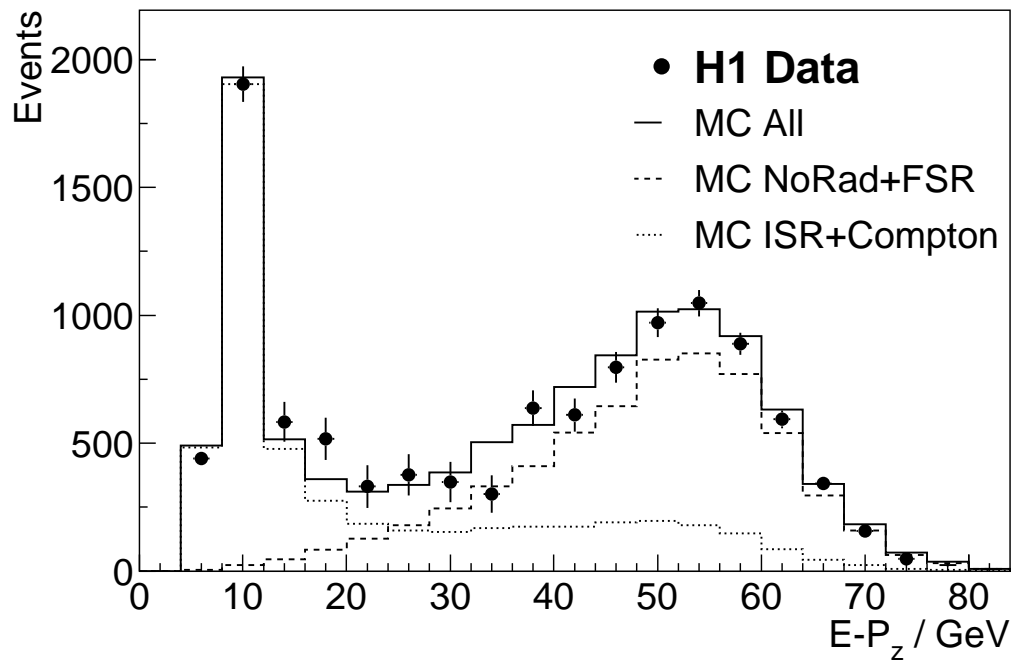


Figure 4: $E-P_z$ distribution for the $E_p = 575$ GeV sample passing all cuts excluding cut on $E-P_z$ for $E'_e < 5$ GeV. The dots show the background subtracted data with statistical errors, the solid line is the total MC prediction, the dashed line, labeled MC NoRad+FSR, is the sum non-radiative and final state radiation components and the dotted line, labeled MC ISR+Compton, shows the sum of initial state radiation and QED-Compton contributions.

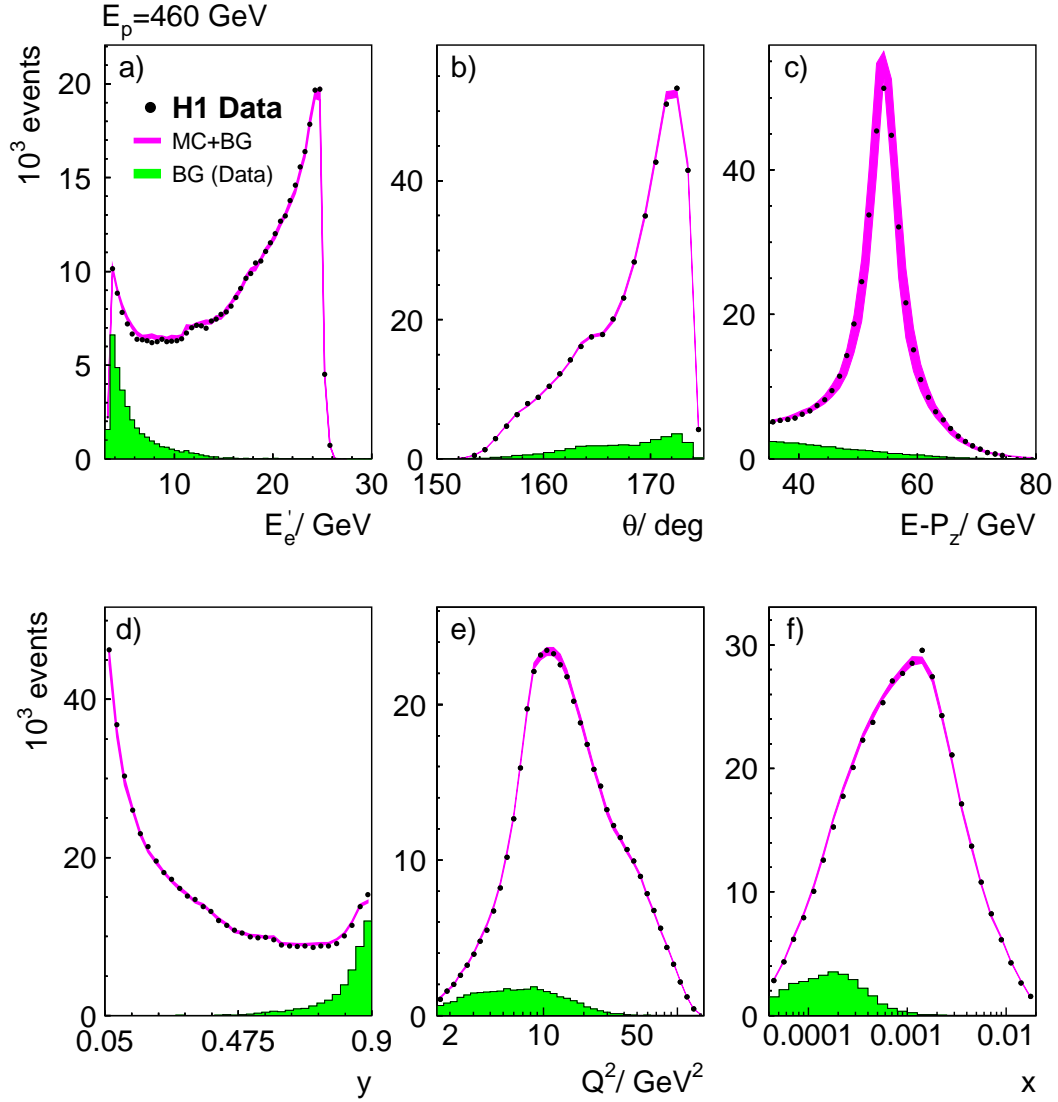


Figure 5: Distributions of the scattered electron energy E_e' (a), polar angle θ_e (b), $E - P_z$ (c) and of the kinematic variables y (d), Q^2 (e), x (f) for events passing all analysis cuts from $E_p = 460 \text{ GeV}$ sample. Data are shown as dots with statistical errors, the shaded histograms show the data driven estimation of the background and the shaded bands represent the simulation of DIS signal with statistical and systematic uncertainties added in quadrature.

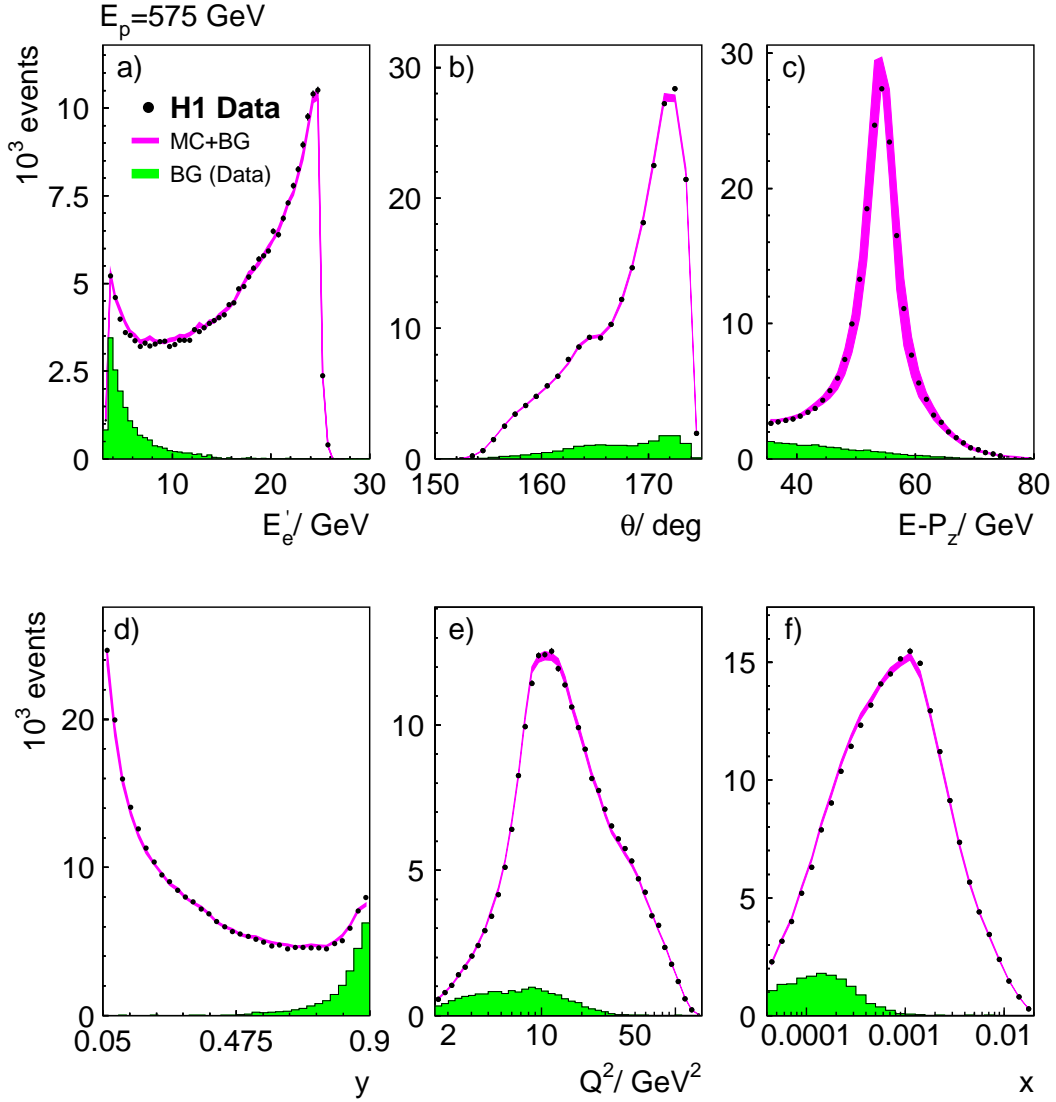


Figure 6: Distributions of the scattered electron energy E_e' (a), polar angle θ_e (b), $E - P_z$ (c) and of the kinematic variables y (d), Q^2 (e), x (f) for events passing all analysis cuts from $E_p = 575 \text{ GeV}$ sample. Data are shown as dots with statistical errors, the shaded histograms show the data driven estimation of the background and the shaded bands represent the simulation of DIS signal with statistical and systematic uncertainties added in quadrature.

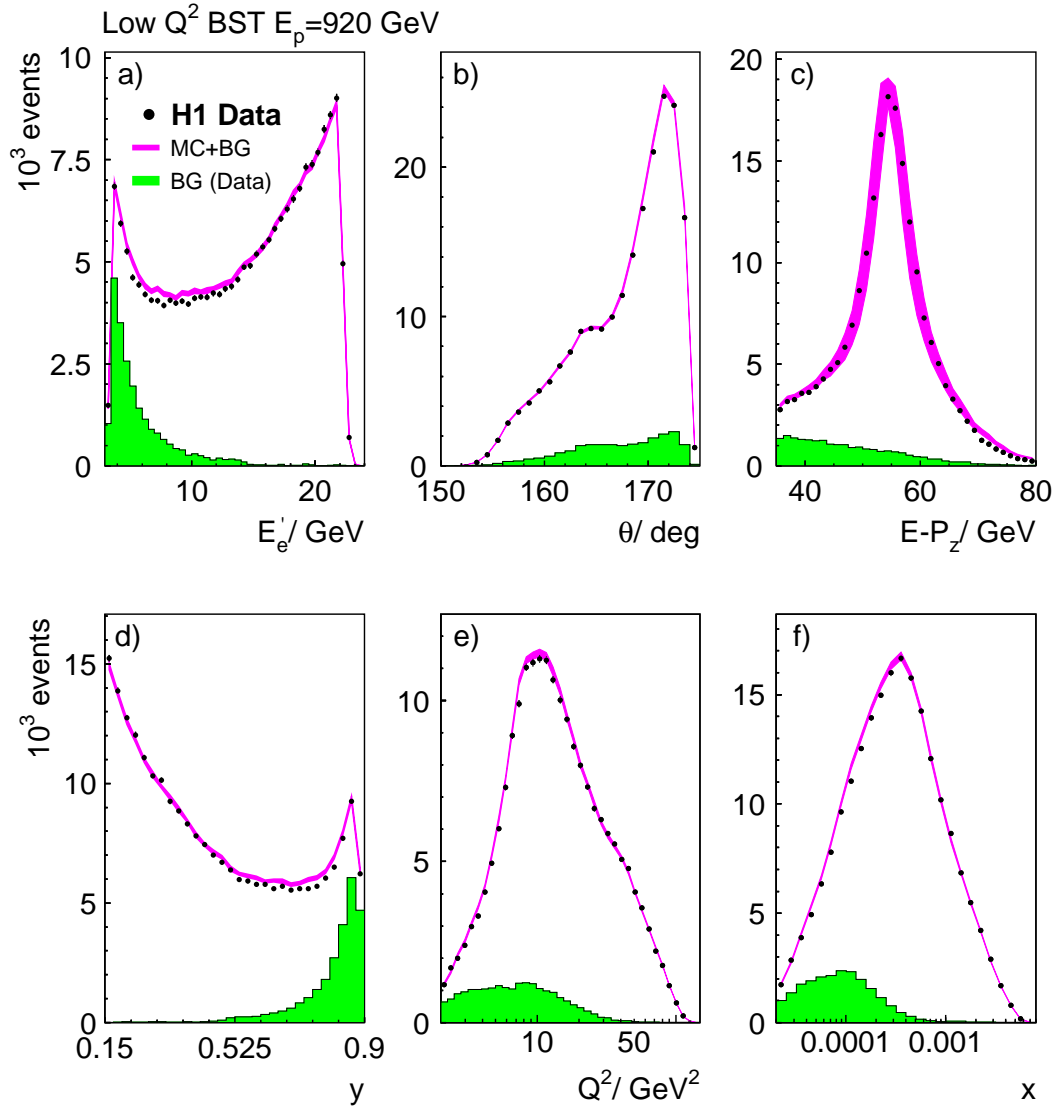


Figure 7: Distributions of the scattered electron energy E'_e (a), polar angle θ_e (b), $E - P_z$ (c) and of the kinematic variables y (d), Q^2 (e), x (f) for events passing all analysis cuts from low Q^2 BST $E_p = 920$ GeV sample. Data are shown as dots with statistical errors, the shaded histograms show the data driven estimation of the background and the shaded bands represent the simulation of DIS signal with statistical and systematic uncertainties added in quadrature.

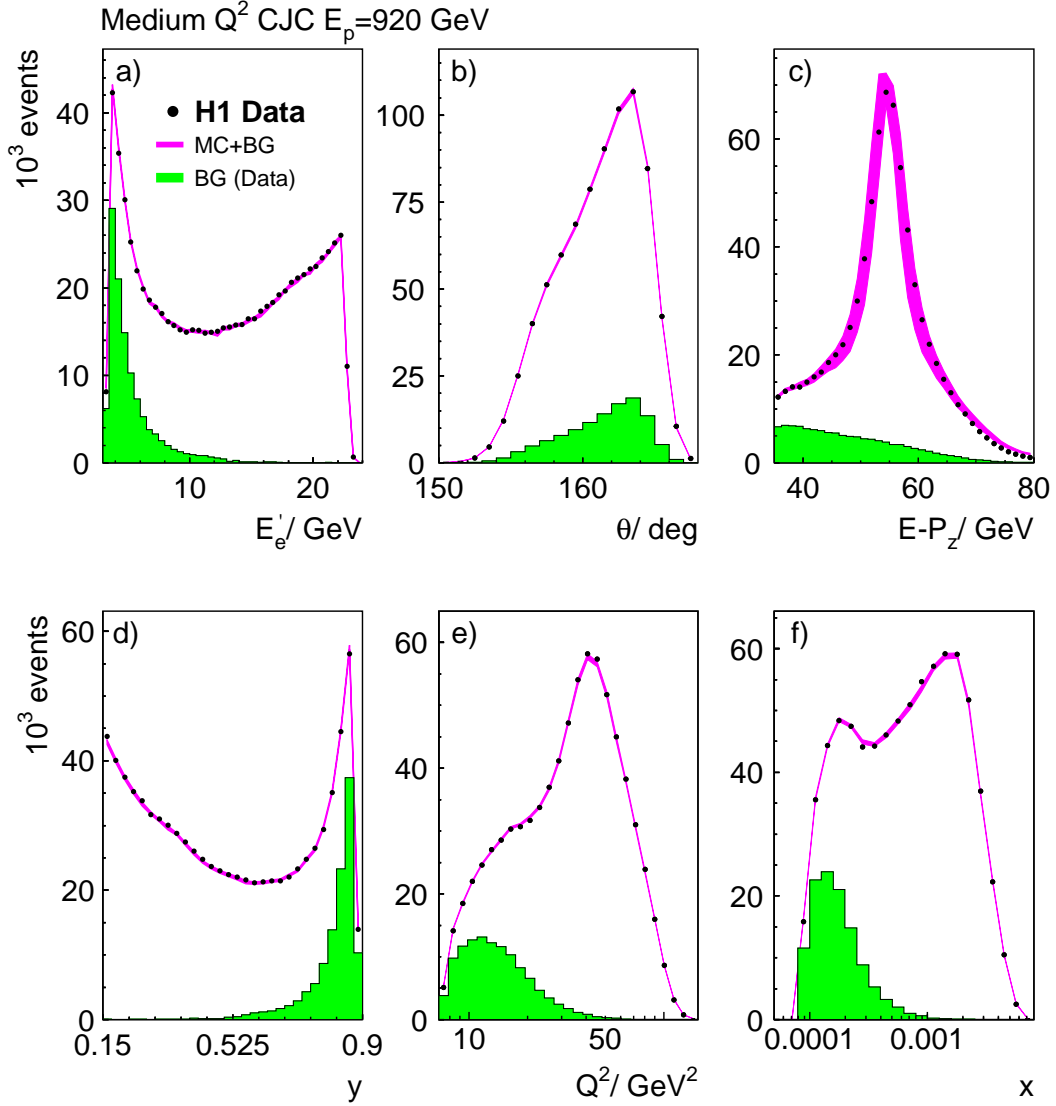


Figure 8: Distributions of the scattered electron energy E_e' (a), polar angle θ_e (b), $E - P_z$ (c) and of the kinematic variables y (d), Q^2 (e), x (f) for events passing all analysis cuts from medium Q^2 CJC $E_p = 920$ GeV sample. Data are shown as dots with statistical errors, the shaded histograms show the data driven estimation of the background and the shaded bands represent the simulation of DIS signal with statistical and systematic uncertainties added in quadrature.

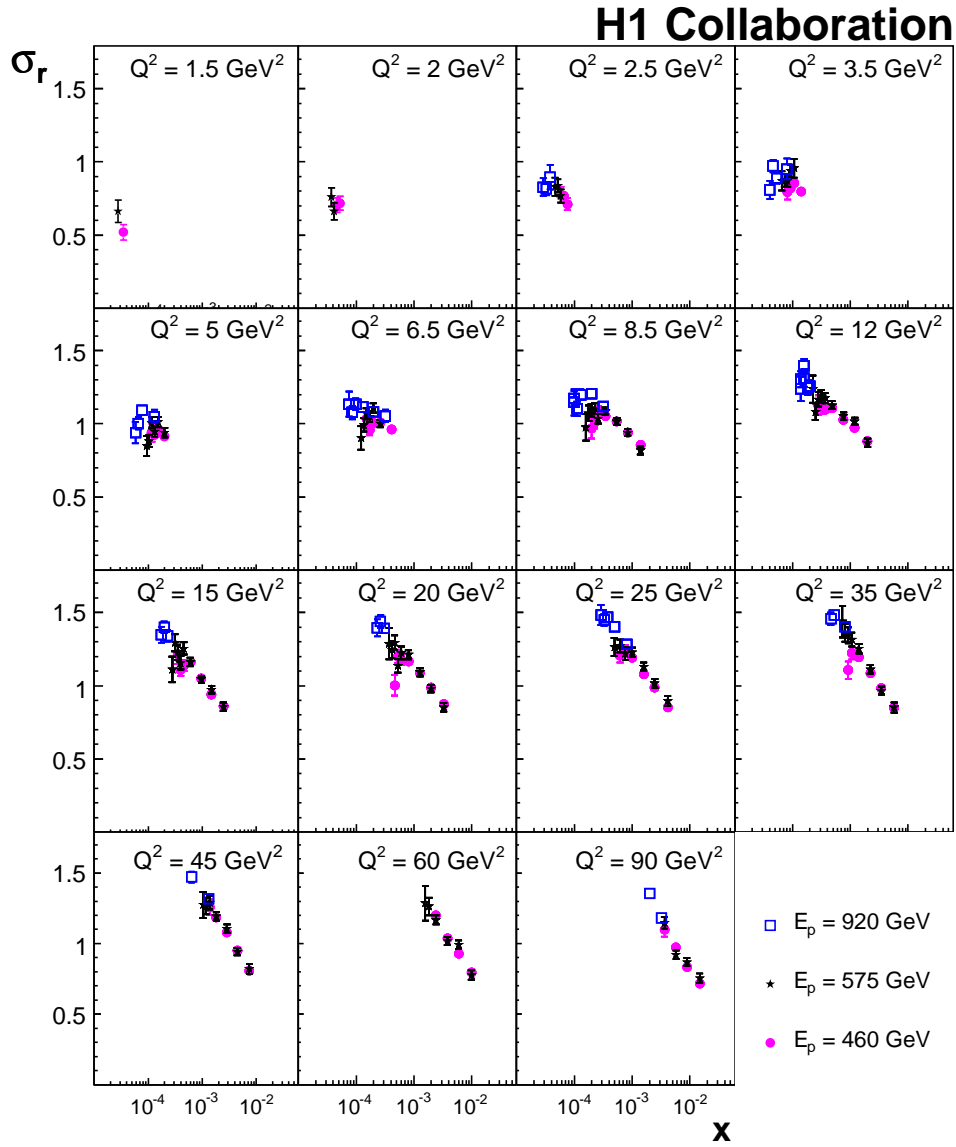


Figure 9: Results on the reduced cross section σ_r as determined from the $E_p = 920$ GeV, $E_p = 575$ GeV and $E_p = 460$ GeV samples. The error bars represent statistical and systematic uncertainties added in quadrature.

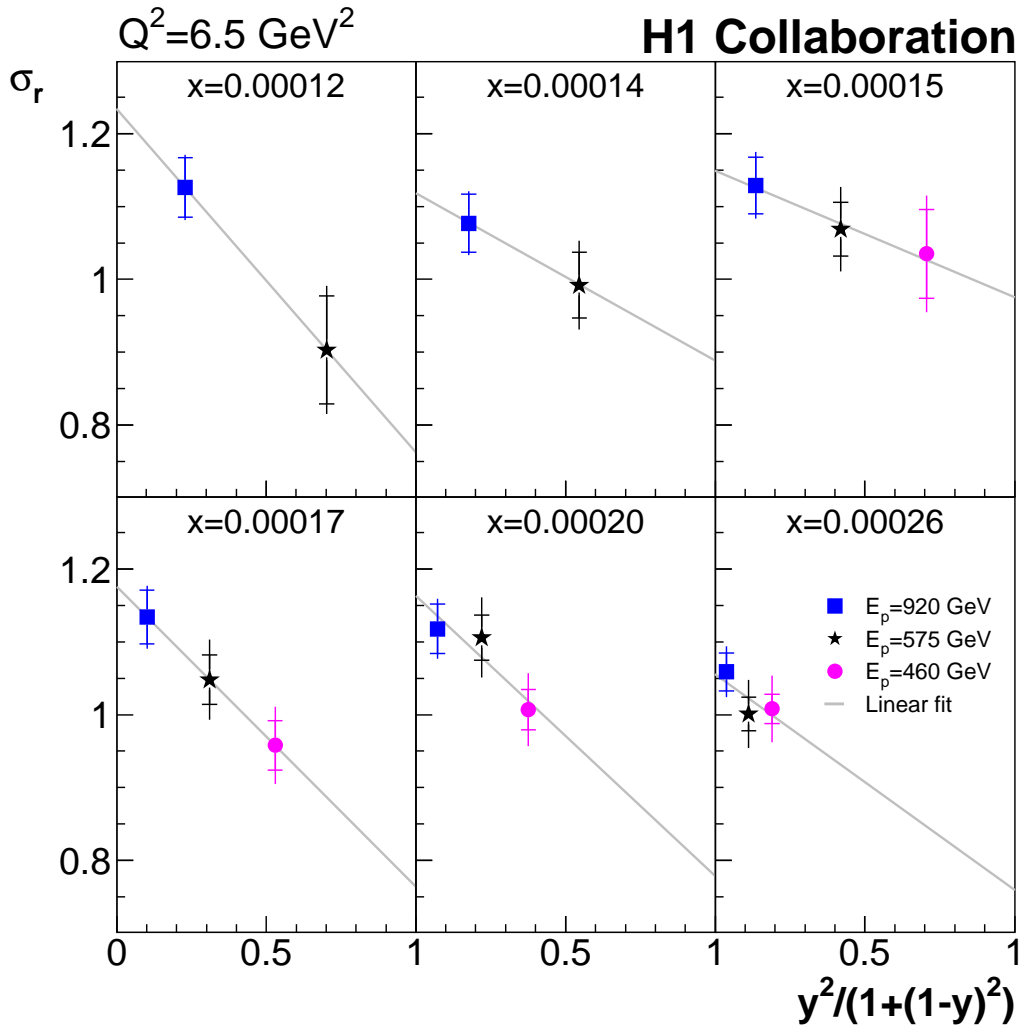


Figure 10: The reduced DIS cross section σ_r as a function of $y^2/(1+(1-y)^2)$ for six values of x at $Q^2 = 6.5 \text{ GeV}^2$, measured for proton beam energies of $E_p = 920, 575$ and 460 GeV . The inner error bars denote the statistical error, the outer error bars show statistical and systematic uncertainties added in quadrature. The luminosity uncertainty is not included in the error bars. The slope of the straight-line fits is determined by the structure function $F_L(x, Q^2)$.

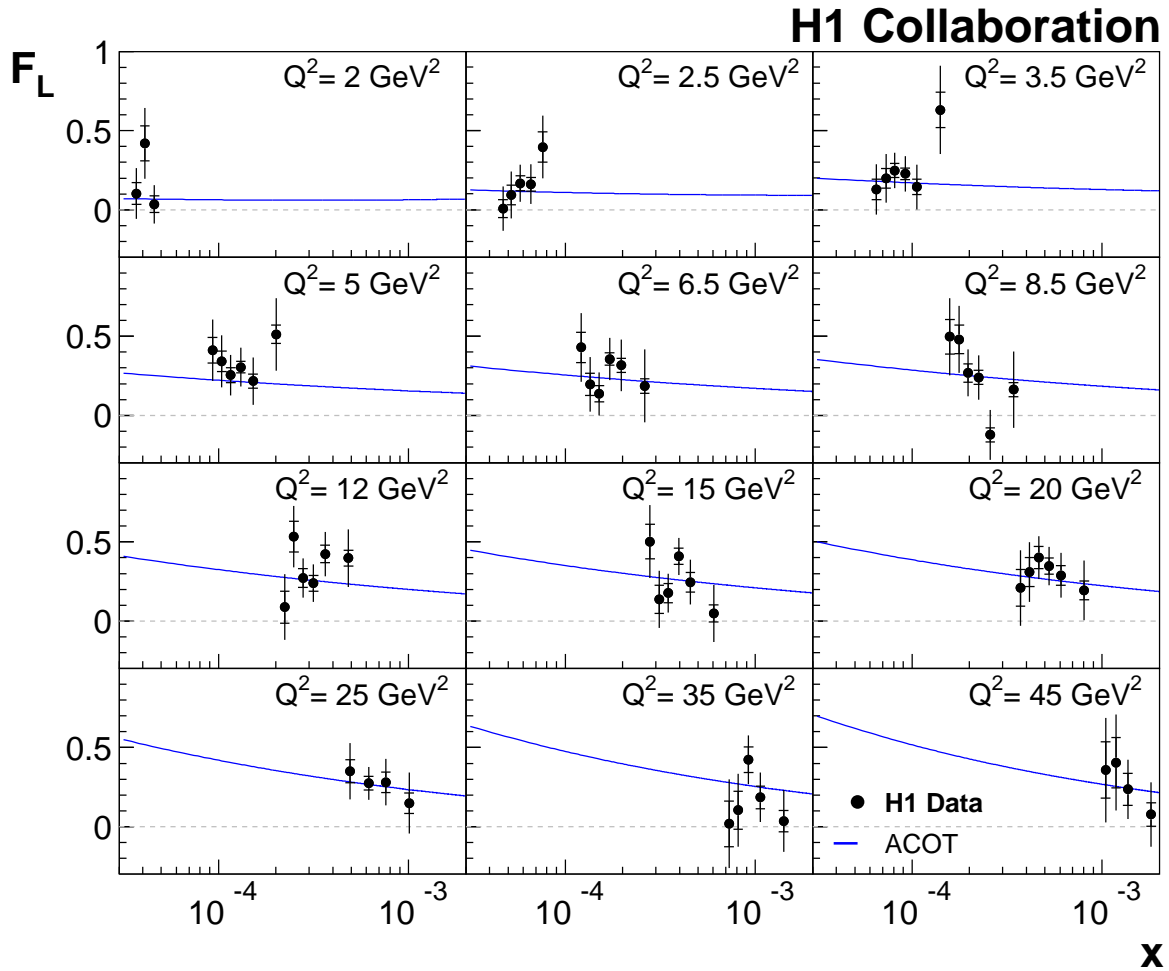


Figure 11: The proton structure function $F_L(x, Q^2)$. The inner error bars represent statistical error, the full error bars include the statistical and systematic uncertainties added in quadrature, excluding 0.5% global normalisation uncertainty. The curves represent predictions of the DGLAP fit in the ACOT scheme.

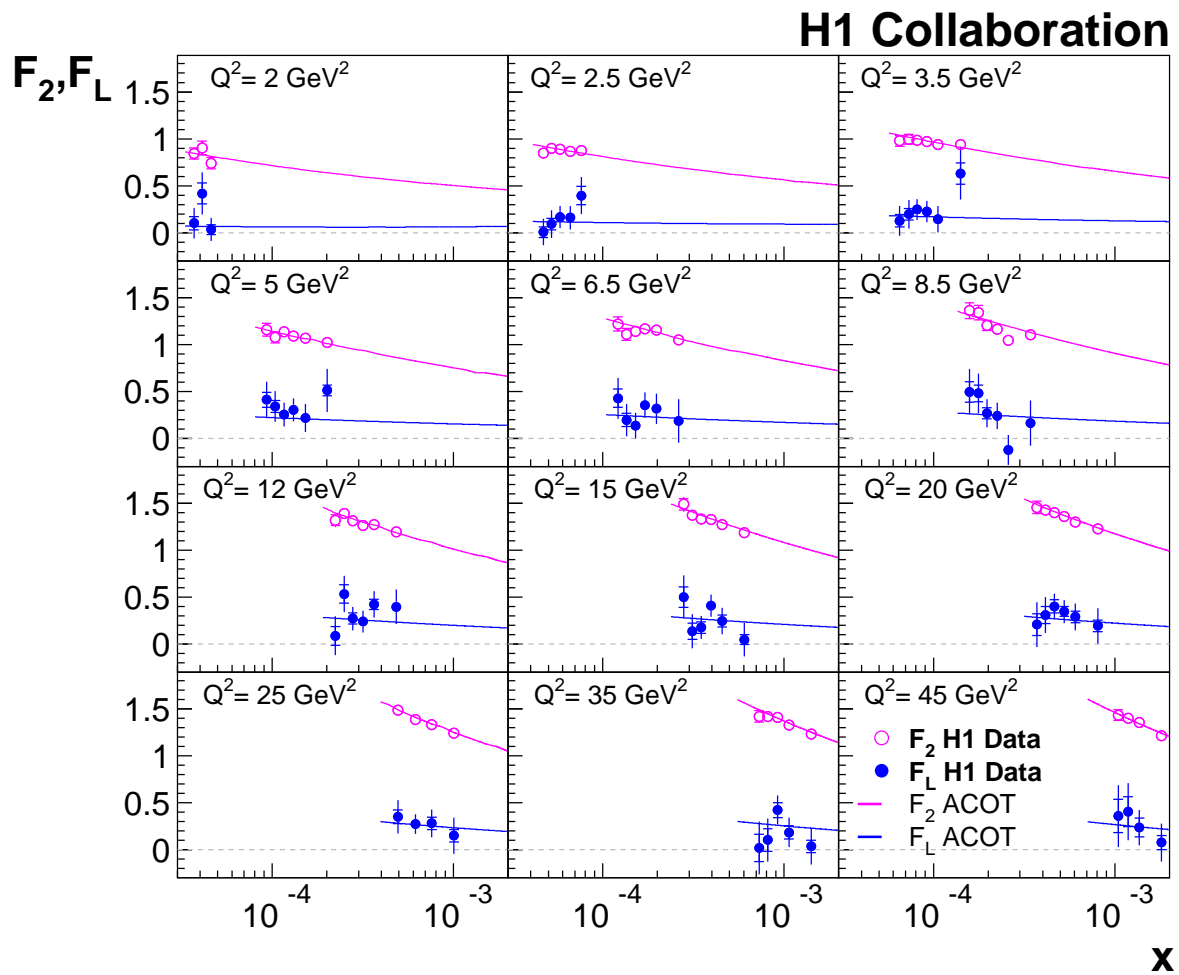


Figure 12: The proton structure functions $F_2(x, Q^2)$ and $F_L(x, Q^2)$. The inner error bars represent statistical error, the full error bars include the statistical and systematic uncertainties added in quadrature, excluding 0.5% global normalisation uncertainty. The curves represent predictions of the DGLAP fit in the ACOT scheme for the structure functions F_2 and F_L .

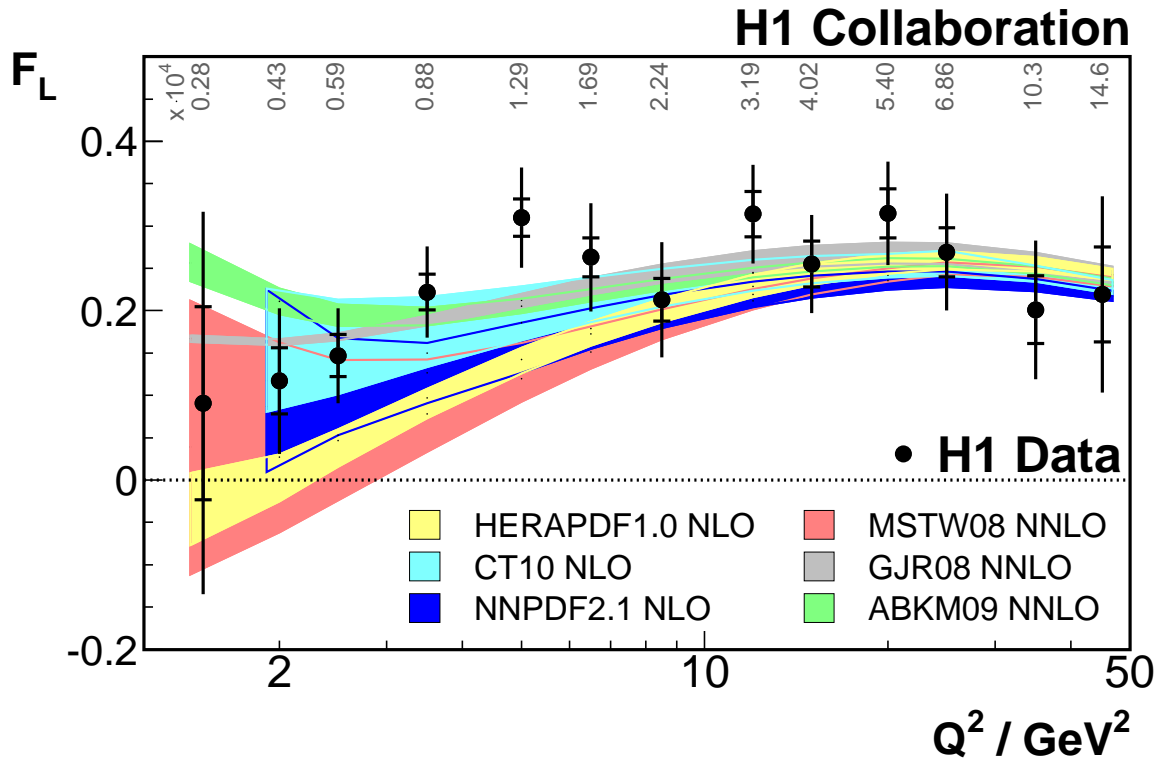


Figure 13: The proton structure function F_L shown as a function of Q^2 . The average x values for each Q^2 are indicated. The inner error bars represent statistical error, the full error bars include the statistical and systematic uncertainties added in quadrature. The bands represent predictions based on HERAPDF1.0, CTEQ6.6 and NNPDF2.1 NLO as well as DGLAP ACOT and RT as well as MSTW08, GJR08 and ABKM09 NNLO calculations.

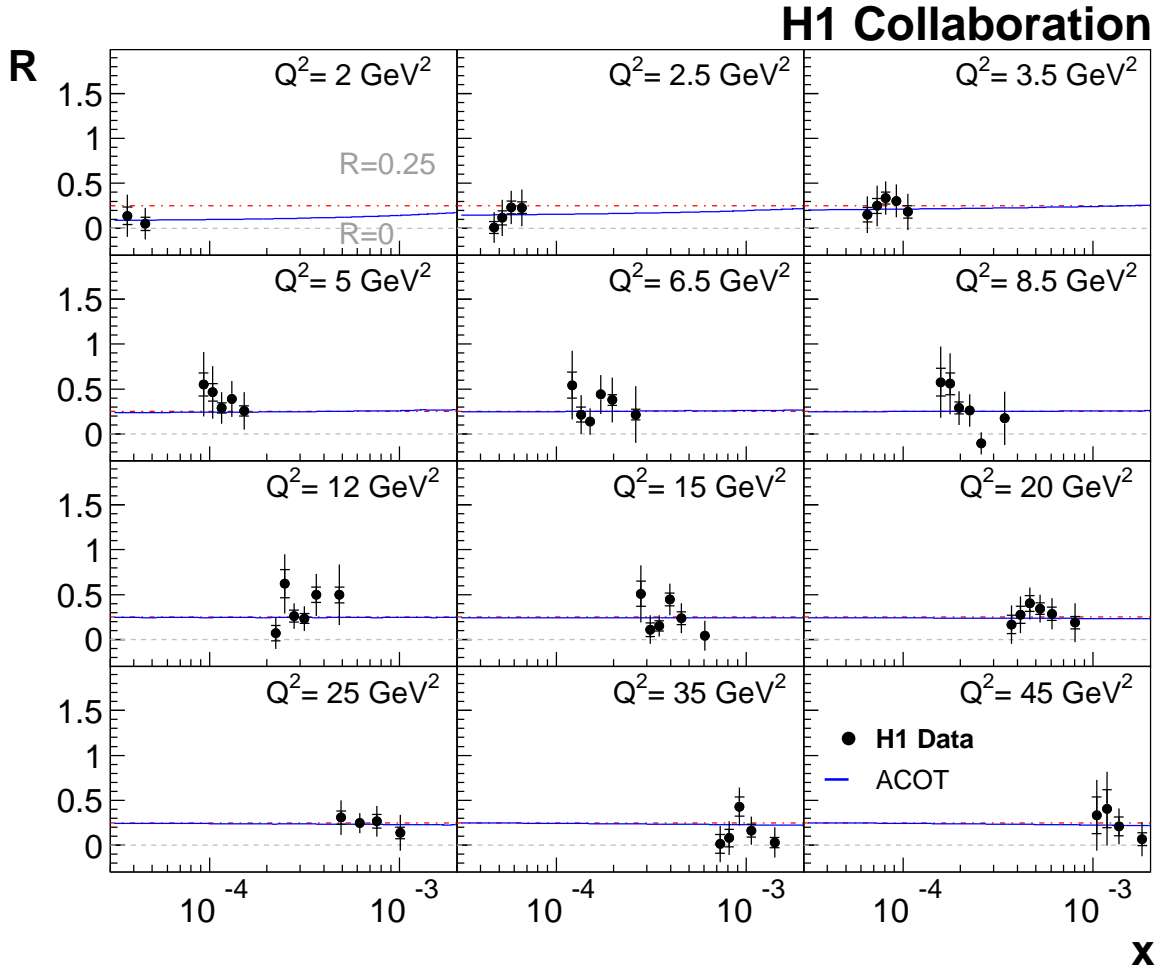


Figure 14: The ratio $R = F_L(x, Q^2)/(F_2(x, Q^2) - F_L(x, Q^2))$. The inner error bars represent statistical error, the full error bars include the statistical and systematic uncertainties added in quadrature. The solid curves represent predictions of the DGLAP fit in ACOT scheme.

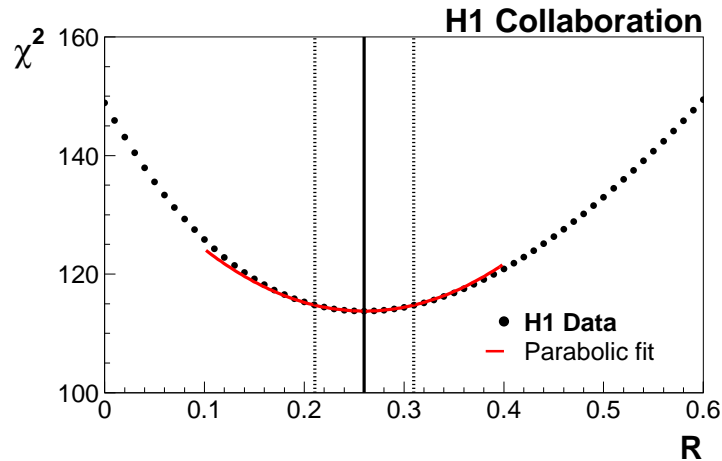


Figure 15: χ^2 for combination of the data taken at $E_p = 920, 575$ and 460 GeV as a function of R assuming R being constant. The solid line shows parabolic fit around the χ^2 minimum. The solid vertical line shows the value of R_{\min} at which χ^2 has the minimum and the dotted vertical lines correspond to the total uncertainty of R_{\min} .

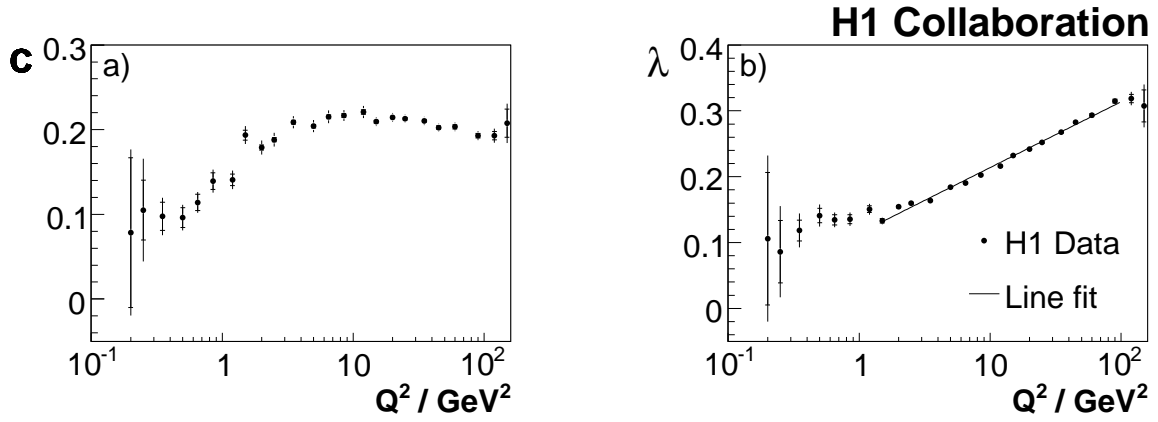


Figure 16: Coefficients c and λ , as defined in equation 15, determined from a fit to the data as a function of Q^2 . The inner error bars represent statistical uncertainties. The outer error bars contain the statistical and systematic uncertainties added in quadrature. The line in b) is from a straight-line fit for $Q^2 \geq 2 \text{ GeV}^2$.

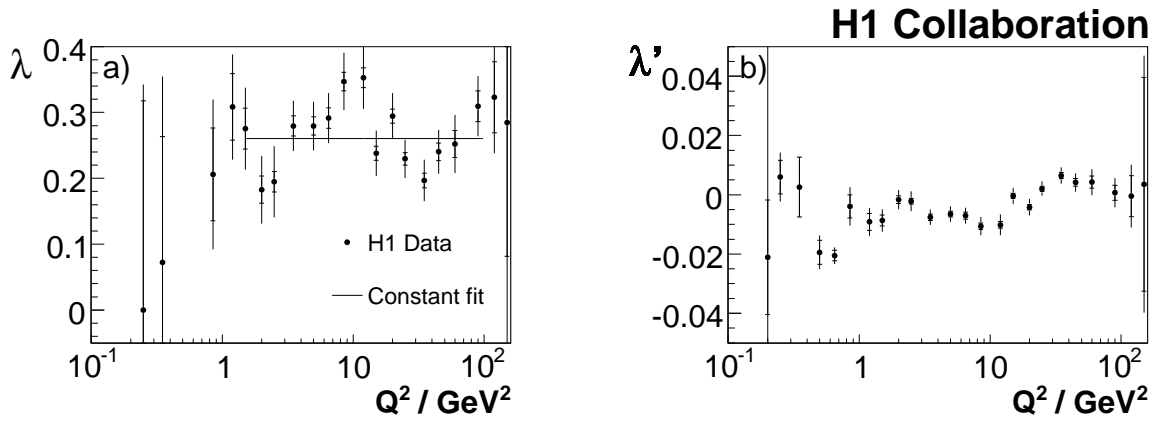


Figure 17: Coefficients λ and λ' , as defined in equation 16, determined from a fit to the H1 data as a function of Q^2 . The inner error bars represent statistical uncertainties. The outer error bars contain the statistical and systematic uncertainties added in quadrature. The line in a) is from a constant fit for $Q^2 \geq 2 \text{ GeV}^2$.

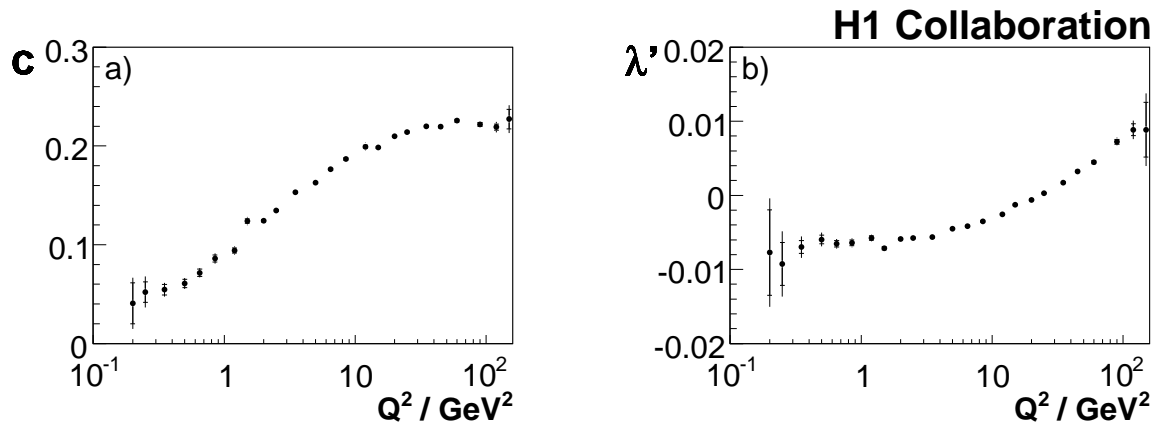


Figure 18: Coefficients c and λ' , as defined in equation 16, determined from a fit to the H1 data as a function of Q^2 with fixed $\lambda = 0.25$. The inner error bars represent statistical uncertainties. The outer error bars contain the statistical and systematic uncertainties added in quadrature.

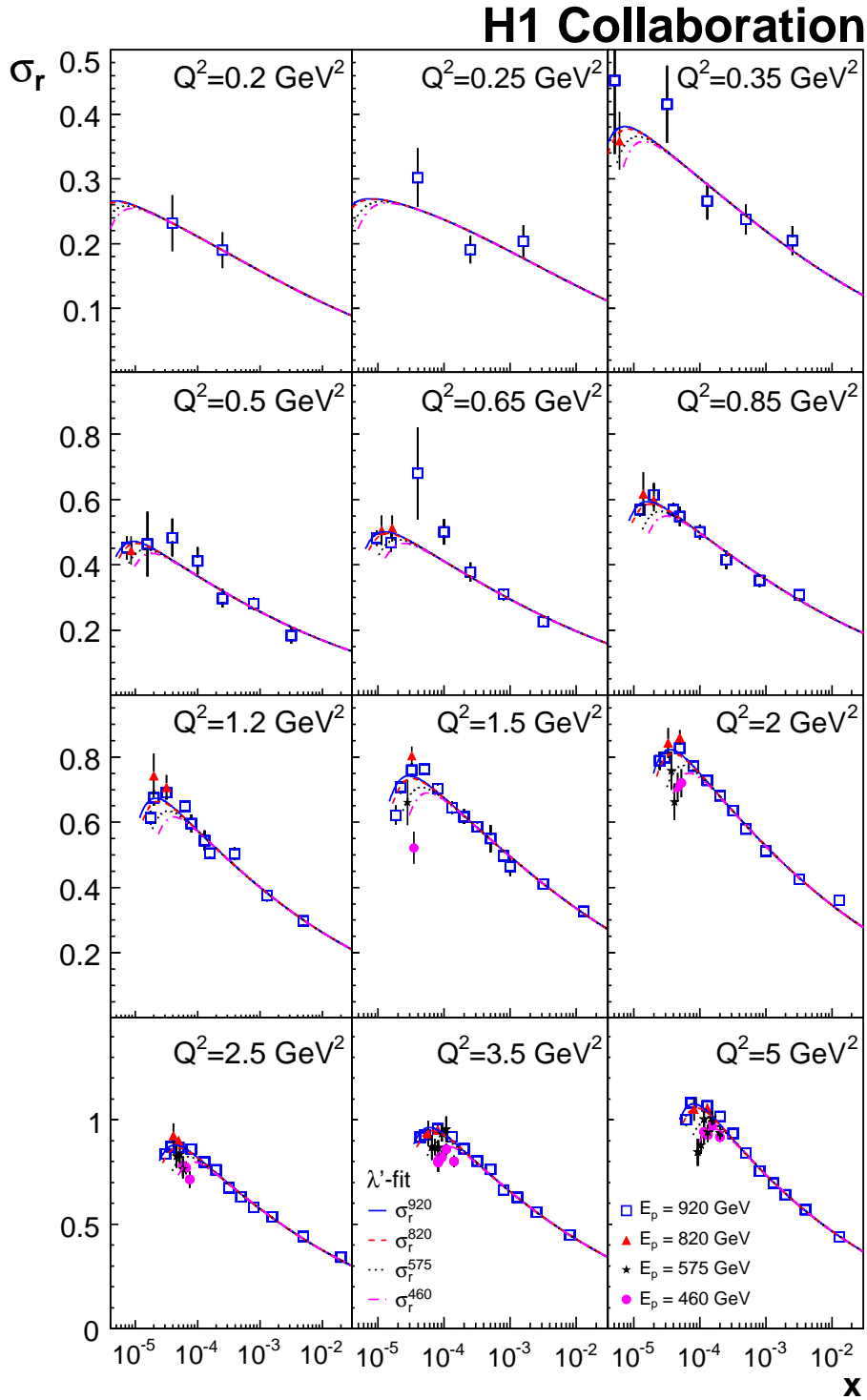


Figure 19: Reduced cross section σ_r as a function of x for different Q^2 bins for $Q^2 \leq 5 \text{ GeV}^2$. The H1 data are compared to the λ' fit result (shown by curves) for different proton beam energies E_p .

H1 Collaboration

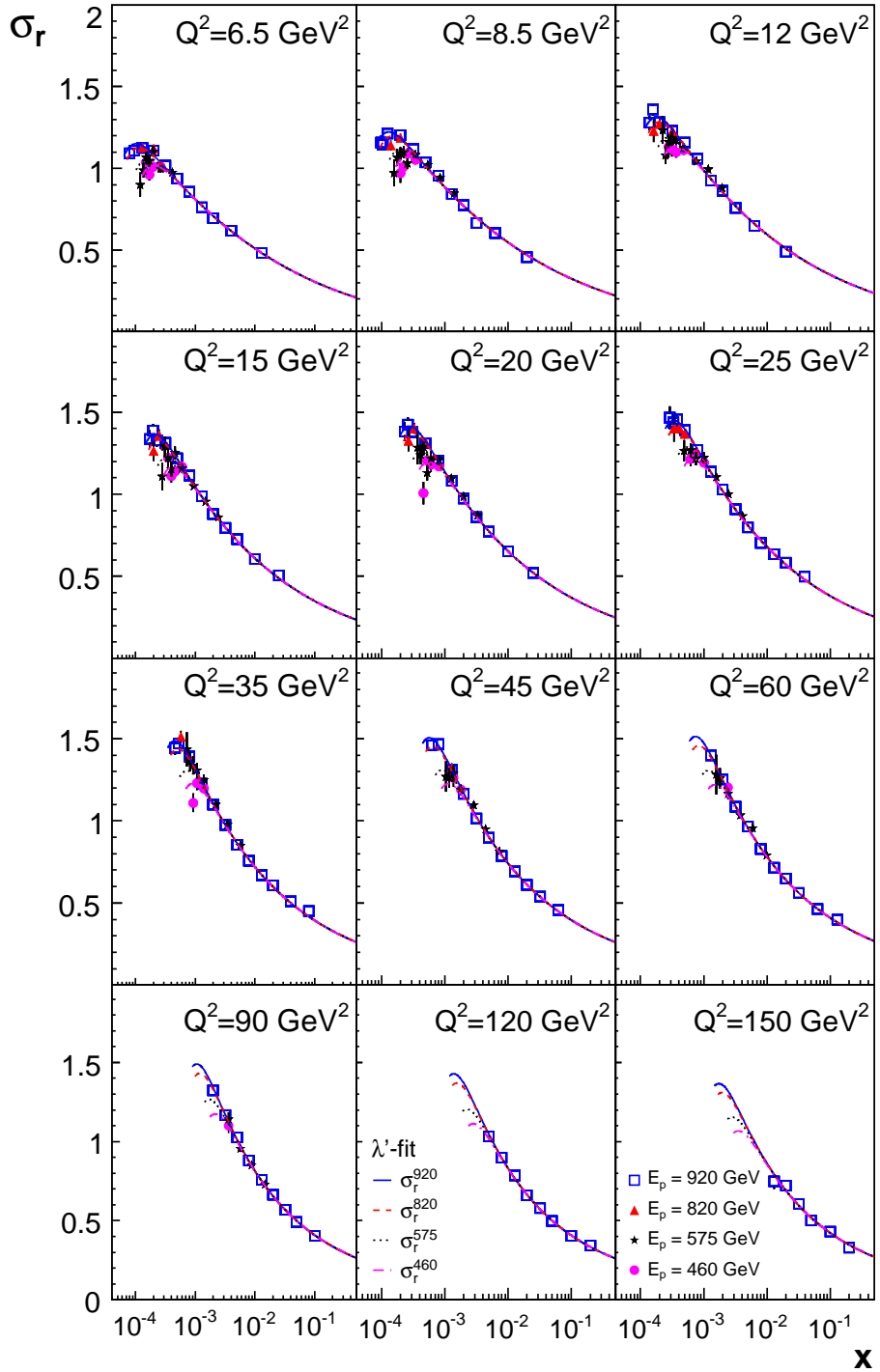


Figure 20: Reduced cross section σ_r as a function of x for different Q^2 bins for $Q^2 > 5 \text{ GeV}^2$. The H1 data are compared to the λ' fit result (shown by curves) for different proton beam energies E_p .

H1 Collaboration

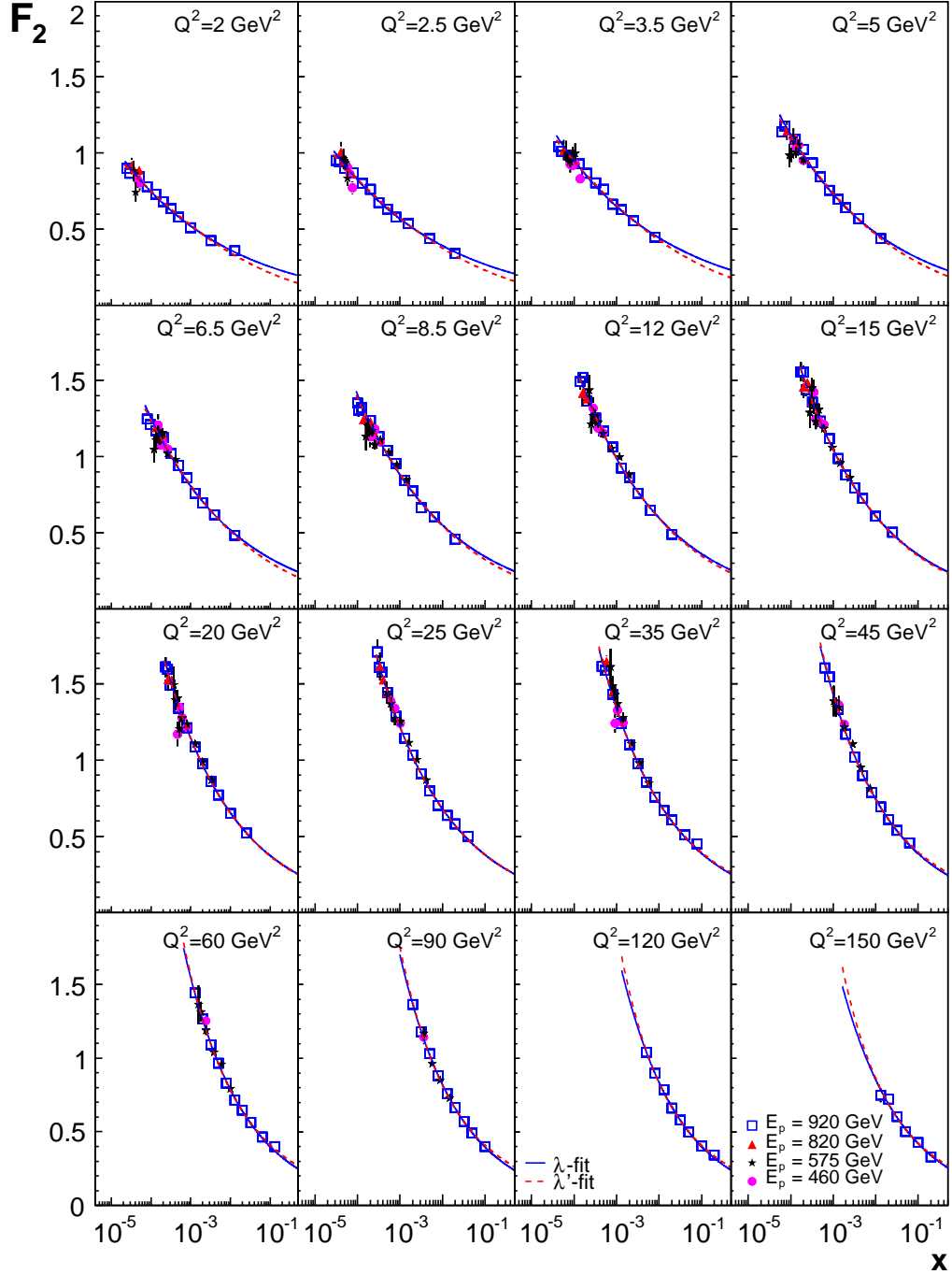


Figure 21: Structure function $F_2(x, Q^2)$ as a function of x calculated from the reduced cross section using $R = 0.26$ for different Q^2 bins. The H1 data for different proton beam energies E_p are compared to the λ and λ' fit results.

H1 Collaboration

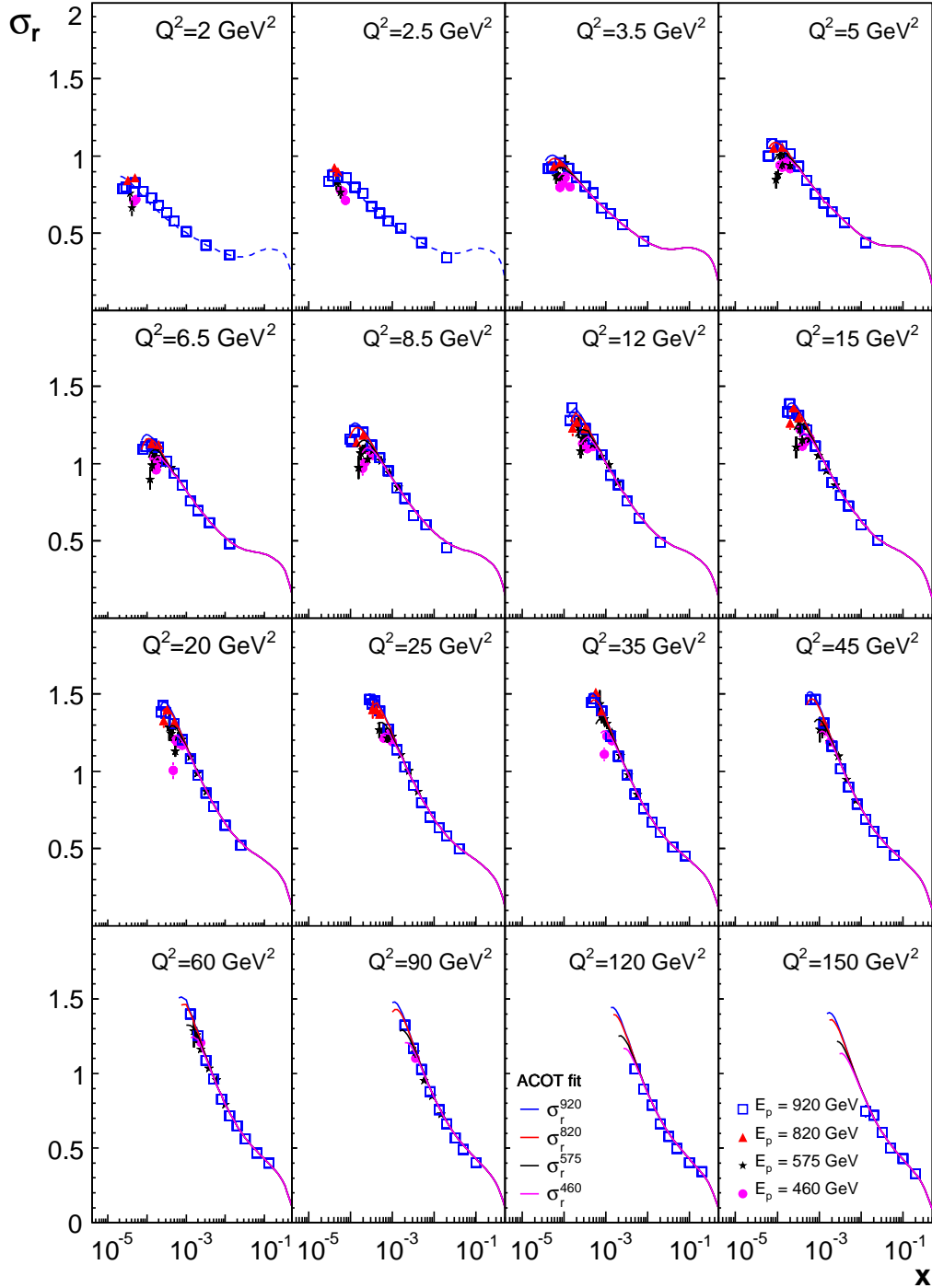


Figure 22: The reduced cross-section measurements taken at different proton beam energies E_p compared to the DGLAP fit in the ACOT scheme (shown by curves) for $2.0 \leq Q^2 \leq 150 \text{ GeV}^2$. The dashed line for $Q^2 \leq 2.5 \text{ GeV}^2$ corresponds to the fit extrapolation.

H1 Collaboration

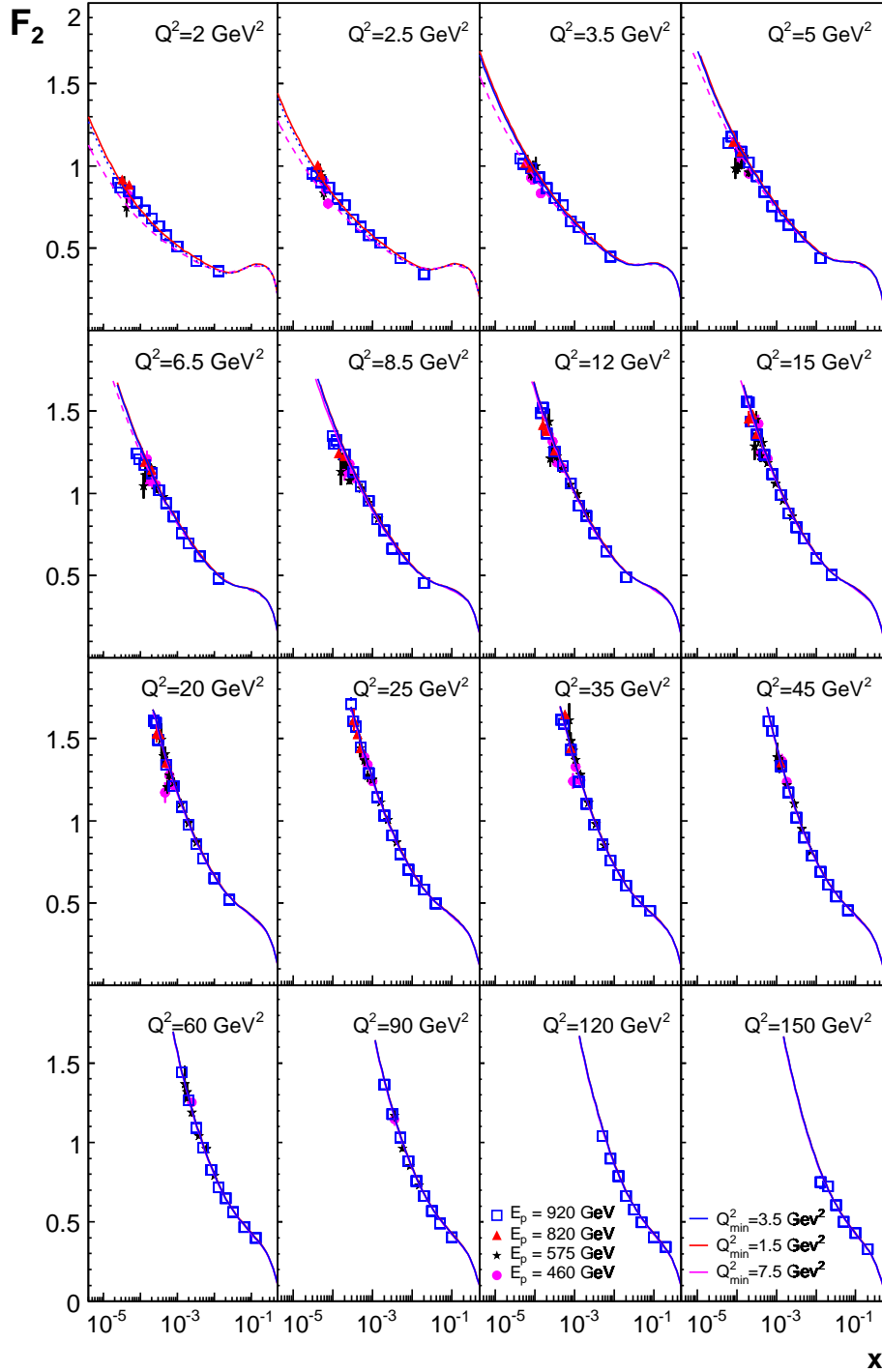


Figure 23: The structure function F_2 as a function of x calculated from the reduced cross section using $R = 0.26$ for different Q^2 bins. The H1 data for different proton beam energies E_p are compared to the DGLAP fit in the ACOT scheme with different values of the Q^2_{min} cut. The dashed and dotted lines correspond to the extrapolation of the fits to lower Q^2 values.

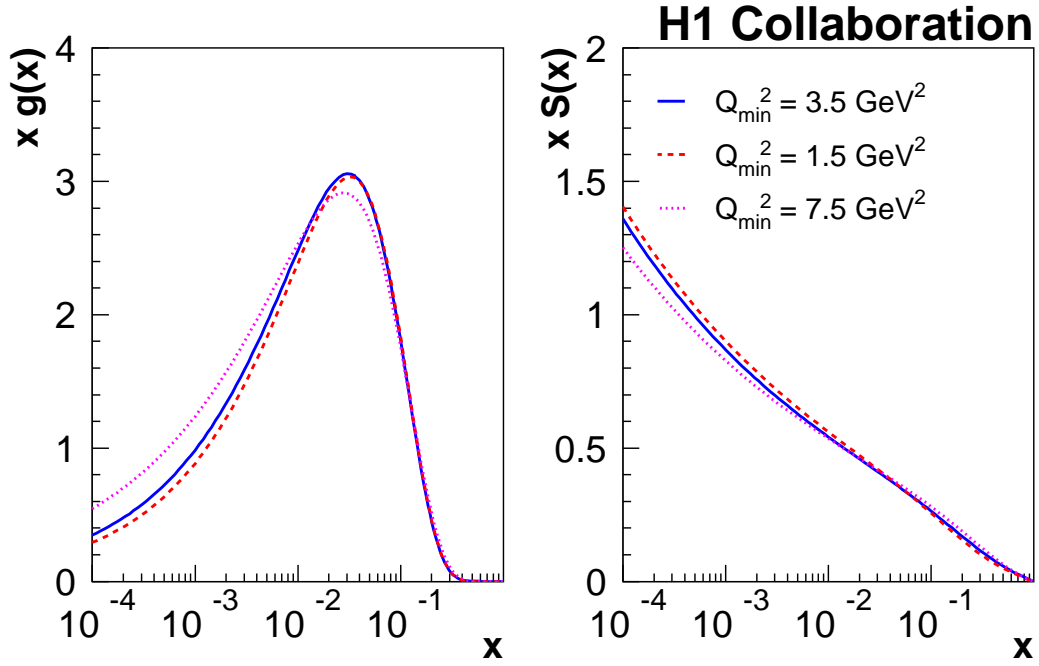


Figure 24: Gluon and sea quark PDFs shown at the starting scale $Q_0^2 = 1.9 \text{ GeV}^2$ for different values of Q_{min}^2 .

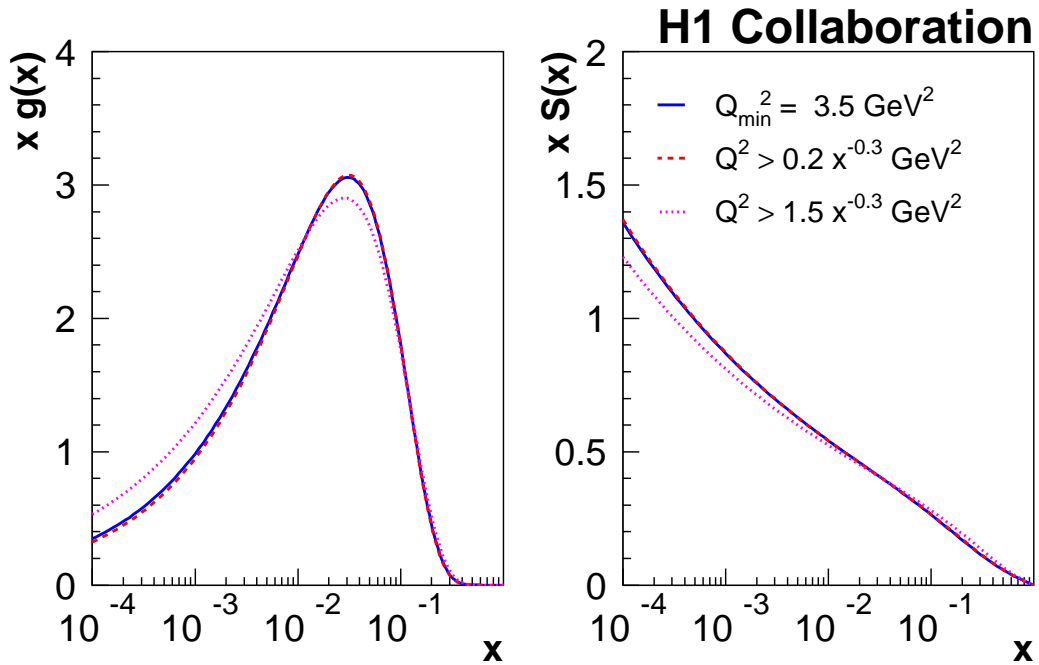


Figure 25: Gluon and sea quark PDFs shown at the starting scale $Q_0^2 = 1.9 \text{ GeV}^2$ for the central fit with $Q_{min}^2 = 3.5 \text{ GeV}^2$ and for the fits with additional cuts $Q^2 > A_s x^{-0.3}$ where $A_s = 0.2$ and $A_s = 1.5$.

H1 Collaboration

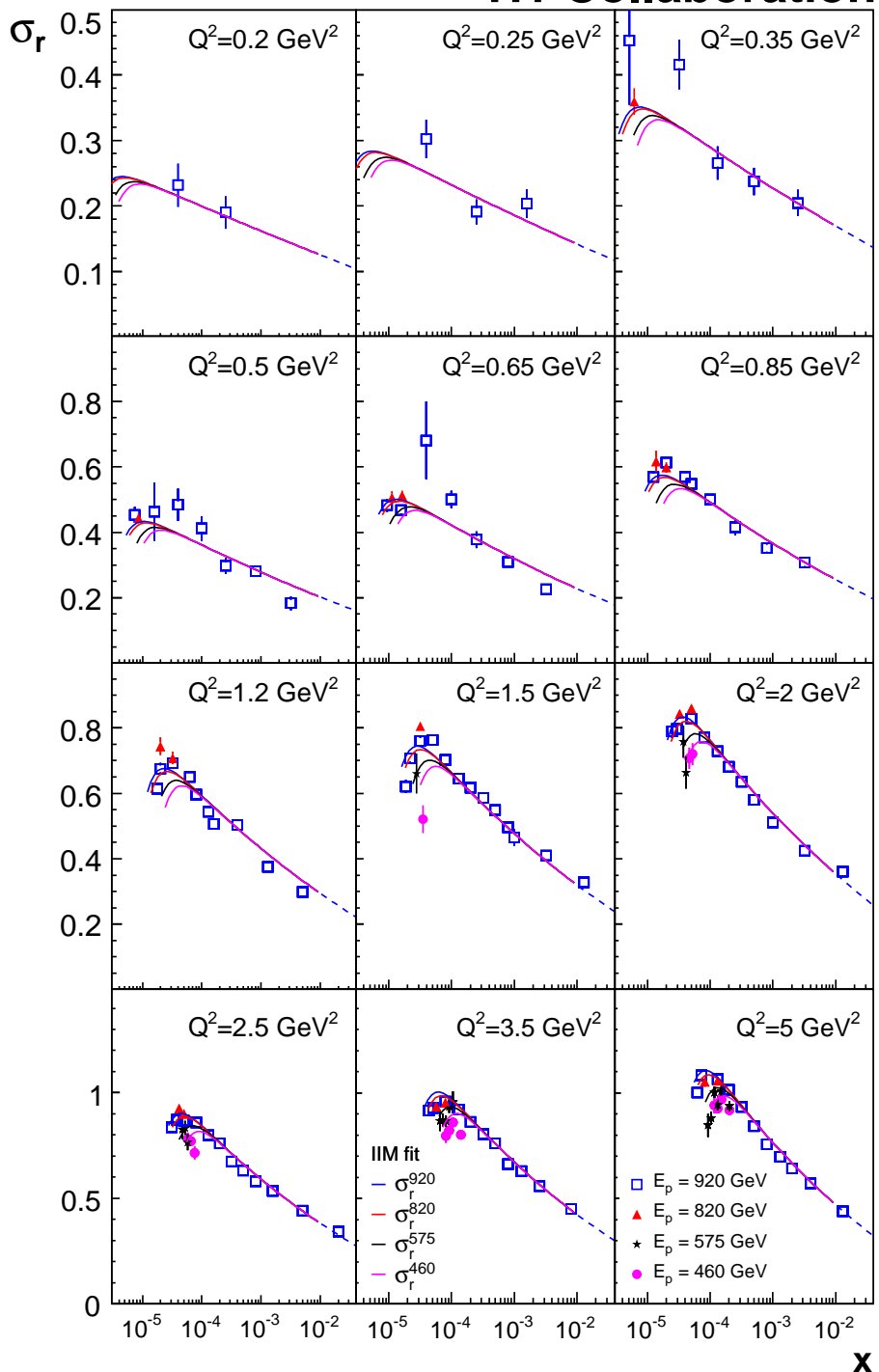


Figure 26: Reduced cross-section data taken at different proton beam energies E_p compared to IIM fit results for $0.2 \leq Q^2 \leq 5 \text{ GeV}^2$.

H1 Collaboration

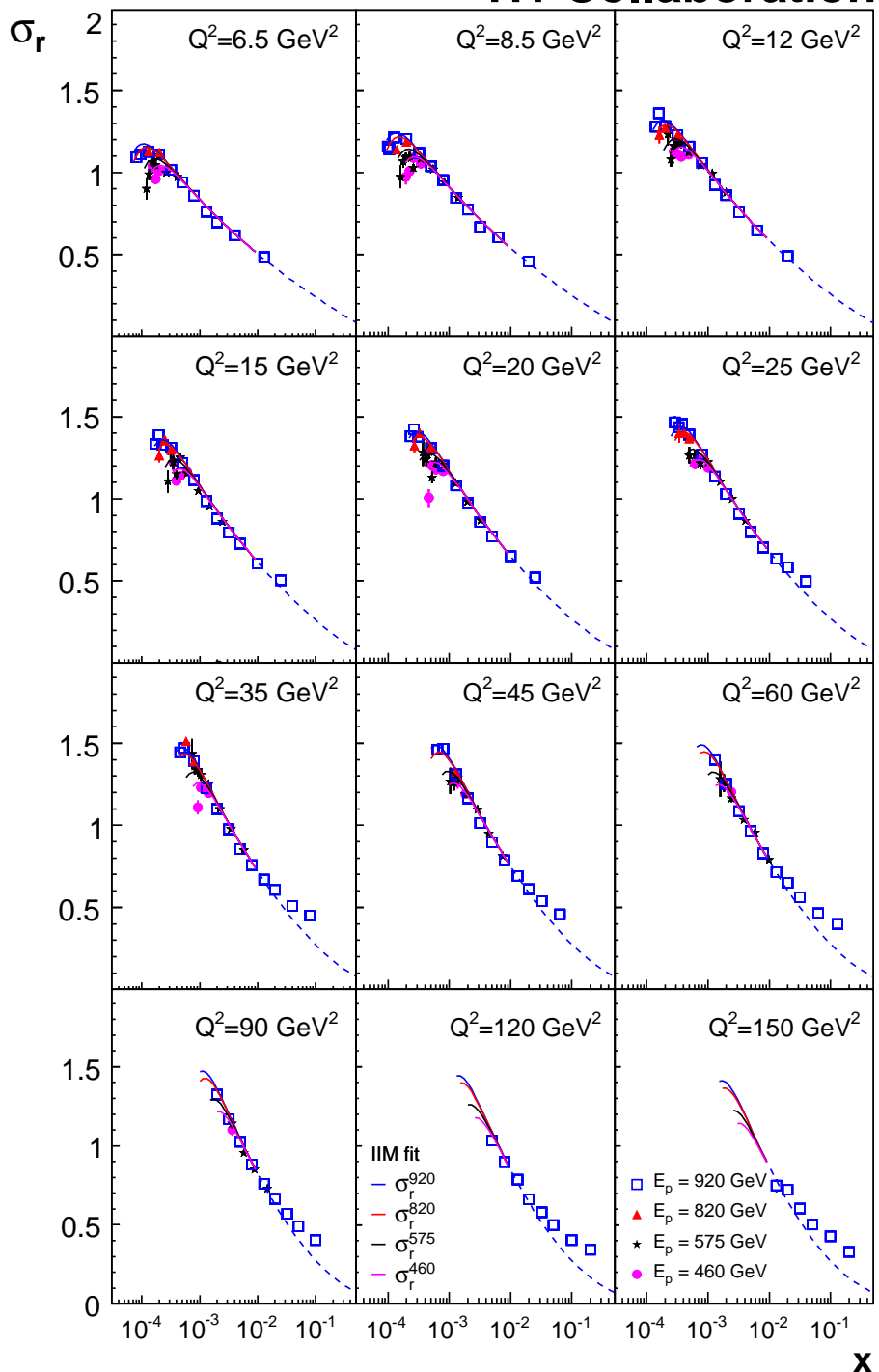


Figure 27: Reduced cross-section data taken at different proton beam energies E_p compared to IIM fit results for $6.5 \leq Q^2 \leq 150 \text{ GeV}^2$.

H1 Collaboration

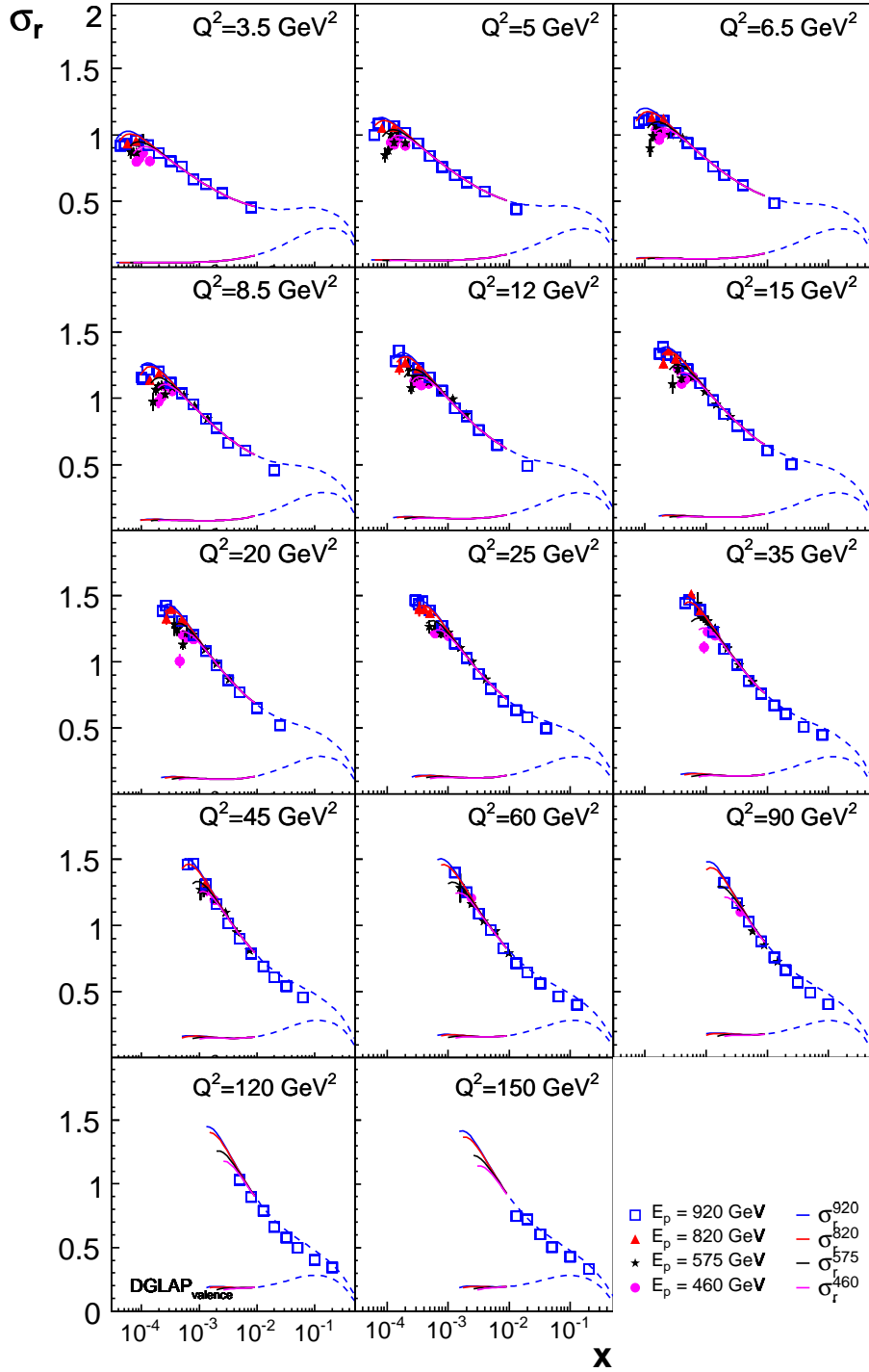


Figure 28: Reduced cross-section data taken at different proton beam energies E_p compared to IIM+DGLAP_{valence} fit results for $3.5 \leq Q^2 \leq 150 \text{ GeV}^2$. The lower curves show the contribution of DGLAP_{valence} calculation.

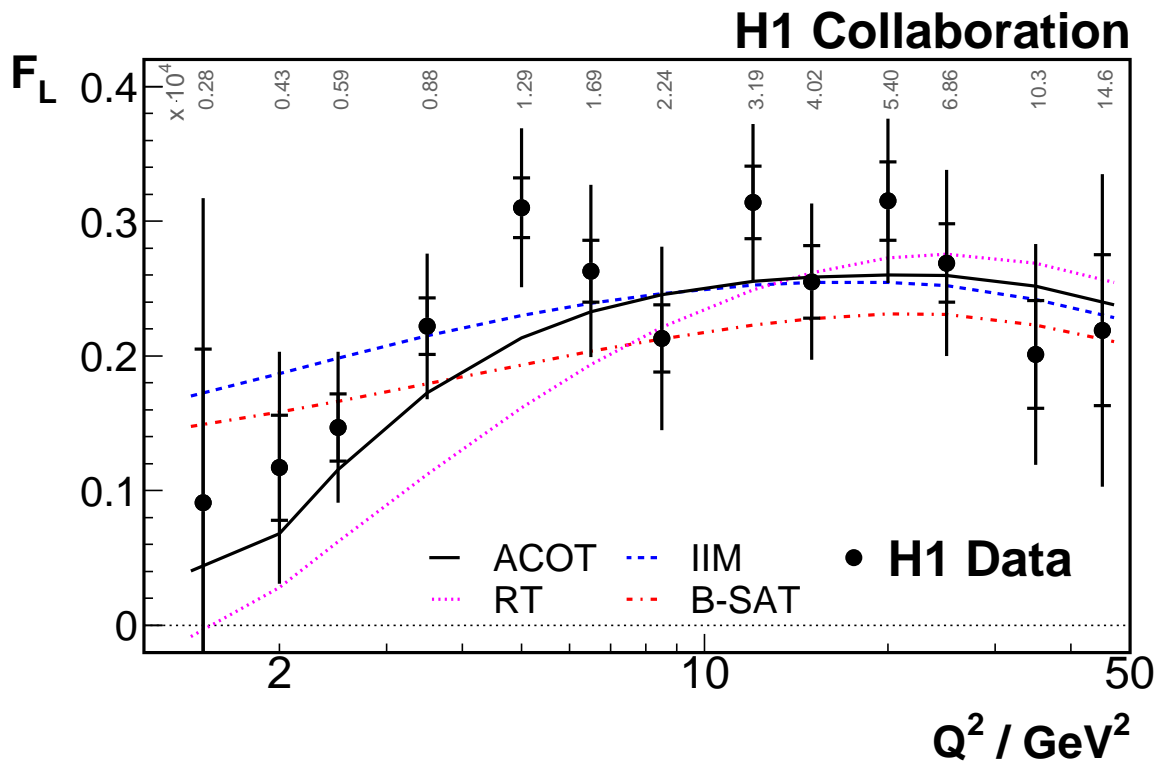


Figure 29: The proton structure function F_L shown as a function of Q^2 . The average x values for each Q^2 are indicated. The inner error bars represent statistical error, the full error bars include the statistical and systematic uncertainties added in quadrature. The lines represent results of the DGLAP ACOT and RT as well as dipole IIM and B-SAT model fits.